PhD Thesis

Dynamic Investigation of Bimodular Structures by Means of Isogeometric Analysis

submitted in satisfaction of the requirements for the degree
Doctor of Science in Civil Engineering
of the TU Wien, Faculty of Civil and Environmental Engineering

---

Dissertation

Dynamische Untersuchung von bimodularen Strukturen mit Hilfe isogeometrischer Analyse

ausgeführt zum Zwecke der Erlangung des akademischen Grads
Doktor der technischen Wissenschaften
eingereicht an der TU Wien, Fakultät für Bau- und Umweltingenieurwesen

Dipl.-Ing. **Galeb El Chabaan**

Matr.Nr.: 01228538

Betreuung:	Ao.Univ.Prof. Univ.Prof. Dipl.-Ing. Dr.techn. **Rudolf Heuer** Institut für Tragkonstruktionen Forschungsbereich Baumechanik und Baudynamik Technische Universität Wien Karlsplatz 13/212-03, 1040 Wien, Österreich
Begutachtung:	Associate Prof. Dipl.-Ing. Dr.techn. **Christian Schranz**, M.Sc. Institut für Baubetrieb und Bauwirtschaft Forschungsbereich Digitaler Bauprozess Technische Universität Wien Karlsplatz 13/235-03, 1040 Wien, Österreich
Begutachtung:	Univ.Prof.in Dr.-Ing.in **Stefanie Elgeti** Institut für Leichtbau und Struktur-Biomechanik Forschungsbereich Leichtbau Technische Universität Wien Getreidemarkt 9, 1060 Wien, Österreich

Wien, im April 2024

Danksagung

An dieser Stelle möchte ich mich ganz herzlich bei jenen bedanken, die mich während meiner Tätigkeit an der Technischen Universität Wien, insbesondere beim Verfassen dieser Dissertation, unterstützt haben.

Mein besonderer DANK gilt meinem Betreuer Herrn Ao.Univ.Prof. Univ.Prof. Dipl.-Ing. Dr.techn. Rudolf Heuer für seine wertvolle Unterstützung. Seine Anregungen zu diesem Thema sowie der ihm zu verdankende Freiraum ermöglichten es mir, meine eigenen Ideen zu entwickeln und umzusetzen. Darüber hinaus bin ich aufrichtig dankbar für seine stets offene Tür und die Geduld, die er während meiner gesamten Arbeit an der Dissertation als Betreuer gezeigt hat.

Herrn Associate Prof. Dipl.-Ing. Dr.techn. Christian Schranz, M.Sc. möchte ich für die Übernahme des Gutachtens der Doktorarbeit herzlich danken.

Auch der Gutachterin, Frau Univ.Prof.in Dr.-Ing.in Stefanie Elgeti, gilt großer Dank. Trotz ihrer beruflichen Verpflichtungen und Zeitknappheit hat sie sich die Zeit genommen, meine Arbeit zu begutachten und zu bewerten.

Ein weiteres großes Dankeschön geht an alle derzeitigen und ehemaligen Kolleginnen und Kollegen des Forschungsbereiches, insbesondere an Frau Univ.Ass.in Dipl.-Ing.in Nathalie Ursel, BSc, für ihr sorgfältiges Korrekturlesen und ihre hilfreichen Anmerkungen während des Schreibens dieser Dissertation.

Meiner Familie bin ich zutiefst dankbar für ihre unermüdliche Unterstützung, auf die ich zu jeder Zeit zählen konnte und weiterhin kann. Nicht zuletzt möchte ich mich bei meinen Freunden bedanken. Ich bin euch unendlich dankbar, dass ich mich in guten wie in schlechten Zeiten immer auf euch verlassen kann.

Kurzfassung

In dieser Arbeit wird die dynamische Analyse von Systemen mit veränderlichen elastischen Eigenschaften während eines Schwingungsvorgangs untersucht. Das einfachste Modell für solche Systeme ist ein bilinearer elastischer Einmassenschwinger, der unterschiedliche Federsteifigkeiten bei Dehnung und Stauchung aufweist. Eine exakte Lösung lässt sich schrittweise herleiten, indem man auf lineare Lösungen eines Einmassenschwingers zurückgreift und die Kontinuität der Verschiebungen und Geschwindigkeiten unter bestimmten Übergangsbedingungen gewährleistet.

Diese Studie konzentriert sich insbesondere auf die mechanische Modellierung und numerische Analyse von ebenen, drehungsfreien, ursprünglich geraden, homogenen, schubstarren Bernoulli-Euler Balken mit klassischen Randbedingungen unter unterschiedlichen Anregungen. Die Balken bestehen aus einem Material mit unterschiedlichem Elastizitätsmodul im Zug- und Druckbereich, einem sogenannten bimodularen Material. Folglich wird die nichtlineare Spannungs-Dehnungs-Kurve durch zwei lineare Segmente mit einer Unstetigkeit der Steigung im Ursprung angenähert. Diese Eigenschaft impliziert, dass die neutrale Achse nicht durch den geometrischen Mittelpunkt eines Querschnitts verläuft und vom Vorzeichen der Krümmung abhängt. Die Ermittlung der Bewegungsgleichung für Biegeschwingungen erfolgt durch die Modellbildung eines effektiven zweischichtigen Balkens mit einer diskontinuierlichen neutralen Achse. Jede der beiden krümmungsabhängigen Biegekonfigurationen ist durch die Lage der neutralen Achse eindeutig charakterisiert, die nicht nur von den elastischen Materialeigenschaften, sondern auch von der Querschnittsform beeinflusst wird. In dieser Arbeit werden verschiedene Querschnitte untersucht, um hauptsächlich ihren Einfluss auf die Position der neutralen Achse, auf die Steifigkeiten sowie folglich auf die dynamische Antwort von bimodularen Balken zu zeigen. Je nach Querschnittsform kann das dynamische Verhalten eines bimodularen Trägers linear oder nichtlinear sein. Ein lineares dynamisches Verhalten zeigen bimodulare Träger mit symmetrischen Querschnitten bezüglich der η-Biegeachse, die durch den geometrischen Mittelpunkt verläuft. Im Gegensatz dazu weisen Träger mit unsymmetrischen Querschnitten eine Nichtlinearität auf, die sich aus den Unterschieden in der effektiven Biegesteifigkeit zwischen zwei Biegekonfigurationen ergibt. Im Falle des nichtlinearen Verhaltens kann keine exakte geschlossene Lösung für die gesamte betrachtete Zeit abgeleitet und durch eine einzige Gleichung ausgedrückt werden. Aus diesem Grund wird die isogeometrische Analyse angewandt, um eine Näherungslösung nicht nur für lineare, sondern insbesondere für nichtlineare Schwingungen eines bimodularen Balkens zu finden.

In einer numerischen Untersuchung liegt besonderes Augenmerk auf der Anwendung der isogeometrischen Finite-Elemente-Diskretisierung mit B-Splines für die dynamische Analyse von unimodularen und bimodularen Trägern mit jeweils drei verschiedenen Querschnitten. Die Querschnittsabmessungen werden so gewählt, dass ein annähernd gleiches Trägheitsmoment bezüglich der η-Biegeachse und gleiche Querschnittsflächen vorhanden sind, was zu gleichen Massen pro Längeneinheit führt. Im Rahmen dieser Studie werden drei verschiedenen Erregungen betrachtet. Eine davon ist die periodische Anregung, bei der die Antworten der Balken im Zeit- und Frequenzbereich analysiert werden. Während die modifizierte Newmark-Methode zur Analyse im Zeitbereich verwendet wird, dient das Verfahren der Harmonischen Balance speziell zur Untersuchung im Frequenzbereich, wobei der Fokus auf nichtlinearen bimodularen Balken liegt. In diesem Fall approximiert eine Fourier-Reihe die Lösung eines nichtlinearen gewöhnlichen Differentialgleichungssystems, welches durch zusätzliche asymmetrische innere

Kräfte aufgrund von Variationen der effektiven Biegesteifigkeit entsteht. Durch die Approximation der stationären Lösung verringert sich mit dem Verfahren der Harmonischen Balance der Rechenaufwand für potenziell lange Einschwingvorgänge und es wird in der Regel eine akzeptable Genauigkeit bei der Verwendung von nur wenigen Reihengliedern erreicht. Ein Vergleich der Antworten zeigt den signifikanten Einfluss von bimodularen Materialien, insbesondere von den Querschnittseigenschaften.

Abstract

This thesis investigates the dynamic response of systems exhibiting varying elastic properties during a vibrational process. The simplest model for such systems is a bilinear elastic oscillator characterized by different spring stiffness in the tensile and compressive domains. An exact solution can be derived piecewise by utilizing linear solutions of a single-degree-of-freedom system and ensuring continuity of displacement and velocity under specified conditions at transition times.

However, this study particularly focuses on the mechanical modeling and numerical analysis of the dynamic response of planar, rotation-free, initially straight, homogeneous Bernoulli-Euler beams rigid in shear. This study analyzes beams with classical boundary conditions under time-varying excitation. However, the beams are made from material with different elastic Young's modulus in tension and compression, known as bimodular material. Consequently, the nonlinear stress-strain curve is approximated by two linear segments with a discontinuity in slope at the origin. This characteristic implies that the neutral axis does not pass through the geometric centroid of a cross-section and, indeed, depends on a curvature's sign. Thus, formulating the equation governing flexural oscillations involves defining a model with two-layer laminates and a discontinuous neutral beam axis. Each of the two bending configurations is uniquely characterized by its neutral axis position, influenced not only by the elastic material properties but also by the shape of the cross-section. In this thesis, various cross-sections are considered in order to demonstrate their influence primarily on the position of the neutral axis, on stiffnesses and, consequently, on the dynamic response of bimodular beams. The dynamic response of a bimodular beam can vary from linear to nonlinear, depending on the specific cross-sectional shape. Bimodular beams with symmetric cross-sections relative to the η-bending axis, passing through the geometric centroid, demonstrate a linear dynamic response. Conversely, bimodular beams with nonsymmetric cross-sections exhibit nonlinearity due to variations in effective bending stiffness during upward and downward bending motions. In the case of the nonlinear behavior of the bimodular beam, an exact closed-form solution cannot be derived for the entire considered motion domain expressed by a single equation. For this reason, isogeometric analysis is applied to provide an approximated solution, not just for linear but particularly for nonlinear vibration of a bimodular beam.

In a numerical investigation, special attention is directed towards employing isogeometric finite element discretization with B-splines for the dynamic analysis of both unimodular and bimodular beams, each with three different cross-sections. However, in order to illustrate the effect of cross-sectional shape on dynamic response, their dimensions are carefully chosen to ensure approximately equal moment of inertia with respect to the η-bending axis and equal cross-sectional areas, resulting in equal mass per unit length. Within this study, three different types of excitations are applied to the beams. One of these includes periodic excitation, whereby the responses of the beams are evaluated across time and frequency domains. While the modified Newmark method is utilized to analyze the responses in the time domain, the harmonic balance method is specifically applied to investigate the frequency-response function to periodic excitation, emphasizing nonlinear bimodular beams. In this case, the truncated Fourier series approximates the solution of a nonlinear ordinary differential equation system, which arises from additional asymmetric internal forces due to variations in effective bending stiffness between upward and downward bending motion. By approximating the steady-state solution, the harmonic balance

method reduces the computational cost of potentially long transient responses and commonly achieves acceptable accuracy even with a low truncation order. A comparison of responses shows the significant influence of bimodular materials, particularly with regard to the properties of the cross-section.

Contents

Chapter 1

Introduction

Certain materials exhibit different stress-strain behaviors under tension compared to compression, a phenomenon first recognized by St. Venant in 1864 while analyzing the pure bending behavior of a beam. However, the concept of materials showing different moduli in tension and compression was first introduced by Timoshenko in 1941, particularly in the context of analyzing the flexural stresses in such materials during pure bending, [50]. In 1965, Ambartsumyan further develops this concept in two dimensions, according to [23]. These materials are known by terms such as bimodular, bimodulus, and bilinear and are characterized by varying moduli. Experimental observations validate this phenomenon across a wide spectrum of materials, including cast iron, tire-cord rubber, concrete, reinforced concrete, epoxies, rock, cord-rubber composite, carbon composite, aramid rubber, polyester rubber, bone, soft biological tissues, and numerous others. These materials exhibit not only different behaviors under tension and compression but also, in some cases, significant nonlinear stress-strain curves. However, it is possible to approximate the stress-strain curve with two straight lines, showing a slope discontinuity at the origin, [52]. Fig. 1.1 graphically illustrates the approximated stress-strain curve of bimodular material, where E_t and E_c denote elastic Young's modulus in tension and compression, respectively. Additionally, another method entails utilizing two segments in tension and two segments in compression, as presented in [24].

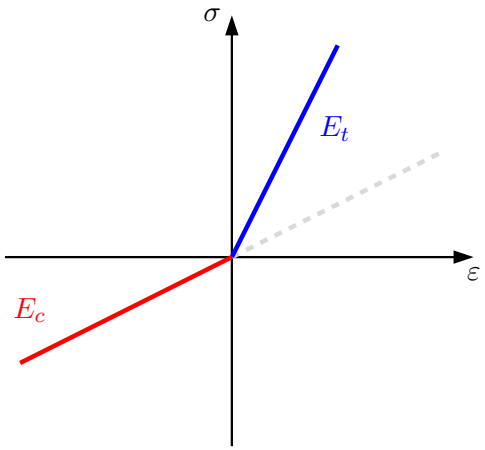

Fig. 1.1: Stress-strain curve of bimodular material

The analysis of bimodular structures presents greater complexity compared to unimodular materials due to the dependence of stiffness on the state of stress. Specifically, stiffnesses are determined by the neutral surface position, which is initially unknown and often requires iterative procedures for precise calculation. Nevertheless, in certain specific cases where axial force is absent, the neutral surface maintains a consistent position throughout the structure's length, thus simplifying computational procedures significantly.

Many studies have been conducted to investigate the behavior of bimodular composite beam, plate, and shell structures. Bert [1] introduces a macroscopic fiber direction strain-governed material model, commonly referred to as Bert's model, for bimodulus fiber-reinforced composites. Bert and Tran [4, 5, 51] analyze the small-deflection static and transient behavior of single-layer bimodulus beams using the transfer-matrix approach. Gordaninejad et al. [2, 23] similarly investigate the behavior of Timoshenko beams composed of multimodular materials, employing the transfer-matrix approach as well. The application of Levinson beam theory, including shear deformation and warping of the cross-section, to analyze the thick bimodular beam with rectangular cross-section is represented in [33]. Ghazavi and Gordaninejad [22] present a study of the nonlinear bending of thick, rectangular beams made from bimodulus materials, employing a higher-order shear deformation theory with a mixed finite element method. Additionally, Gordaninejad analyzes the effect of shear deformation of bimodular fibrous composite plates in [25], also implementing a high-order theory and utilizing a mixed finite element method. The analytical, numerical, and experimental investigations of bimodular thick sandwich beams are detailed in [26, 43]. Furthermore, the analysis of rectangular plates incorporating bimodulus composite material, conducted via finite element analysis, can be found in [3, 9, 44–47]. Based on the parametric variational principle and finite element method, computational methods for mechanical analysis of bimodular structures are presented in [57, 58]. The governing equations of the bimodular thick plate obtained using the average stress method are documented in [20]. Additionally, based on higher-order plate theory, Dong et al. [19] analyze the vibration and buckling of rectangular bimodular laminated simply supported single- and two-layered cross-ply plates. Analytical solutions for tapered and curved bimodular beams are derived in [28, 34]. A perturbation method is employed to solve bimodular von-Kármán circular plates under centrally concentrated forces, as described in [27]. Patel et al. investigate the free flexural vibration behavior of bimodular laminated angle-ply composite plates, [39]. Using the finite element approach, Patel et al. [40] also study the flexural behavior of bimodular laminated composite plates subjected to thermal load. Regarding bimodular shells, Bert and Kumar [6] formulate a theory for the small amplitude free vibration of circular cylindrical shells made from bimodular material.

This thesis is organized into six chapters. Following this initial chapter, Chapter 2 introduces the bilinear elastic oscillator as the fundamental model characterized by its varying elastic resistance properties during vibration. In the first part of this chapter, the governing equation is formulated by applying Newton's second law of motion. Subsequently, an analytical solution to the free vibration equation is derived piecewise due to the variation of the elastic resisting force with the sign of displacement. Similarly, an exact solution is presented for the system under harmonic excitation. Maintaining continuity in displacement and velocity at transition times is crucial and can be ensured through particular conditions. The chapter concludes with an illustrative example.

Chapter 3 presents the mechanical modeling of homogeneous Bernoulli-Euler beams rigid in shear. However, they are composed of material with different elastic Young's modulus in tension and compression. Consequently, the neutral axis does not pass through the geometric centroid of a cross-section and strongly depends on the sign of curvature. Moreover, the position of the neutral axis in the considered bending configuration additionally depends not only on elastic material properties but also on the specific cross-section used. For this reason, one of the main focuses of this thesis is to analyze the influence of the cross-section on the dynamic response of bimodular structures. Within this chapter, various cross-sections are analyzed in order to determine their influence on system behavior.

The main idea and concept of isogeometric analysis and its application to the bimodular beam vibration are represented in Chapter 4. The first part of this chapter provides an introduction to

B-splines and refinement techniques, followed by linear and nonlinear vibration analysis utilizing isogeometric finite element discretization. Building upon the linear case, the discretized equation of motion is formulated by including an additional nonlinear force vector. This vector arises from asymmetric internal forces due to effective bending disparities between upward and downward bending configurations. The chapter concludes with a focus on the harmonic balance method, particularly emphasizing its application for nonlinear analysis in the frequency domain when a system is subjected to periodic excitation.

Chapter 5 presents the numerical analysis of the bimodular beam subjected to three different excitations. In order to demonstrate the influence of the bimodular material, especially the cross-sectional shape, on the dynamic response, this study considers both unimodular and bimodular beams, each with three cross-sections, namely, rectangular, triangular, and T cross-sections. However, their dimensions are carefully chosen in such a way that they have equal cross-sectional areas and approximately equal moment of inertia with respect to the bending axis. The equal cross-sectional areas imply that the beams possess equal mass per unit length. This study utilizes the modified Newmark method for analysis in the time domain, while the harmonic balance method plays an important role in determining the responses in the frequency domain.

Finally, Chapter 6 serves as the last chapter in this thesis, offering a comprehensive summary and concluding the discussion on this topic.

The text of this thesis was written using the word processing program LaTeX, and the mathematical software MATLAB R2023b was used to carry out all the numerical analyses.

Chapter 2

Dynamic analysis of bilinear elastic oscillator

Dynamic systems are typically classified into two categories based on their behavior, namely, linear and nonlinear. This chapter is focused on the bilinear spring mass system, characterized by a bilinear force-displacement curve. Specifically, the spring stiffness varies with the positive and negative displacements, resulting in nonlinear effects in the system's response. In Section 2.1 of this chapter, an equation of motion for a bilinear elastic oscillator is derived. Since an analytical solution cannot be defined by a single equation covering the entire motion domain, as in the case of a linear system, the solution is derived piecewise. This approach is applied not only for free vibration in Section 2.2 but also for forced vibration, as presented in Section 2.3. The chapter concludes with an example in Section 2.4, showing the nonlinear behavior of the bilinear system.

2.1 Equation of motion

Bilinear elastic dynamic systems can be modeled by bilinear oscillators, as shown in Fig. 2.1. The entire mass m of the system is concentrated within a rigid block, constrained by rollers to move in one direction only. It is called a single-degree-of-freedom (SDOF) system since the single displacement coordinate $x(t)$ is sufficient to define the position of the mass at any time t. However, the elastic resistance to displacement is provided by either one or two springs in such a way that the mechanical model has two different stiffness constants $k^{(+)}$ and $k^{(-)}$ corresponding to positive and negative displacement domain, respectively. The energy dissipation mechanism is represented by a linear viscous damper in a parallel arrangement, with the viscous damping coefficient c assumed to remain constant throughout the motion. The system is subjected to a time-varying external force $p(t)$.

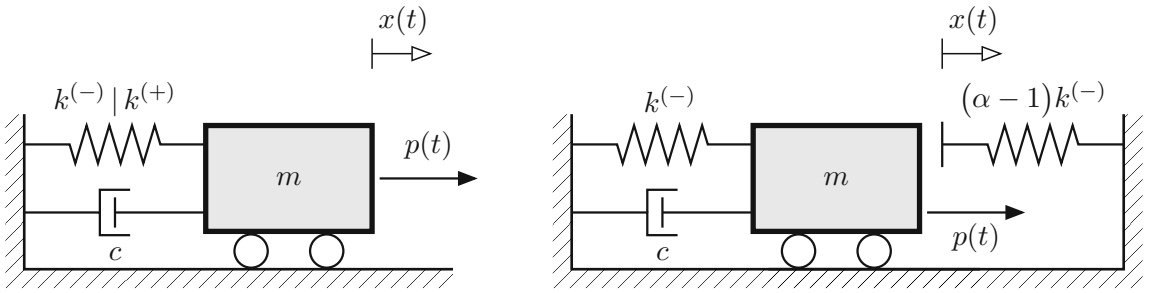

Fig. 2.1: Bilinear elastic oscillator models

In addition to this external force $p(t)$, which is assumed to act positively in the direction of the displacement degree of freedom, the forces acting on the mass include the elastic resisting force f_S and the damping resisting force f_D. The relationship between the elastic resisting force and relative displacement is graphically illustrated in Fig. 2.2, assuming that the stiffness constant within the positive displacement domain, $k^{(+)}$, is greater than the one within the negative, $k^{(-)}$.

Since the system is characterized by displacement-dependent stiffness, as shown in this figure,

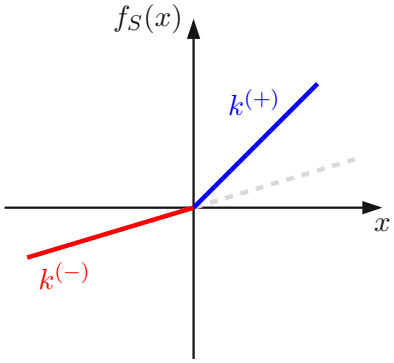

Fig. 2.2: The resisting force of bilinear elastic oscillator

the elastic resisting force can be expressed as follows

$$f_S(x) = \begin{cases} k^{(+)}x = \alpha\, k^{(-)}x & x \geq 0 \\ k^{(-)}x & x < 0 \end{cases} \tag{2.1}$$

where $\alpha = k^{(+)}/k^{(-)}$ denotes the spring stiffness ratio. In the presence of linear viscous damper, the damping resisting force is determined by the damping constant c multiplied by the velocity $v(t)$, which is given by

$$f_D = c\, v(t) \tag{2.2}$$

Both the elastic and damping forces resist deformation and velocity, respectively, act in opposite directions. The equation of motion for the mass-bilinear spring-damper system subjected to external force can be formulated by using Newton's second law of motion

$$m\ddot{x} = p(t) - f_S(x) - f_D \tag{2.3}$$

Finally, substituting Eq. (2.2) into Eq. (2.3) and rearranging gives the following equation of motion governing the displacement

$$m\ddot{x} + c\dot{x} + f_S(x) = p(t) \tag{2.4}$$

Here, $\dot{(\cdot)}$ denotes differentiation with respect to time $\mathrm{d}(\cdot)/\,\mathrm{d}t$, thus $\dot{x}$ represents the velocity and $\ddot{x}$ represents the acceleration of the mass.

2.2 Free vibration

The differential equation governing free vibration of the bilinear elastic oscillator with damping can be obtained by setting $p(t) = 0$ on the right-hand side of Eq. (2.4), resulting in

$$m\ddot{x} + c\dot{x} + f_S(x) = 0 \tag{2.5}$$

Dividing by m yields the following second-order time differential equation

$$\ddot{x} + 2\zeta(x)\,\omega_0(x)\,\dot{x} + \omega_0^2(x)\,x = 0 \tag{2.6}$$

Here, $\omega_0(x)$ and $\zeta(x)$ denote the natural circular frequency of vibration and damping ratio, respectively. Due to the system's stiffness dependency on displacement, characterized by different values between positive and negative displacement domains, the natural circular frequency in this case can be generally defined as

$$\omega_0(x) = \begin{cases} \omega_0^{(+)} & x \geq 0 \\ \omega_0^{(-)} & x < 0 \end{cases} \tag{2.7}$$

by introducing the natural circular frequency specified within the positive and negative displacement domains as follows

$$\omega_0^{(+)} = \sqrt{\frac{k^{(+)}}{m}} \qquad \omega_0^{(-)} = \sqrt{\frac{k^{(-)}}{m}} \tag{2.8}$$

The relationship between these two natural circular frequencies can be expressed through the utilization of the stiffness ratio α, resulting in

$$\frac{\omega_0^{(+)}}{\omega_0^{(-)}} = \sqrt{\alpha} \tag{2.9}$$

The damping ratio can be defined in the same manner, with different values assigned to the positive and negative displacement domains, given by

$$\zeta(x) = \begin{cases} \zeta^{(+)} & x \geq 0 \\ \zeta^{(-)} & x < 0 \end{cases} \tag{2.10}$$

where

$$\zeta^{(+)} = \frac{c}{2\sqrt{mk^{(+)}}} \qquad \zeta^{(-)} = \frac{c}{2\sqrt{mk^{(-)}}} \tag{2.11}$$

Similarly, with the utilization of the stiffness ratio α, one can derive the relationship between two damping ratios, leading to

$$\frac{\zeta^{(+)}}{\zeta^{(-)}} = \frac{1}{\sqrt{\alpha}} \tag{2.12}$$

Based on the bilinear elastic resisting force according to Fig. 2.2, which shows a discontinuity in stiffness at $x = 0$, an analytical solution cannot generally be represented by a single equation that covers the entire motion domain as a linear system. Nevertheless, it remains possible to derive solutions for each domain individually, as the governing equations of motion retain linearity within their respective domains, [42]. Such solutions to Eq. (2.6) for the underdamped case, where $\zeta(x) < 1$, can be derived from the linear case solution, as presented in [14, 29], leading to

$$x_i(t) = e^{-\zeta_i \omega_{0,i} t}\Big(A_i \cos \omega_{D,i} t + B_i \sin \omega_{D,i} t\Big) \qquad t_{0,i} \leq t < t_{0,i+1} \tag{2.13}$$

where index i denotes the *specific*-cycle of motion over time within a single positive or negative displacement domain, which is similar to a half-cycle in a sine or cosine waveform. The time $t_{0,i}$ symbolizes the transition time point from one displacement domain to another, occurring when the displacement becomes zero. However, $t_{0,1}$ denotes the initial time, starting at zero, at which the system is influenced by initial conditions and the displacement may not necessarily be zero.

The initial state of the system is determined by the given initial displacement $x_0 = x_1(t=0)$ and initial velocity $\dot{x}_0 = \dot{x}_1(t=0)$, and the constants of the first specific-cycle A_1 and B_1 need to be determined based on these initial conditions. The parameter $\omega_{D,i}$ appearing in Eq. (2.13) represents the natural circular frequency of damped vibration for the i^{th} specific-cycle, defined as follows

$$\omega_{D,i} = \omega_{0,i}\sqrt{1-\zeta_i^2} \tag{2.14}$$

Both the natural circular frequencies $\omega_{0,i}$ and $\omega_{D,i}$, as well as the damping ratio ζ_i, depend on the stiffness and undergo changes during the transition from one domain to another. Therefore, it is of particular interest to determine, through the initial state, whether the first transition is from positive to negative displacement domain or vice versa, leading to the following two cases for defining the sequence of the natural circular frequencies and damping ratios during the vibration

- Case 1: Displacements within the first specific-cycle are positive, $x_1(t) > 0$

$$\omega_{0,i} = \begin{cases} \omega_0^{(+)} & i = 1,3,5,... \\ \omega_0^{(-)} & i = 2,4,6,... \end{cases} \qquad \zeta_i = \begin{cases} \zeta_i^{(+)} & i = 1,3,5,... \\ \zeta_i^{(-)} & i = 2,4,6,... \end{cases} \tag{2.15}$$

- Case 2: Displacements within the first specific-cycle are negative, $x_1(t) < 0$

$$\omega_{0,i} = \begin{cases} \omega_0^{(-)} & i = 1,3,5,... \\ \omega_0^{(+)} & i = 2,4,6,... \end{cases} \qquad \zeta_i = \begin{cases} \zeta_i^{(-)} & i = 1,3,5,... \\ \zeta_i^{(+)} & i = 2,4,6,... \end{cases} \tag{2.16}$$

After establishing the natural circular frequencies and damping ratios, it is necessary to determine not only the integration constants A_i and B_i, but also the transition time $t_{0,i}$ for each specific-cycle i to achieve the solution outlined in Eq. (2.13). The motion, subjected to both initial conditions and represented by this solution, is visually depicted in Fig. 2.3, where the displacements remain positive throughout the initial specific-cycle, indicated by $x_1(t) > 0$.

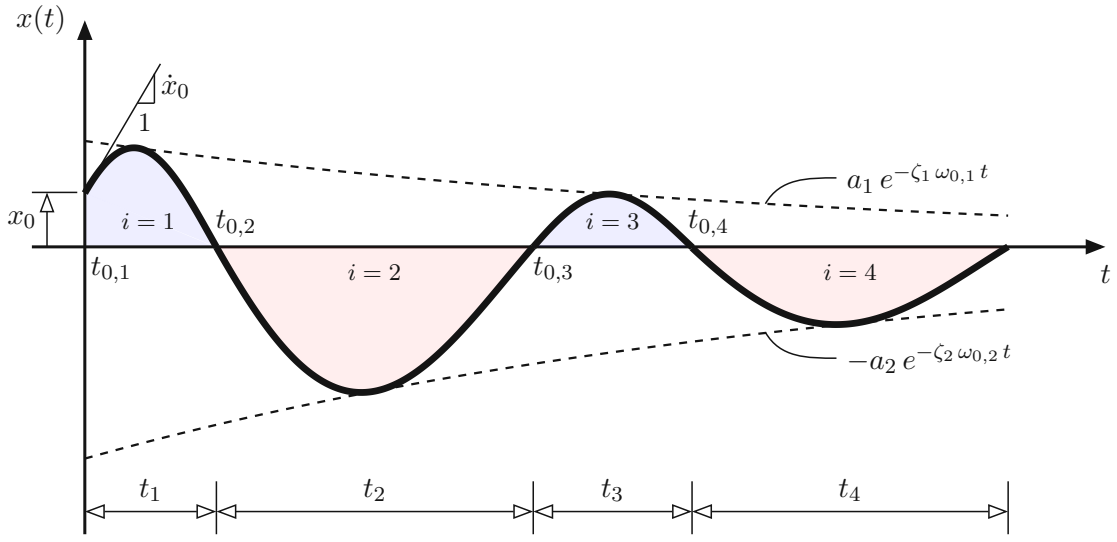

Fig. 2.3: Free-vibration response of the bilinear elastic oscillator

However, for a more straightforward approach in order to find the solution, the expression provided in Eq. (2.13) can be alternatively reformulated as follows

$$x_i(t) = a_i\, e^{-\zeta_i \omega_{0,i} t} \cos\left(\omega_{D,i} t - \varepsilon_i\right) \tag{2.17}$$

where a_i and ε_i denote the amplitude of the vibratory displacement $x_i(t)$ and phase angle of the i^{th} specific-cycle, respectively. These two quantities, as well as the transition time $t_{0,i}$, must be successively determined for each vibration cycle, starting from the first specific-cycle, $i = 1$. In order to determine the amplitude a_1 within the initial displacement domain, one must determine the integration constants A_1 and B_1 by evaluating Eq. (2.13) and its first time derivative at $t = 0$, thereby yielding the following well-known constants

$$A_1 = x_0 \qquad\qquad B_1 = \frac{\dot{x}_0 + \zeta_1\, \omega_{0,1}\, x_0}{\omega_{D,1}} \tag{2.18}$$

Hence, the first amplitude can be expressed in terms of the initial displacement x_0 and initial velocity $\dot{x}_0$, as follows

$$a_1 = \sqrt{A_1^2 + B_1^2} = \sqrt{x_0^2 + \left(\frac{\dot{x}_0 + \zeta_1\, \omega_{0,1}\, x_0}{\omega_{D,1}}\right)^2} \tag{2.19}$$

Given the first constants according to Eq. (2.18), the phase angle can also be obtained for the first specific-cycle, as shown by

$$\varepsilon_1 = \arctan\frac{B_1}{A_1} = \arctan\left(\frac{\dot{x}_0 + \zeta_1\, \omega_{0,1}\, x_0}{\omega_{D,1}\, x_0}\right) \tag{2.20}$$

The duration of the first specific-cycle, denoted by t_1 and coinciding with the transition time $t_{0,2}$, can be determined by the condition that the displacement reaches zero at that time point. Specializing Eq. (2.17) for the first specific-cycle and equating it to zero yields

$$a_1\, e^{-\zeta_1 \omega_{0,1} t_1} \cos\left(\omega_{D,1} t_1 - \varepsilon_1\right) = 0 \tag{2.21}$$

which is satisfied for all values of a_1 if

$$\cos\left(\omega_{D,1} t_1 - \varepsilon_1\right) = 0 \tag{2.22}$$

By setting the quantities in brackets to $\pi/2$, the following expression for the duration of the first specific-cycle, i.e., the first transition time, is derived

$$t_1 = t_{0,2} = \frac{\pi + 2\varepsilon_1}{2\omega_{D,1}} \tag{2.23}$$

In a similar manner, the remaining transition time points can be determined, emphasizing their recursive nature. Consequently, the transition times from the second specific-cycle onwards can be expressed using the following recursive formula

$$t_{0,i+1} = t_{0,i} + \frac{\pi}{\omega_{D,i}} \qquad\qquad i = 2, 3, \ldots \tag{2.24}$$

As mentioned previously, the displacements reach zero at these transition times, while the velocities do not. However, maintaining velocity continuity at these points is essential and can be expressed as follows

$$\dot{x}_{i-1}(t_{0,i}) = \dot{x}_i(t_{0,i}) \tag{2.25}$$

The first derivative of Eq. (2.17) with respect to time provides the velocity of the i^{th} specific-cycle, which is represented by

$$\dot{x}_i(t) = -a_i\, e^{-\zeta_i \omega_{0,i} t}\Big[\zeta_i \omega_{0,i} \cos\Big(\omega_{D,i} t - \varepsilon_i\Big) + \omega_{D,i} \sin\Big(\omega_{D,i} t - \varepsilon_i\Big)\Big] \tag{2.26}$$

Specializing this equation for both specific-cycles $i-1$ and i at the transition time $t_{0,i}$, and then substituting them into Eq. (2.25), yields

$$-a_{i-1}\, e^{-\zeta_{i-1}\omega_{0,i-1} t_{0,i}}\, \omega_{D,i-1} = -a_i\, e^{-\zeta_i \omega_{0,i} t_{0,i}}\, \omega_{D,i} \tag{2.27}$$

The following relationship can be derived from Eqs. (2.9) and (2.12)

$$\zeta^{(+)}\omega_0^{(+)} = \zeta^{(-)}\omega_0^{(-)} \tag{2.28}$$

This implies that the product of the damping ratio and natural circular frequency remains constant throughout the entire vibration process and can also be expressed in general form using index notation as

$$\zeta_{i-1}\, \omega_{0,i-1} = \zeta_i\, \omega_{0,i} \tag{2.29}$$

Finally, by substituting this equation into Eq. (2.27), the amplitude relationship between two neighboring specific-cycles can be defined as

$$a_i = \frac{\omega_{D,i-1}}{\omega_{D,i}} a_{i-1} \qquad\qquad i = 2, 3, \ldots \tag{2.30}$$

Regarding the phase angle, it is obvious from Eq. (2.20) that the phase angle in the first displacement domain depends on both initial conditions x_0 and $\dot{x}_0$. Consequently, the phase angle of the i^{th} specific-cycle is influenced by the displacement and velocity at the beginning of the i^{th} cycle, namely, at the transition time $t_{0,i}$. Since the displacement becomes zero at the transition time $t_{0,i}$, the equation for determining the i^{th} phase angle can be formulated by specializing Eq. (2.17) for $t = t_{0,i}$ and equating it to zero, as follows

$$a_i\, e^{-\zeta_i \omega_{0,i} t_{0,i}} \cos\Big(\omega_{D,i} t_{0,i} - \varepsilon_i\Big) = 0 \tag{2.31}$$

This condition can be met if $a_i = 0$, resulting in a trivial solution. Therefore, the cosine function must be zero, which can be achieved by

$$\omega_{D,i} t_{0,i} - \varepsilon_i = \Big(2i - 1\Big)\frac{\pi}{2} \tag{2.32}$$

For a given natural circular frequency of damped vibration $\omega_{D,i}$ and transition time $t_{0,i}$, the unknown i^{th} phase angle can be obtained by

$$\varepsilon_i = \omega_{D,i} t_{0,i} - \Big(2i - 1\Big)\frac{\pi}{2} \qquad\qquad i = 2, 3, \ldots \tag{2.33}$$

The time needed to complete a full cycle of free vibration is defined as the natural period $T_{D,bi}$ for the damped vibration of the bilinear elastic oscillator. It is apparent from Fig. 2.3 that the

time required to complete the first full cycle, which is the sum of the first two specific-cycles, corresponds to the transition time $t_{0,3}$. This transition time, along with the first phase angle ε_1, determines the natural period of damped vibration as follows

$$T_{D,bi} = \frac{\pi/2 - \varepsilon_1}{\omega_{D,1}} + t_{0,3} \tag{2.34}$$

The determination of the transition time $t_{0,3}$ involves specializing Eq. (2.24) for $i = 2$, while also taking into account Eq. (2.23). Subsequently, substituting the derived transition time into Eq. (2.34) yields the natural period of damped vibration for the bilinear system, given by

$$T_{D,bi} = \frac{\pi}{\omega_{D,1}} + \frac{\pi}{\omega_{D,2}} = \frac{\pi}{\omega_D^{(+)}} + \frac{\pi}{\omega_D^{(-)}} \tag{2.35}$$

Based on the well-known relationship between the natural period of vibration and circular frequency, the following expression defines the natural circular frequency of damped vibration for the bilinear elastic oscillator, [42, 49, 60]

$$\omega_{D,bi} = \frac{2\pi}{T_{D,bi}} = \frac{2\,\omega_D^{(+)}\omega_D^{(-)}}{\omega_D^{(+)} + \omega_D^{(-)}} \tag{2.36}$$

The damped natural cyclic frequency can be also defined by utilizing either Eq. (2.35) or Eq. (2.36), expressed as

$$f_{D,bi} = \frac{1}{T_{D,bi}} = \frac{\omega_{D,bi}}{2\pi} \tag{2.37}$$

For an undamped system, the natural circular frequency of the bilinear elastic oscillator can be derived by specializing Eq. (2.36) for $\zeta^{(+)} = 0$ and $\zeta^{(-)} = 0$ and expressing in terms of $\omega_0^{(-)}$ and α using the relationship between the two natural circular frequencies according to Eq. (2.9), leading to

$$\omega_{0,bi} = \frac{2\omega_0^{(+)}\omega_0^{(-)}}{\omega_0^{(+)} + \omega_0^{(-)}} = \frac{2\sqrt{\alpha}}{1+\sqrt{\alpha}}\,\omega_0^{(-)} \tag{2.38}$$

In a similar manner, the natural period of vibration and natural cyclic frequency are defined for an undamped system, expressed by $\omega_0^{(-)}$ and α, as follows

$$T_{bi} = \frac{\pi(1+\sqrt{\alpha})}{\sqrt{\alpha}\,\omega_0^{(-)}} \qquad f_{bi} = \frac{\sqrt{\alpha}}{\pi(1+\sqrt{\alpha})}\,\omega_0^{(-)} \tag{2.39}$$

2.3 Response due to harmonic excitation

The bilinear elastic system, as depicted in Fig. 2.1, was previously analyzed for the free vibration case, only considering the given initial conditions. The current focus lies on investigating the system's response due to a harmonic excitation, particularly characterized by a cosine waveform expressed as follows

$$p(t) = p_0 \cos \nu t \tag{2.40}$$

where p_0 denotes the amplitude of the force, and ν represents the exciting or forcing frequency. Substituting this harmonic force in Eq. (2.4) gives

$$m\ddot{x} + c\dot{x} + f_S(x) = p_0 \cos \nu t \tag{2.41}$$

When divided by m and considering the bilinear nature of the elastic resisting force, the equation of motion can be written in the following form

$$\ddot{x} + 2\zeta(x)\,\omega_0(x)\,\dot{x} + \omega_0^2(x)\,x = \frac{1}{m}\,p_0 \cos \nu t \tag{2.42}$$

Similarly to the approach from the previous subsection, the solution to this equation can be derived separately for each specific-cycle by applying the solution obtained from the linear case outlined in [14, 29]. In this case, the solution can be expressed as follows

$$x_i(t) = e^{-\zeta_i \omega_{0,i}\left(t - t_{0,i}\right)} \left[A_i \cos \omega_{D,i}(t - t_{0,i}) + B_i \sin \omega_{D,i}(t - t_{0,i})\right] + C_i \cos \nu(t - t_{0,i}) + D_i \sin \nu(t - t_{0,i}) \tag{2.43}$$

Here, the initial component of the equation, characterized by the natural circular frequencies $\omega_{0,i}$ and $\omega_{D,i}$, represents the free or transient vibration, while the subsequent part incorporating the exciting frequency ν describes the forced or steady-state vibrations. Fig. 2.4 illustrates such a motion of the bilinear elastic oscillator induced by a harmonic force.

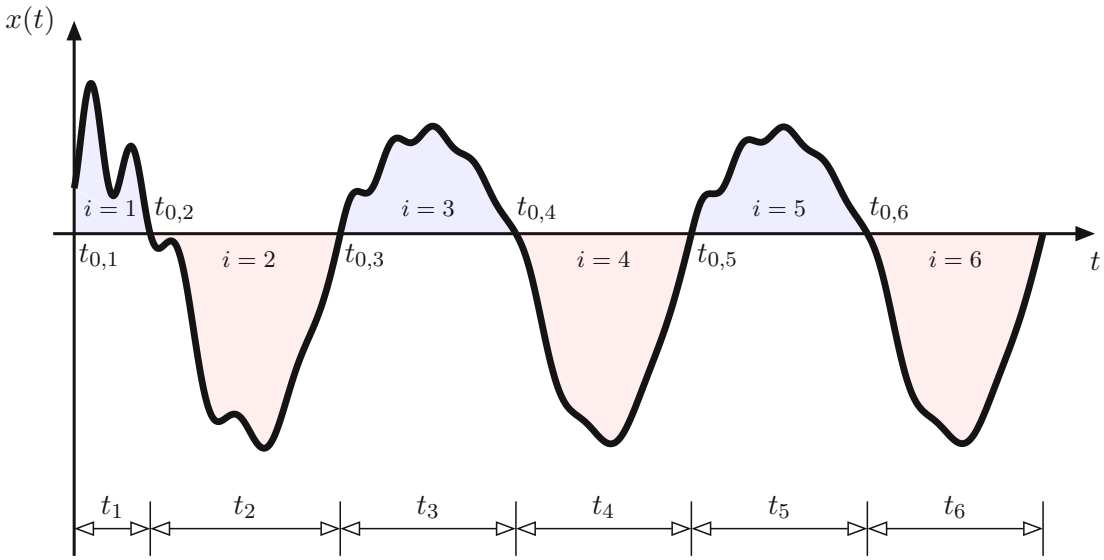

Fig. 2.4: Response of the bilinear elastic oscillator due to cosine harmonic force

Since the solution represented by Eq. (2.43) is defined separately for each specific-cycle, with time ranging from zero to the end time denoted by t_i, it is necessary to determine the initial conditions of the considered displacement segment i. Due to the fact that the displacement segment begins at the transition time $t_{0,i}$, where the displacement reaches zero, the only initial condition that needs to be determined is the velocity. This initial velocity can be derived from the previous $i-1$ specific-cycle at the end time, indicated by t_{i-1}. The following expression for determining the initial velocity is obtained by differentiating Eq. (2.43) with respect to time and specializing for the previous specific-cycle at time $t = t_{0,i}$

$$\dot{x}_{0,i} = \dot{x}_{i-1}(t_{i-1}) = -\zeta_{i-1}\,\omega_{0,i-1}\,e^{-\zeta_{i-1}\omega_{0,i-1}t_{i-1}}\Big(A_{i-1}\cos\omega_{D,i-1}t_{i-1} + B_{i-1}\sin\omega_{D,i-1}t_{i-1}\Big)$$
$$+ e^{-\zeta_{i-1}\omega_{0,i-1}t_{i-1}}\omega_{D,i-1}\Big(-A_{i-1}\sin\omega_{D,i-1}t_{i-1} + B_{i-1}\cos\omega_{D,i-1}t_{i-1}\Big)$$
$$+ \nu\Big(-C_{i-1}\sin\nu t_{i-1} + D_{i-1}\cos\nu t_{i-1}\Big) \qquad i = 2, 3, ... \tag{2.44}$$

where the duration of the specific-cycle $i-1$ is defined by the time difference between the transition times $t_{0,i}$ and $t_{0,i-1}$, given by

$$t_{i-1} = t_{0,i} - t_{0,i-1} \tag{2.45}$$

With the initial conditions defined for the i^{th} displacement domain, the focus now shifts to the particular solution, which is given by

$$x_{p,i}(t) = C_i\cos\nu(t - t_{0,i}) + D_i\sin\nu(t - t_{0,i}) \tag{2.46}$$

The velocity corresponding to the i^{th} specific-cycle is determined by differentiating this equation with respect to time, yielding

$$\dot{x}_{p,i}(t) = \nu\Big[-C_i\sin\nu(t - t_{0,i}) + D_i\cos\nu(t - t_{0,i})\Big] \tag{2.47}$$

As the solution is formulated separately for each specific-cycle, ensuring the continuity of displacement and velocity at each transition time point becomes crucial. To maintain this continuity, the coefficients of the particular solution are adjusted by equating the displacement and velocity of the particular solution at the beginning of the i^{th} specific-cycle with their counterparts obtained from the particular solution of the corresponding linear case. These oscillate linearly throughout the entire duration, starting from $t = 0$ to the considering transition time $t_{0,i}$. In this context, the continuity can be preserved according to the following conditions

$$x_{p,i}(t = t_{0,i}) = x_{0,i}(t = t_{0,i}) \tag{2.48a}$$

$$\dot{x}_{p,i}(t = t_{0,i}) = \dot{x}_{0,i}(t = t_{0,i}) \tag{2.48b}$$

Here, $x_{0,i}(t = t_{0,i})$ and $\dot{x}_{0,i}(t = t_{0,i})$ denote the linear displacement and velocity, respectively, specialized for $t = t_{0,i}$. These responses are determined by the properties of the system within i^{th} specific-cycle, vibrating linearly from time zero to the considered time $t_{0,i}$. They can be generally written for an arbitrary time t as

$$x_{0,i}(t) = C_{0,i}\cos\nu t + D_{0,i}\sin\nu t \tag{2.49a}$$

$$\dot{x}_{0,i}(t) = \nu\Big(-C_{0,i}\sin\nu t + D_{0,i}\cos\nu t\Big) \tag{2.49b}$$

By substituting these equations along with the second time derivative, into Eq. (2.42), two algebraic equations are obtained by equating coefficients, which are then solved to determine the following coefficients

$$C_{0,i} = \frac{\left(\omega_{0,i}^2 - \nu^2\right)}{\Delta_i}\frac{p_0}{m} \qquad D_{0,i} = \frac{2\zeta_i\,\omega_{0,i}\,\nu}{\Delta_i}\frac{p_0}{m} \tag{2.50}$$

where Δ_i represents the determinant of the coefficient matrix, as defined in [29, 59], which is given by the following expression

$$\Delta_i = \left(\omega_{0,i}^2 - \nu^2\right)^2 + \left(2\zeta_i\omega_{0,i}\nu\right)^2 = \omega_{0,i}^4\left\{\left[1 - \left(\frac{\nu}{\omega_{0,i}}\right)^2\right]^2 + \left[2\zeta_i\left(\frac{\nu}{\omega_{0,i}}\right)\right]^2\right\} \tag{2.51}$$

Here, $\omega_{0,i}$ and ζ_i are defined according to Eqs. (2.15) and (2.16), depending on the sign of the displacements within the first specific-cycle. Finally, by specializing Eqs. (2.46), (2.47) and (2.49) for $t = t_{0,i}$, the continuity conditions according to Eqs. (2.48) lead to the following expressions for determining the coefficients of the particular solution

$$C_i = C_{0,i}\cos\nu t_{0,i} + D_{0,i}\sin\nu t_{0,i} \tag{2.52a}$$

$$D_i = -C_{0,i}\sin\nu t_{0,i} + D_{0,i}\cos\nu t_{0,i} \tag{2.52b}$$

Based on these coefficients, upon evaluating Eq. (2.43) and its time derivative at the beginning of the specific-cycle, i.e., at the transition time $t_{0,i}$, the coefficients A_i and B_i are defined as follows

$$A_i = \begin{cases} x_0 - C_1 & i = 1 \\ -C_i & i \geq 2 \end{cases} \tag{2.53a}$$

$$B_i = \frac{1}{\omega_{D,i}}\left(\dot{x}_{0,i} + \zeta_i\omega_{0,i}A_i - \nu D_i\right) \tag{2.53b}$$

where x_0 denotes the initial displacement of the first displacement domain at $t = 0$. As indicated by the definition of the coefficient A_i, the specific-cycles for i greater than one lack this initial displacement, as the displacement is zero at the transition times. To progress from the i^{th} specific-cycle to the subsequent one, denoted by $i + 1$, the new transition time $t_{0,i+1}$ must be determined by solving the nonlinear equation provided by Eq. (2.43) for t_i. After obtaining the duration of the i^{th} specific cycle, denoted by t_i, the desired transition time is subsequently determined by

$$t_{0,i+1} = t_{0,i} + t_i \tag{2.54}$$

Once the new transition time is determined, the procedure for evaluating the response in the next segment can continue by replacing i with $i + 1$.

2.4 Example

This example shows how the bilinear properties of the oscillator's spring influence its dynamic response when subjected to initial conditions and a harmonic force. The relationship between the spring stiffness constants in the positive and negative displacement domains is determined by the stiffness ratio $\alpha = 4$. Furthermore, the ratio of the exciting frequency to the natural circular frequency, defined by the stiffness constant within the negative displacement domain, is $\nu/\omega_0^{(-)} = 0.25$. Additionally, the damping is included by the damping ratio $\zeta^{(-)} = 0.1$, which is specified for the negative displacement segments. The bilinear elastic oscillator at time zero is defined by the following initial displacement and velocity, respectively

$$x_0 = 0.2\,x_{st}^{(-)} \qquad \dot{x}_0 = \omega_0^{(-)}\,x_{st}^{(-)} \tag{2.55}$$

Here, $x_{st}^{(-)}$ denotes the static deformation within the negative diplacement domains, defined as

$$x_{st}^{(-)} = \frac{p_0}{k^{(-)}} \tag{2.56}$$

When considering the bilinear oscillator only subjected to these initial conditions, which induce free vibration, it is necessary to analyze the dynamic response segment by segment, as detailed in Subsection 2.2. Starting from the first specific-cycle $i = 1$, the amplitude a_1 and the phase angle ε_1 can be determined from the provided initial conditions utilizing Eqs. (2.19) and (2.20), respectively. To proceed to the next segment, the transition time $t_{0,2}$ needs to be determined according to Eq. (2.23). After the new transition time has been determined, the corresponding amplitude and phase angle are defined by using Eqs. (2.30) and (2.33). This process is recursive, and further determination of the transition times will be carried out using Eq. (2.24). Table A.1 in the Appendix summarizes the transition times, amplitudes, and phase angles for the first seven specific-cycles.

The dynamic response of the bilinear elastic oscillator over a defined time, subjected to the initial conditions, involves piecewise substitution of corresponding values from Table A.1 into Eq. (2.17). Additionally, this exact solution will be compared with results obtained using the modified Newmark's method. Based on [14], Table 2.1 presents the adjusted algorithm for obtaining the solution when a system is characterized by a bilinear elastic resisting force.

Tab. 2.1: Newmark's method, [14]

Special cases

(1) Constant average acceleration method ($\gamma = 1/2,\ \beta = 1/4$)

(2) Linear acceleration method ($\gamma = 1/2,\ \beta = 1/6$)

1.0 Initial calculations

1.1 $\ddot{x}_0 = \dfrac{p_0 - c\dot{x}_0 - f_S(x_0)}{m}$

1.2 Select Δt

1.3 $a_k = \dfrac{1}{\beta\Delta t^2}m + \dfrac{\gamma}{\beta\Delta t}c \qquad a_c = \dfrac{1}{\beta\Delta t}m + \left(\dfrac{\gamma}{\beta} - 1\right)c \qquad a_m = \left(\dfrac{1}{2\beta} - 1\right)m + \Delta t\left(\dfrac{\gamma}{2\beta} - 1\right)c$

2.0 Calculations for each time step, $i = 0, 1, 2, ...$

2.1 $\hat{p}_{i+1} = p_{i+1} + a_k x_i + a_c \dot{x}_i + a_m \ddot{x}_i$

2.2 $\hat{k} = k(x_i) + a_k$

2.3 $x_{i+1} = \dfrac{\hat{p}_{i+1}}{\hat{k}}$

2.4 $\dot{x}_{i+1} = \dfrac{\gamma}{\beta\Delta t}\Big(x_{i+1} - x_i\Big) + \left(1 - \dfrac{\gamma}{\beta}\right)\dot{x}_i + \Delta t\left(1 - \dfrac{\gamma}{2\beta}\right)\ddot{x}_i$

2.5 $\ddot{x}_{i+1} = \dfrac{1}{\beta\Delta t^2}\Big(x_{i+1} - x_i\Big) - \dfrac{1}{\beta\Delta t}x_i - \left(\dfrac{1}{2\beta} - 1\right)\ddot{x}_i$

3.0 Repetition for the next time step

Replace i with $i + 1$ and implement steps 2.1 to 2.5 for the next time step.

Both solutions for free vibration of the bilinear elastic oscillator are graphically illustrated in Fig. 2.5, showing identical dynamic responses. Furthermore, two linear cases are also included to demonstrate the difference between these cases during vibration. As can be seen, significant

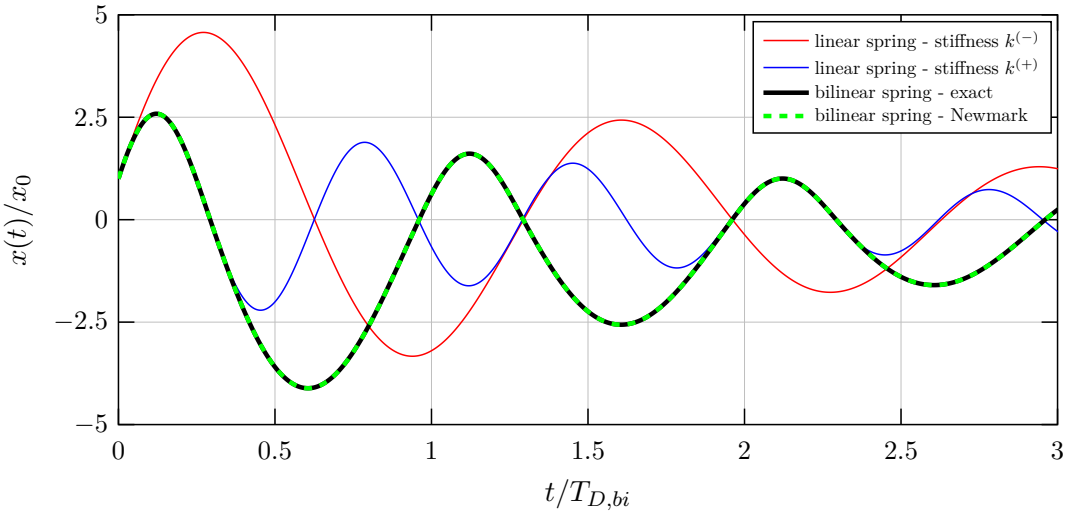

Fig. 2.5: Free-vibration response, time normalized by $T_{D,bi}$

differences in amplitude exist between the bilinear and linear responses due to variations in spring properties. Remarkably, the response of the bilinear oscillator completely coincides with the linear response of the system characterized by the stiffness constant $k^{(+)}$ within the first specific-cycle. Conversely, when the initial conditions dictate that the vibration begins from the negative displacement domain, the bilinear oscillator mirrors the response of the linear system defined by the stiffness constant $k^{(-)}$ within the first specific-cycle. Contrary to Fig. 2.5, which presents responses over time normalized by the natural period of vibration of the bilinear system as defined in Eq. (2.35), Fig. 2.6 illustrates the same responses over time, but each normalized by its own natural period of vibration, denoted by T_D.

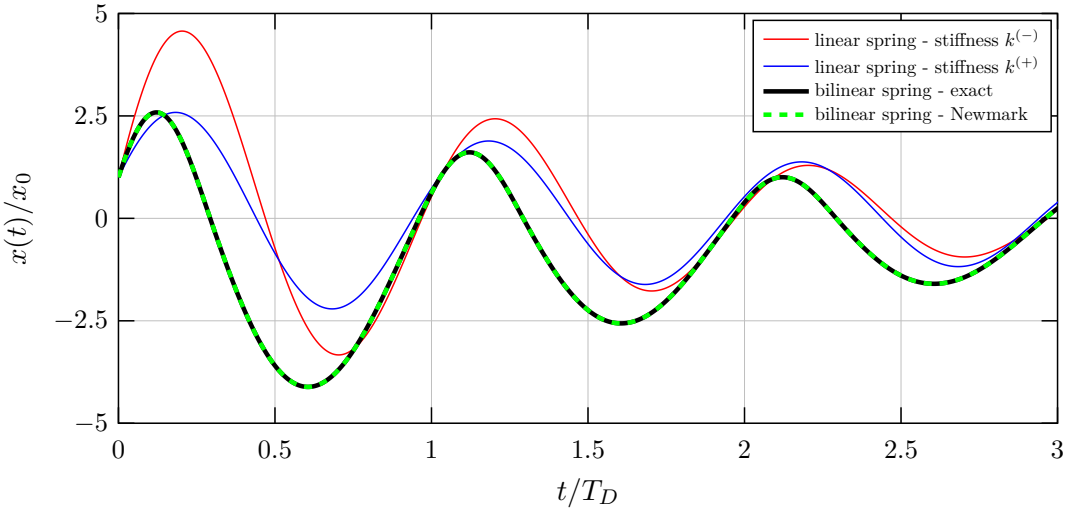

Fig. 2.6: Free-vibration response, time normalized by T_D

Fig. 2.6, the oscillation variation within the natural period of vibration is depicted for both the linear and bilinear cases. However, Fig. 2.7 demonstrates the effect of the difference in spring stiffnesses between positive and negative displacements, characterized by the stiffness ratio α, on the dynamic response.

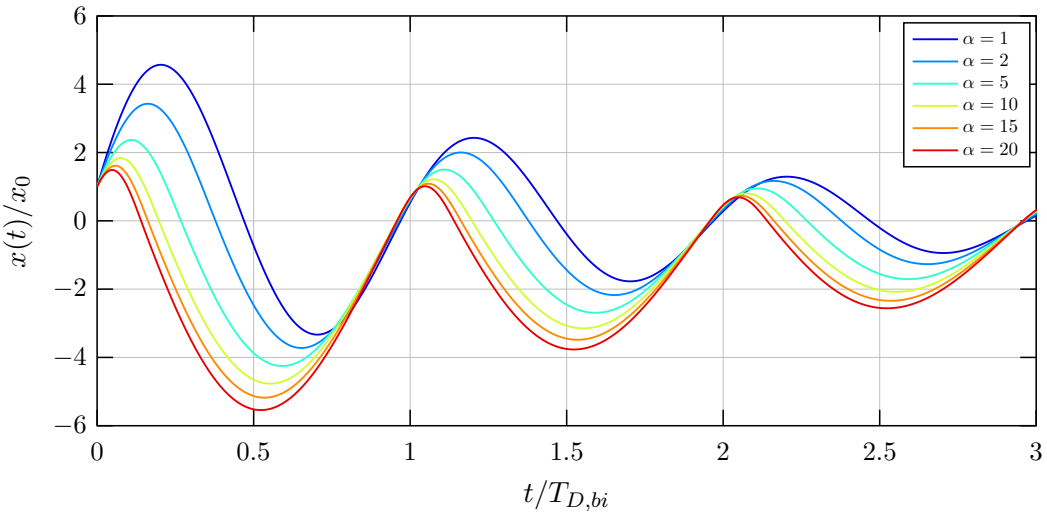

Fig. 2.7: Influence of the stiffness ratio α on free-vibration response

As the stiffness ratio increases, it becomes evident that both the amplitude and specific-cycle duration of the positive displacement domains decrease in comparison to those of the negative displacement domain.

In addition, Fig. 2.8 provides a visual representation of the free vibration responses resulting from initial conditions depicted in a phase plane. The displacement and velocity are normalized by their corresponding initial values, namely, initial displacement x_0 and initial velocity $\dot{x}_0$.

Similarly, the vibration response due to harmonic excitation can be obtained piecewise, as detailed in Subsection 2.3. Given the circular frequency ratio $\nu/\omega_0^{(-)}$, damping ratio $\zeta^{(-)}$, and stiffness ratio α, the coefficients of the particular solution for the first specific-cycle C_1 and D_1 are determined using Eq. (2.52), where $t_{0,1} = 0$ as initial time and coefficients $C_{0,1}$ and $D_{0,1}$ can be expressed through static displacement $x_{st}^{(-)}$. Having determined C_1 and D_1, the coefficents A_1 and B_1 can be computed according to Eq. (2.53), also in terms of $x_{st}^{(-)}$. Since the coefficients have been obtained, the dynamic response of the bilinear oscillator can be plotted until the transition time $t_{0,2}$ is reached. However, the transition time from the first positive displacement segment to the second negative segment, denoted by $t_{0,2}$, is a priori unknown and can be determined by solving the nonlinear Eq. (2.43) in terms of $t_{0,2}$. At this transition time, Eq. (2.44) specifies the new initial velocity as the updated initial conditions for the subsequent displacement segment. The new initial displacement is naturally set to zero. With these updated initial conditions, the entire process can be repeated recursively. Tables in the Appendix, labeled as Table A.2 and Table A.3, provide a summary of the normalized transition times and coefficients for both the linear case with $\alpha = 1$ and the bilinear case with $\alpha = 4$. In this analysis, the first fifteen specific cycles are considered.

The dynamic response of the bilinear elastic oscillator under harmonic excitation throughout the considered time is graphically presented in Fig. 2.9. Similar to the free vibration, the solution is compared with results obtained utilizing the modified Newmark's method, as outlined in the algorithm presented in Table 2.1. Additionally, two linear cases are illustrated in the same figure.

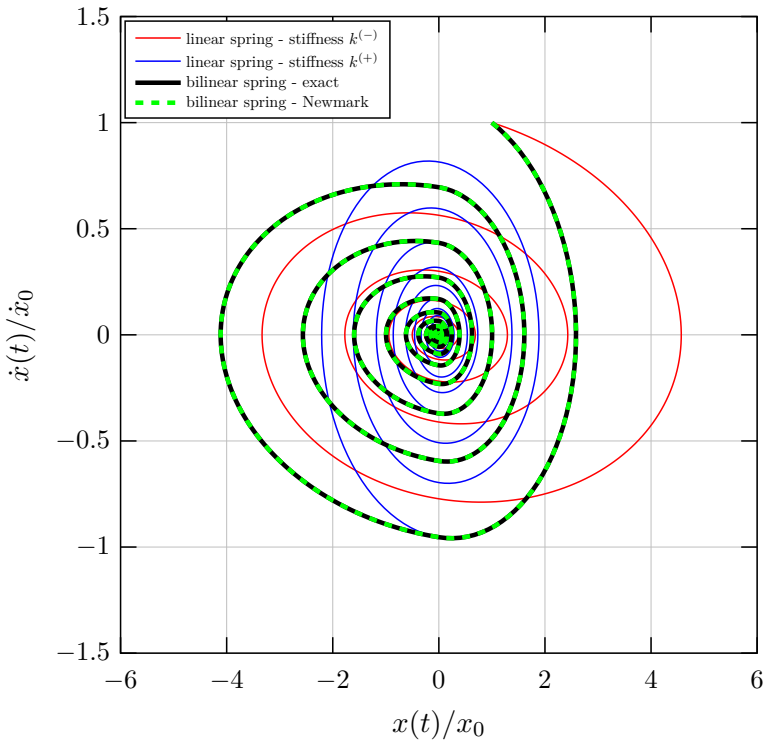

(a)

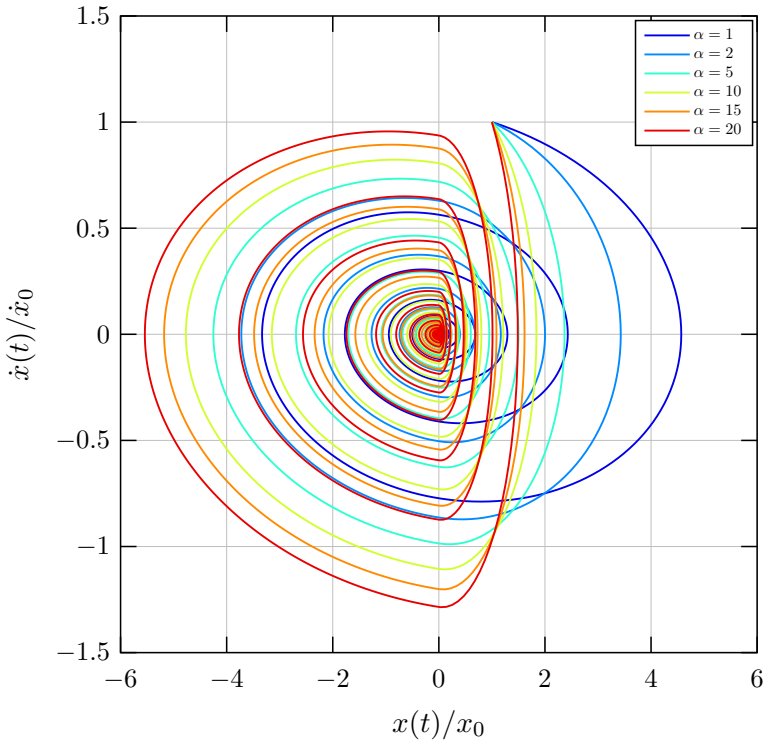

(b)

Fig. 2.8: Phase plane of free vibration (a) linear and bilinear systems (b) bilinear system with different stiffness ratios α

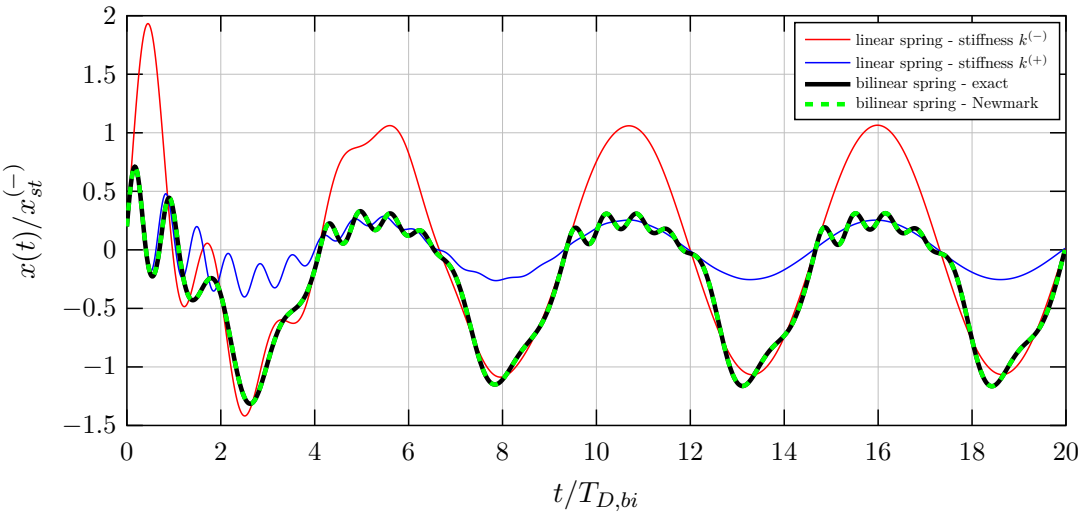

Fig. 2.9: Response to harmonic force; $\nu/\omega_{0,bi} = 0.1875$

This figure shows that the exact solution perfectly coincides with the one obtained using the Newmark method. Additionally, it becomes evident that as time progresses, the transient response diminishes, with only the steady-state response remaining. When considering the steady-state response, the bilinear oscillator tends to coincide with the corresponding linear response with identical spring stiffness properties. More precisely, within positive displacement segments, it tends towards the blue line, indicative of the response of a linear oscillator characterized by spring stiffness $k^{(+)}$. Similarly, within the negative displacement domain, it tends towards the red line, representing the response of a linear oscillator with spring stiffness $k^{(-)}$. Thus, the dynamic response of the bilinear oscillator represents a combination of two linear responses, contributing to its overall behavior. However, the response of the bilinear elastic oscillator contains more than one harmonic function in both displacement domains, particularly evident within the positive displacement domain. This characteristic arises from the varying elastic resisting force during vibration and indicates a nonlinear phenomenon. Precisely, the steady-state response consists of a particular solution with the same frequency as the excitation and free vibration term with the corresponding natural frequency. Fig. 2.10 graphically illustrates the contribution of each part of the solution to the resulting response of the system within specific-cycle i. More precisely, the coefficients listed in Tables A.2 and A.3 are visually depicted in order to demonstrate their influence on the dynamic response during vibration. The blue columns indicate the normalized coefficients of the linear solution when $\alpha = 1$, while the red columns represent the normalized coefficients of the bilinear oscillator's solution when $\alpha = 4$. From Fig. 2.10, it is evident how the coefficients A_i and B_i decrease in the linear case as the specific cycle progresses, i.e., over time. These coefficients determine the transient vibration, which gradually diminishes over time until it becomes negligible. Because of the piecewise nature of the solution formulation, where the initial displacement is set to zero at each transition time, the coefficients D_i dominate over C_i, indicating a sinusoidal function as the response within displacement segments. However, when considering the bilinear oscillator with a stiffness ratio of $\alpha = 4$, it is noteworthy that the coefficients A_i and B_i, which define the free vibration, also contribute to the steady-state response. This implies that the system, besides the excitation frequency, also oscillates freely with the corresponding natural frequency, as previously mentioned. Although the coefficients C_i are also present, their influence on the response is smaller than D_i. Similarly, Figs. 2.11 and 2.12 illustrate the responses and coefficient contributions for three values of excitation frequency.

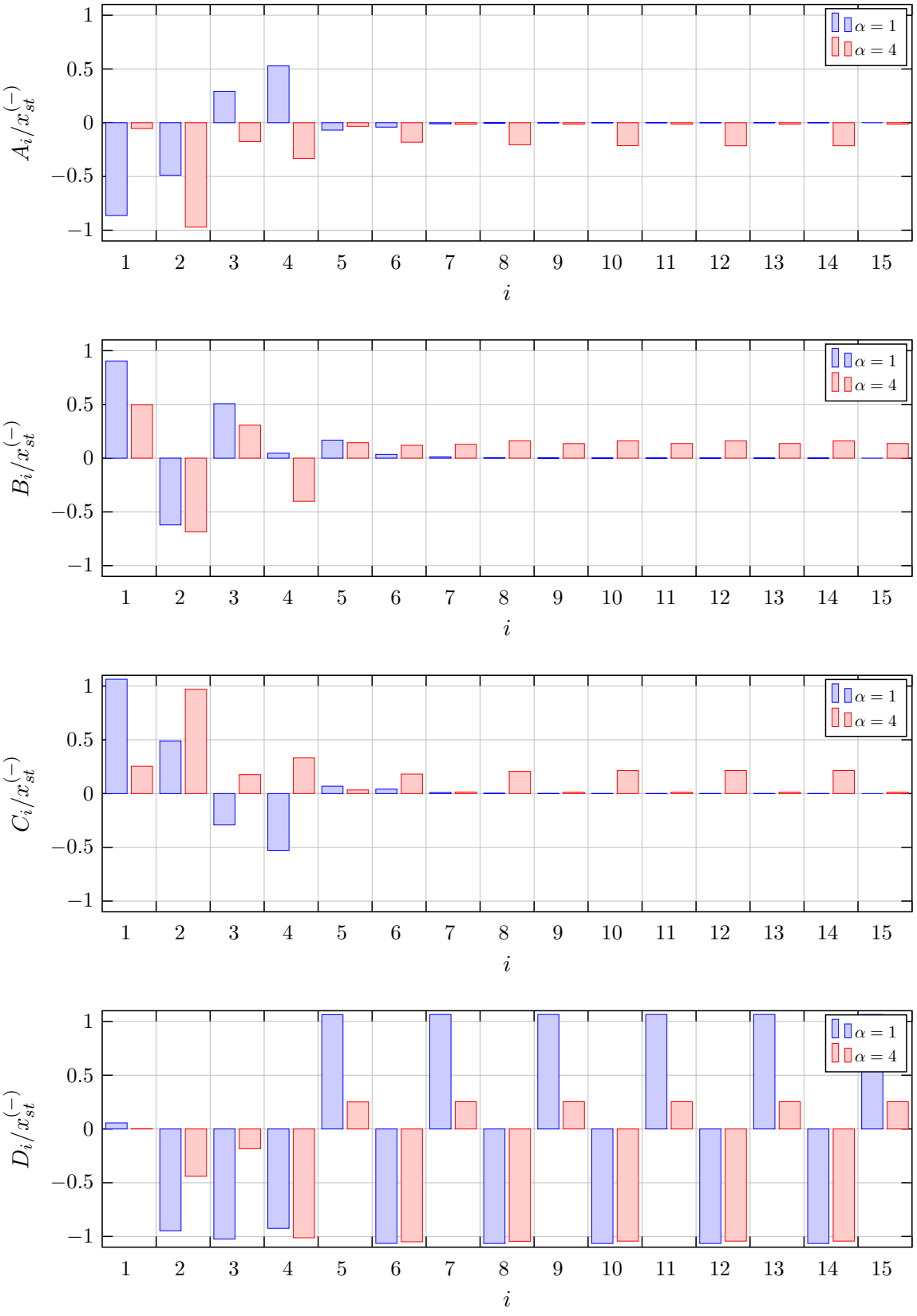

Fig. 2.10: Variation of coefficients with specific-cycle; $\nu/\omega_{0,bi} = 0.1875$

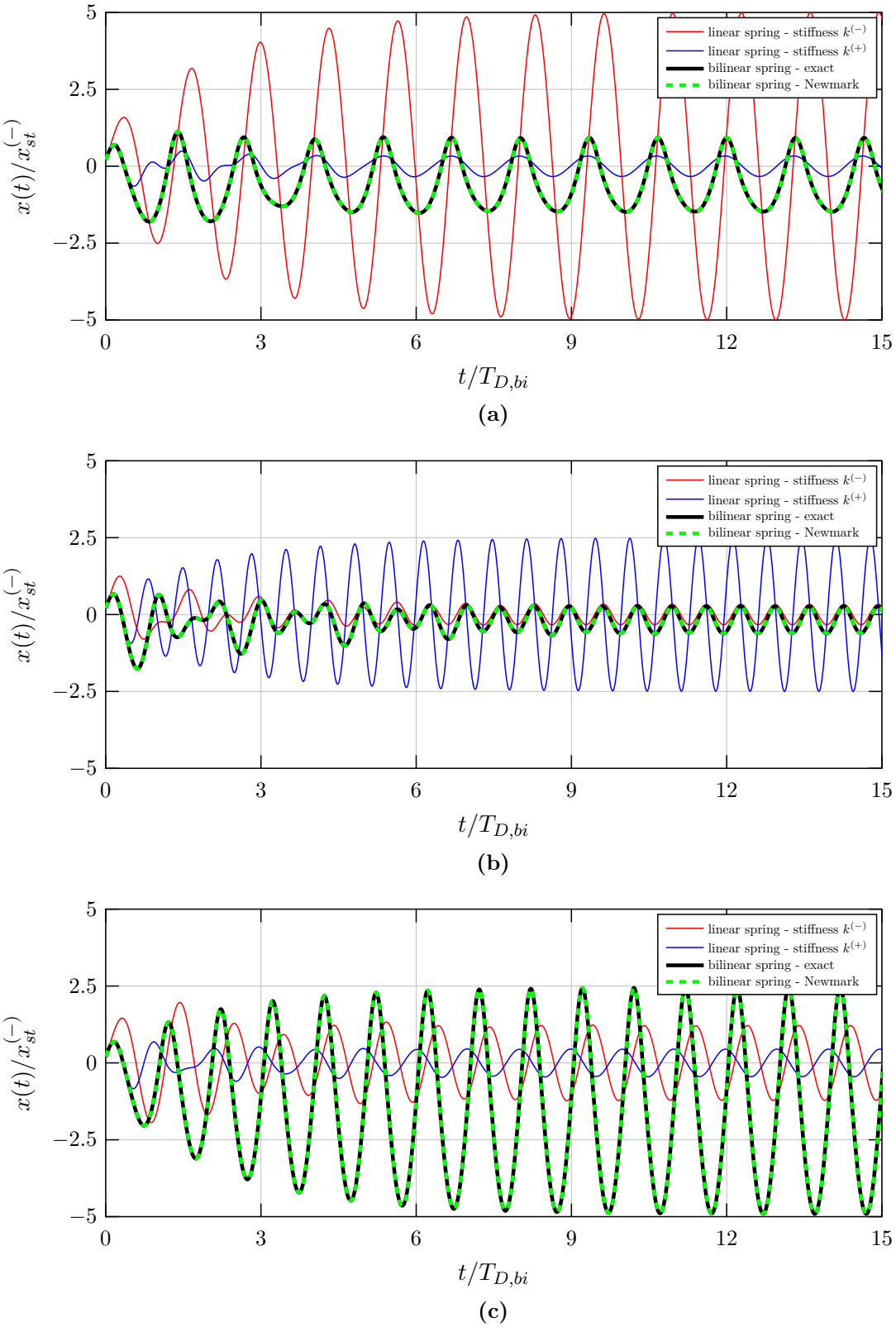

Fig. 2.11: Response to harmonic force $p(t) = p_0 \cos \nu t$ for three values of the exciting frequency (a) $\nu = \omega_0^{(-)}$ (b) $\nu = \omega_0^{(+)}$ (c) $\nu = \omega_{0,bi}$

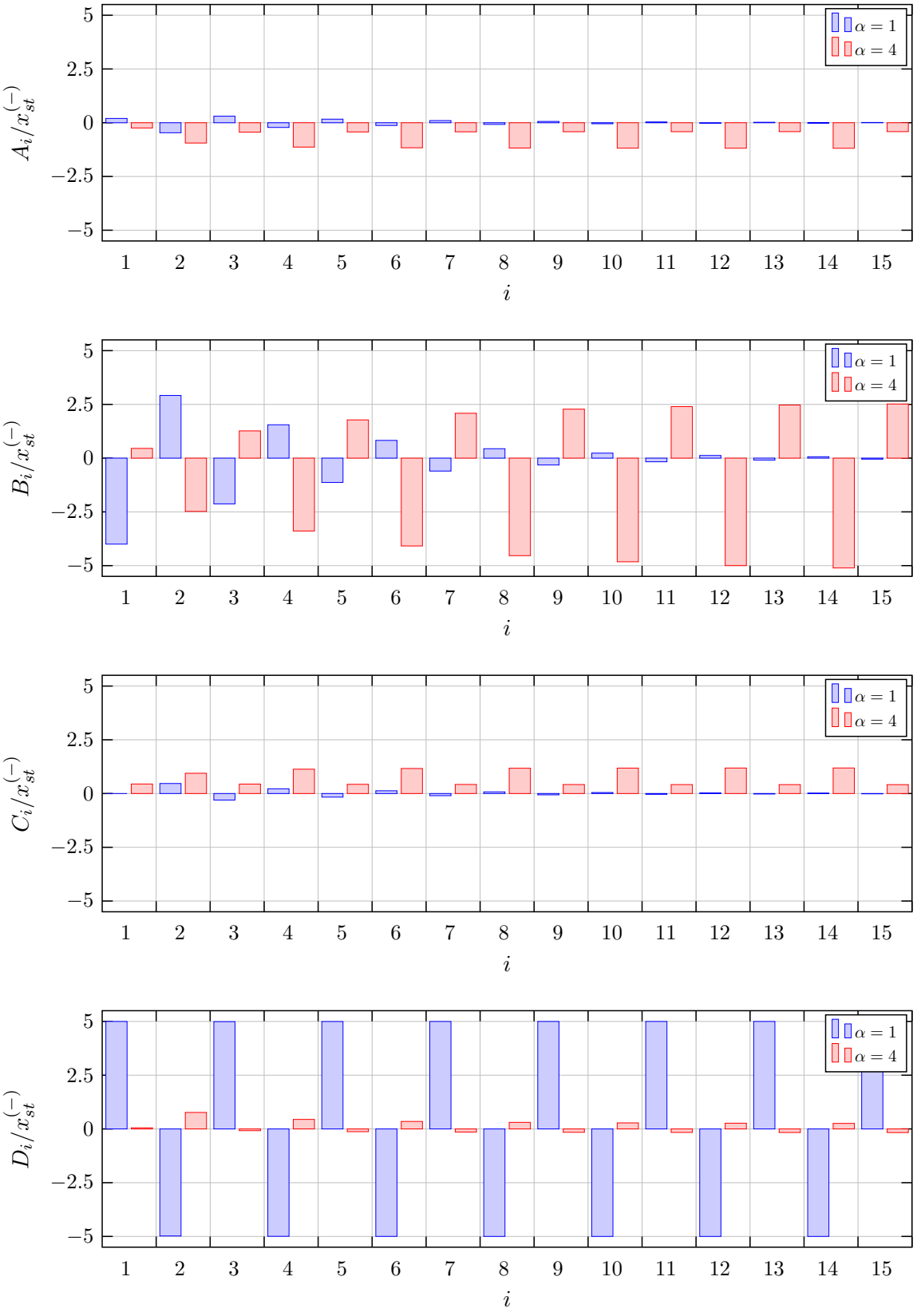

Fig. 2.12: Variation of coefficients with specific-cycle; $\nu = \omega_{0,bi}$

Fig. 2.11a shows the dynamic response of two linear and bilinear systems when the excitation circular frequency matches the natural circular frequency of the oscillator with spring stiffness $k^{(-)}$, denoted by $\omega_0^{(-)}$. As expected, the amplitudes of this linear oscillator are larger than those of the other two systems. Similarly, Fig. 2.11b depicts the responses due to harmonic excitation with a circular frequency identical to the natural circular frequency of the second linear system, characterized by the spring stiffness $k^{(+)}$. However, when the excitation circular frequency matches the circular frequency $\omega_{0,bi}$, the amplitudes of the nonlinear response significantly exceed those of both linear responses. Remarkably, this nonlinear response of the bilinear oscillator attains the maximum amplitudes observed in the preceding two cases, namely, when the excitation circular frequency equals the natural circular frequencies of the linear systems. In this case, when $\nu = \omega_{0,bi}$, the contributions of coefficients on linear and nonlinear responses in each specific-cycle are also graphically illustrated in Fig. 2.12. It is crucial to highlight that, in the case of the bilinear oscillator, maximum amplitudes arise primarily from free vibration, as evidenced by the dominant coefficients B_i. More precisely, the influence of the initial velocity at each transition time, which induces free vibration, significantly outweighs the contribution of the solution associated with the excitation frequency. In this case, the influence of the stiffness ratio α on dynamic response is presented in Fig. 2.13 below.

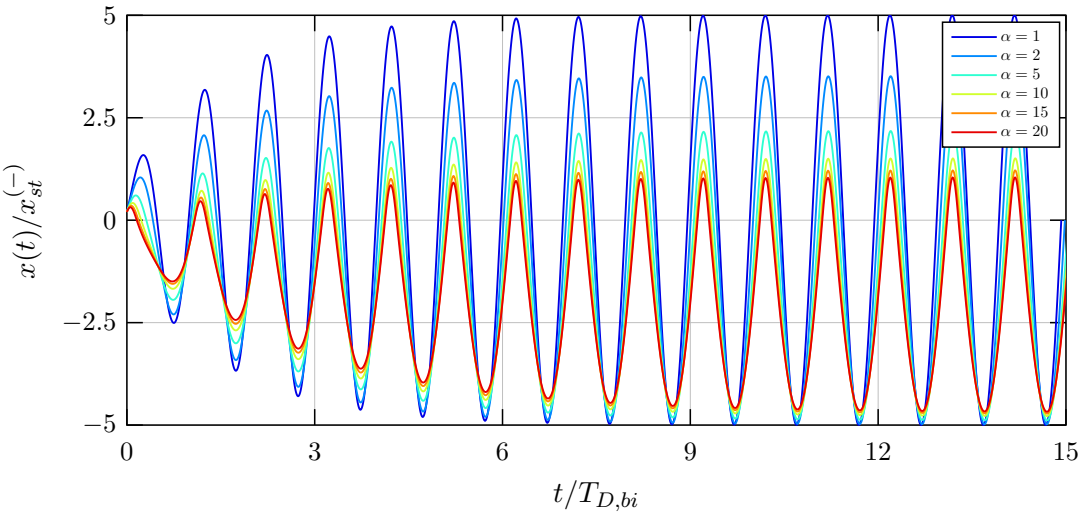

Fig. 2.13: Influence of the stiffness ratio α on vibration response; $\nu = \omega_{0,bi}$

It is clear from this figure that increasing the stiffness ratio results in decreasing amplitudes, particularly in the positive displacement domain when the spring stiffness $k^{(-)}$ is used as a reference and remains constant. The nonlinear effect becomes more significant as the stiffness ratio α progresses.

Additionally, Figs. 2.14 and 2.15 provide the system responses in a phase plane for three different values of excitation frequencies and six different values of the stiffness ratio, as previously analyzed in the time domain.

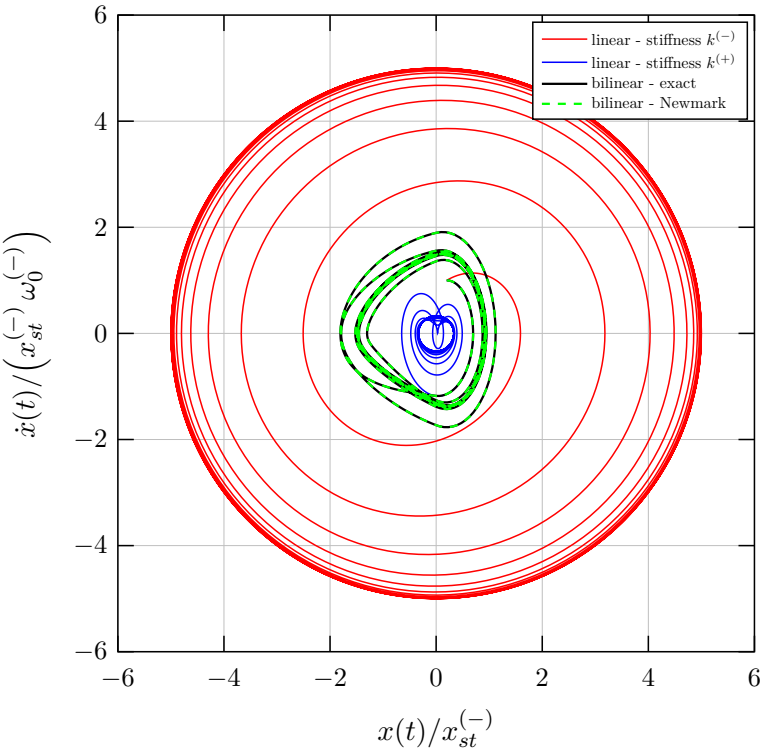

(a)

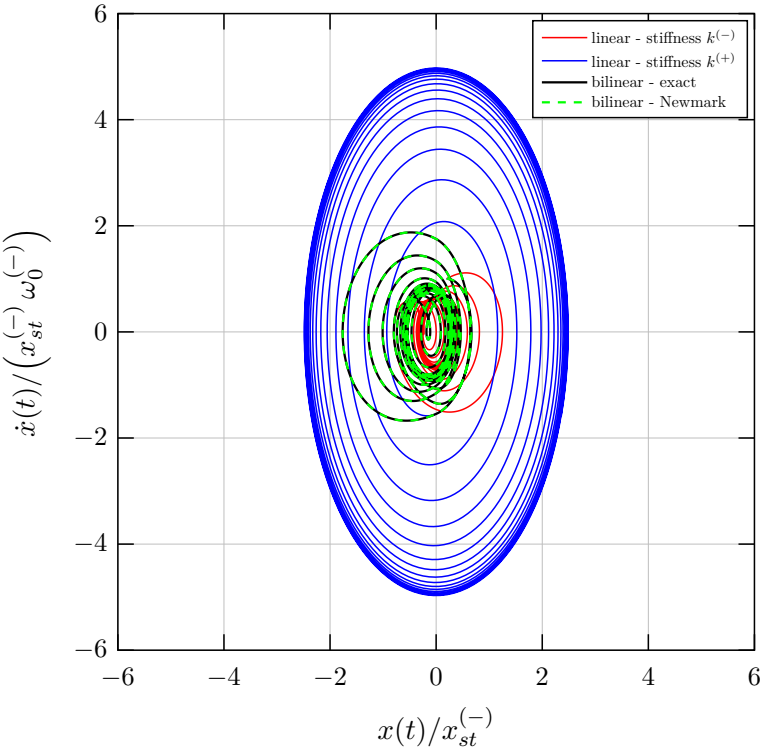

(b)

Fig. 2.14: Phase plane of harmonic vibration (a) $\nu = \omega_0^{(-)}$ (b) $\nu = \omega_0^{(+)}$

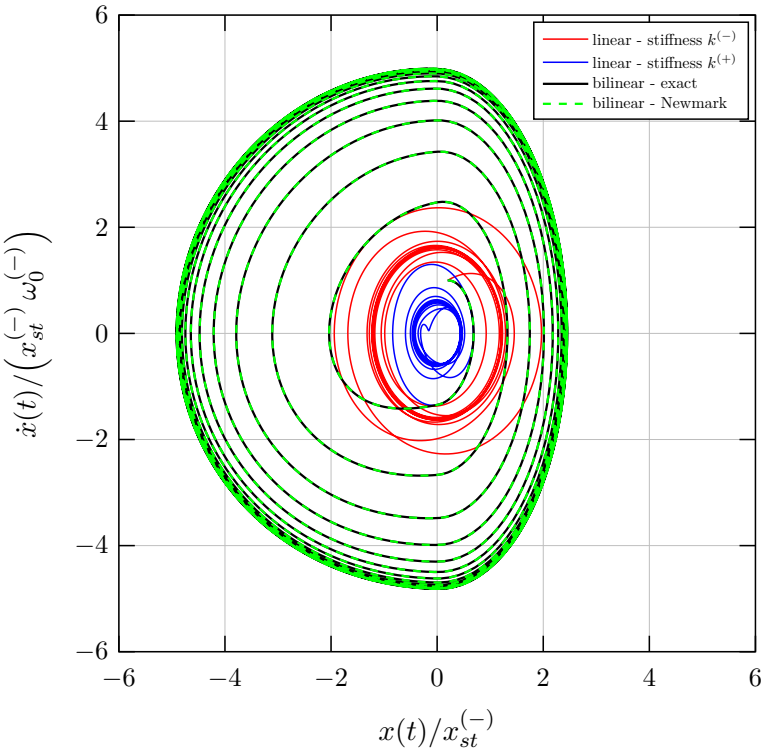

(a)

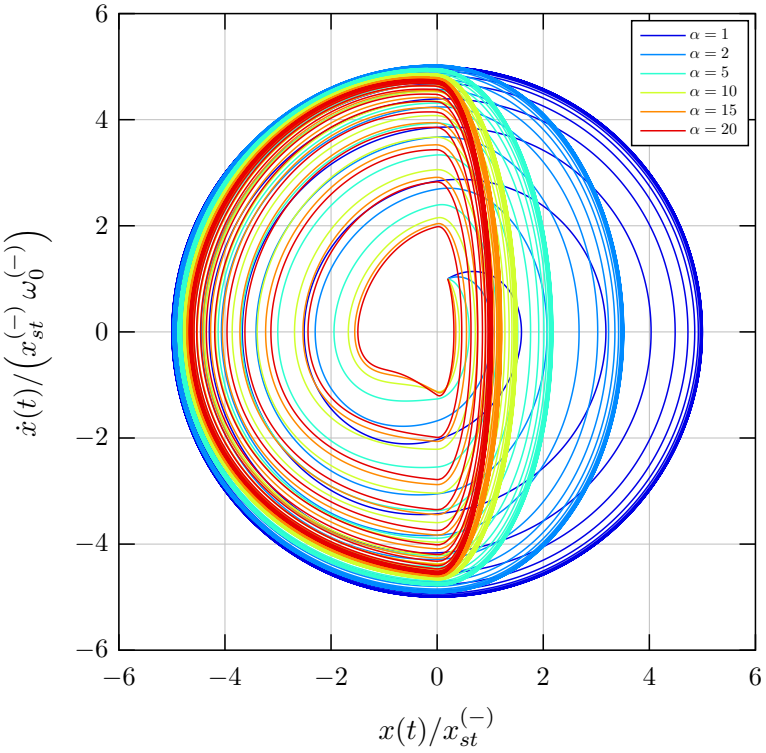

(b)

Fig. 2.15: Phase plane of harmonic vibration (a) $\nu = \omega_{0,bi}$ (b) influence of stiffness ratio α

Chapter 3

Bimodular structure

This chapter presents a study on the mechanical modeling of a continuous bimodular beam rigid in shear and explores the influence of elastic properties and specific cross-sections on the stiffness of the structure, consequently affecting the dynamic response of the planar straight bimodular beam under time-varying excitation. After the introduction of kinematic relations in Section 3.1, the strain-displacement and constitutive relations are derived based on these kinematic assumptions. The derivations for each are detailed in Sections 3.2 and 3.3, respectively. The equation of motion for the flexural vibration is formulated by modeling the bimodular beam as effective two-layer laminates with a discontinuous neutral axis, as derived in Section 3.4. Finally, in Section 3.5, various cross-sections, including rectangular, isosceles triangular, trapezoidal, and T-shaped cross-sections, are considered to illustrate their influence on the position of the neutral axis and stiffnesses, and therefore, on the behavior of the bimodular beam during a vibrational process.

3.1 Kinematic relations

Consider a homogeneous straight beam of length l with a constant cross-sectional area A and mass density ρ, undergoing cylindrical bending in the x-ζ plane. Neglecting changes in the cross-sectional dimensions caused by external loads and assuming that all points of a cross-section experience the same ζ-direction displacement, the transverse displacement in the ζ-direction can be written as

$$w(x, \zeta, t) = w(x, t) \tag{3.1}$$

Here, x denotes the axial beam coordinate, and t is time. The Cartesian (x, η, ζ) -coordinate system is positioned at the geometrical centroid of the cross-section, denoted by S, as illustrated in Fig. 3.1 below.

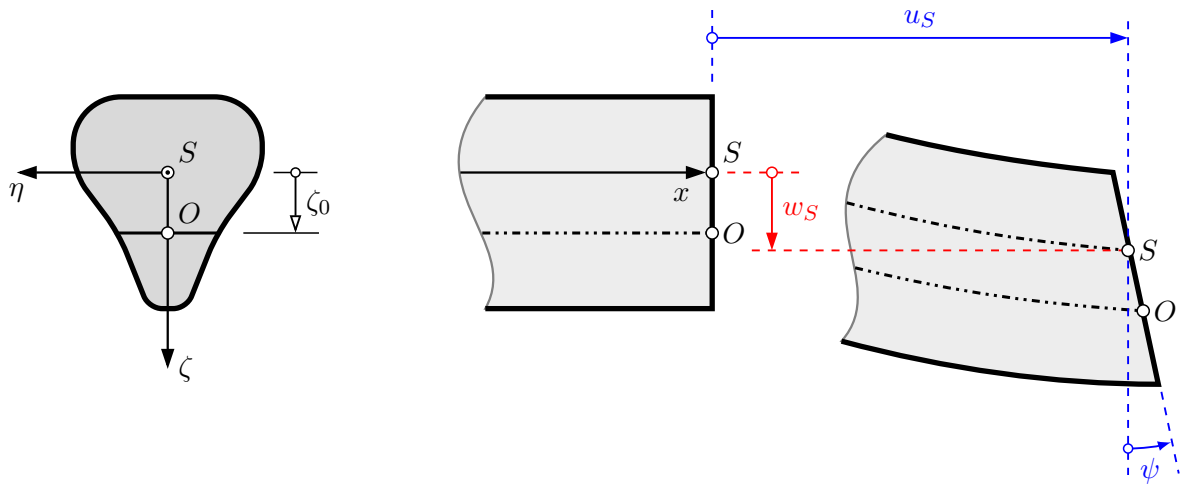

Fig. 3.1: Cross-section of a beam at x in its initial (time "$t = 0$") and deformed state (time "t")

Assuming that the cross-section remains plane during deformation, the axial displacement can be described as the sum of the displacement of the geometrical centroid S along x-axis in the positive x-direction, represented by term $u_S(x,t)$, and displacement due to rotation about the η-axis, denoted as $\psi(x,t)$, given by

$$u(x,\zeta,t) = u_S(x,t) + \zeta\psi(x,t) \tag{3.2}$$

However, in the case of a beam made from bimodular material, the elastic and geometrical centroids no longer coincide under pure bending conditions. Therefore, a new reference point is chosen precisely where the stress, as well as the strain, are equal to zero due to pure bending. The axis passing through that new reference point, denoted by O, is the neutral axis due to bending, known as the bending or flexural neutral axis. Now, the axial displacement of the geometrical centroid $u_S(x,t)$ can be expressed by the axial displacement of the new reference point on the bending neutral axis and displacement induced by the rotation of the cross-section as

$$u_S(x,t) = u_0(x,t) - \zeta_0\psi(x,t) \tag{3.3}$$

where $u_0(x,t)$ is the axial displacement of the reference point O, and ζ_0 represents the position of the bending neutral axis. Substituting Eq. (3.3) in Eq. (3.2) gives the axial displacement of an arbitrary point of the beam

$$u(x,\zeta,t) = u_0(x,t) - \Big(\zeta_0 - \zeta\Big)\psi(x,t) \tag{3.4}$$

According to Bernoulli-Euler beam theory, where shear deformation is neglected, the cross-section remains not only plane, but also orthogonal to the deformed axis of the beam during the vibrational process. In this case, the effect of transverse shear deformation can be neglected, implying that the rotation of the cross-section is equal to the negative slope of the beam axis

$$\psi(x,t) = -\frac{\partial w(x,t)}{\partial x} \tag{3.5}$$

Consequently, the in-plane displacement field, expressed by the axial displacement and transverse displacement in the ζ-direction, can be written as follows

$$u(x,\zeta,t) = u_0(x,t) + \Big(\zeta_0 - \zeta\Big)\frac{\partial w(x,t)}{\partial x} \qquad\qquad w(x,\zeta,t) = w(x,t) \tag{3.6}$$

3.2 Strain-displacement relations

Based on the kinematic assumptions and the resulting displacement field according to Eq. (3.6), the components of the linear strain tensor can be obtained, leading to the following uniaxial strain state or, more specifically, to the normal strain in the longitudinal beam direction

$$\varepsilon_x(x,\zeta,t) = \frac{\partial u(x,\zeta,t)}{\partial x} = \frac{\partial u_0(x,t)}{\partial x} + \Big(\zeta_0 - \zeta\Big)\frac{\partial^2 w(x,t)}{\partial x^2} \tag{3.7}$$

This axial strain is actually the sum of the extensional strain along the longitudinal axis through point O and the strain due to bending, commonly referred to as the bending or flexural strain. Eq. (3.7) can be rewritten as

$$\varepsilon_x(x,\zeta,t) = \varepsilon_0(x,t) - \Big(\zeta_0 - \zeta\Big)\kappa(x,t) \tag{3.8}$$

by introducing the following notation

$$\varepsilon_0(x,t) = \frac{\partial u_0(x,t)}{\partial x} \qquad \kappa(x,t) = \frac{\partial \psi(x,t)}{\partial x} = -\frac{\partial^2 w(x,t)}{\partial x^2} \tag{3.9}$$

where $\varepsilon_0(x,t)$ represents the extensional strain along the bending neutral plane, and $\kappa(x,t)$ is the curvature.

3.3 Constitutive relations

Knowing the strain field, the sole non-zero stress, i.e., the axial normal stress, in a linear elastic beam is determined by the generalized Hooke's law, expressed as follows

$$\sigma_x(x,\zeta,t) = E(\zeta)\varepsilon_x(x,\zeta,t) \tag{3.10}$$

where $E(\zeta)$ is the time-independent elastic or Young's modulus. This equation after substituting Eq. (3.7) becomes

$$\sigma_x(x,\zeta,t) = E(\zeta)\left[\varepsilon_0(x,t) + \left(\zeta_0 - \zeta\right)\frac{\partial^2 w(x,t)}{\partial x^2}\right] \tag{3.11}$$

For the assumed beam, the normal stress resultant $N(x,t)$ and bending moment resultant $M(x,t)$ are given by spatial integration over the cross-sectional area A as

$$N(x,t) = \int_A \sigma_x(x,\zeta,t)\,\mathrm{d}A = \overline{A}\,\varepsilon_0(x,t) + \left(\overline{A}\zeta_0 - B\right)\frac{\partial^2 w(x,t)}{\partial x^2} \tag{3.12a}$$

$$M(x,t) = \int_A \sigma_x(x,\zeta,t)\,\zeta\,\mathrm{d}A = B\,\varepsilon_0(x,t) + \left(B\zeta_0 - D\right)\frac{\partial^2 w(x,t)}{\partial x^2} \tag{3.12b}$$

where $\overline{A}$, B and D represent extensional, bending-extensional coupling and bending stiffness, respectively, defined as

$$\overline{A} = \int_A E\,\mathrm{d}A = \int_h E(\zeta)\,b(\zeta)\,\mathrm{d}\zeta \tag{3.13a}$$

$$B = \int_A E\,\zeta\,\mathrm{d}A = \int_h E(\zeta)\,\zeta\,b(\zeta)\,\mathrm{d}\zeta \tag{3.13b}$$

$$D = \int_A E\,\zeta^2\,\mathrm{d}A = \int_h E(\zeta)\,\zeta^2\,b(\zeta)\,\mathrm{d}\zeta \tag{3.13c}$$

where h denotes a height of the cross-section, and $b(\zeta)$ represents a width expressed as function of the ζ-coordinate.

3.4 Governing equations

In this section, the partial differential equation governing the transverse vibration in ζ-direction of a straight bimodular beam subjected to an external force will be formulated based on an independent reference axis, see Fig. 3.2.

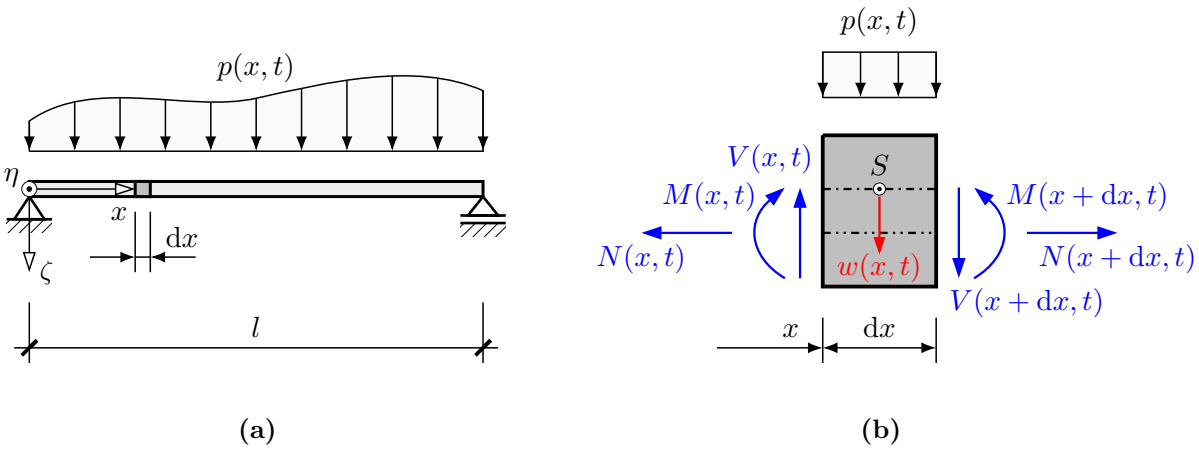

Fig. 3.2: System composed of bimodular material (a) example of beam and applied distributed force (b) free-body diagram of an infinitesimal beam element

The equation of motion can be derived by considering the free-body diagram of an infinitesimal bimodular beam element with length $\mathrm{d}x$ at a fixed time t, as presented in Fig. 3.2b. Due to the negligible longitudinal inertia and absence of external forces in x-direction, the conservation of momentum in the x-direction yields

$$-N(x,t) + N(x+\mathrm{d}x,t) = 0 \tag{3.14}$$

Conservation of momentum in the ζ-direction gives

$$-V(x,t) + p(x,t)\mathrm{d}x + V(x+\mathrm{d}x,t) = \mu \mathrm{d}x \frac{\partial^2 w(x,t)}{\partial t^2} \tag{3.15}$$

where $p(x,t)$ is the transverse load in the ζ-direction, assumed to vary arbitrarily with position and time, and μ is the mass per unit length defined as the integral of the mass density ρ over the cross-sectional area A

$$\mu = \int_A \rho \,\mathrm{d}A = \int_h \rho(x,\zeta) b(\zeta) \mathrm{d}\zeta \tag{3.16}$$

The conservation of angular momentum, under the assumption of negligible rotational inertia, leads to

$$-M(x,t) - V(x,t)\frac{\mathrm{d}x}{2} + M(x+\mathrm{d}x,t) - V(x+\mathrm{d}x,t)\frac{\mathrm{d}x}{2} = 0 \tag{3.17}$$

The expansion of the normal force $N(x+\mathrm{d}x,t)$, transverse shear force $V(x+\mathrm{d}x,t)$, and bending moment $M(x+\mathrm{d}x,t)$ in the Taylor series at point x, followed by division by $\mathrm{d}x$ and subsequently taking the limit $\mathrm{d}x \to 0$, yields the following relations

$$\frac{\partial N(x,t)}{\partial x} = 0 \tag{3.18a}$$

$$\frac{\partial V(x,t)}{\partial x} = \mu \frac{\partial^2 w(x,t)}{\partial t^2} - p(x,t) \tag{3.18b}$$

$$\frac{\partial M(x,t)}{\partial x} = V(x,t) \tag{3.18c}$$

Differentiating Eq. (3.18c) with respect to x, and replacing the partial derivative of the transverse shear force with respect to x in Eq. (3.18b) by the second partial derivative of the bending moment with respect to x gives

$$\frac{\partial^2 M(x,t)}{\partial x^2} = \mu \frac{\partial^2 w(x,t)}{\partial t^2} - p(x,t) \tag{3.19}$$

By taking the first partial derivative of the normal force $N(x,t)$ and second partial derivative of the bending moment $M(x,t)$ with respect to x, as defined in Eq. (3.12), and substituting them in Eqs. (3.18a) and (3.19), respectively, the following equations are obtained

$$\overline{A} \frac{\partial \varepsilon_0(x,t)}{\partial x} + \Big(\overline{A}\zeta_0 - B\Big) \frac{\partial^3 w(x,t)}{\partial x^3} = 0 \tag{3.20a}$$

$$B \frac{\partial^2 \varepsilon_0(x,t)}{\partial x^2} + \Big(B\zeta_0 - D\Big) \frac{\partial^4 w(x,t)}{\partial x^4} = \mu \frac{\partial^2 w(x,t)}{\partial t^2} - p(x,t) \tag{3.20b}$$

In the following, the bimodular beam is assumed to be inextensible along the bending neutral plane during the vibrational process. Consequently, the strain on the neutral axis ε_0, as well as its partial derivatives with respect to x, can be neglected in Eqs. (3.20). Finally, the partial differential equation of motion for the bimodular beam flexure subjected to an external dynamic load can be obtained from Eq. (3.20b) after slight rearrangement as follows

$$\Big(D - B\zeta_0\Big) w(x,t)_{,xxxx} + \mu \ddot{w}(x,t) = p(x,t) \tag{3.21}$$

Here, $(\cdot)_{,x}$ denotes the derivative of $(\cdot)$ with respect to the axial coordinate $\partial(\cdot)/\partial x$ and $\dot{(\cdot)}$ indicates time derivative $\partial(\cdot)/\partial t$. Thus, $w(x,t)_{,xxxx} = \partial^4 w(x,t)/\partial x^4$, and $\ddot{w}(x,t) = \partial^2 w(x,t)/\partial t^2$. To find a solution to Eq. (3.21), it is necessary to satisfy the two boundary conditions at each end of the bimodular beam, as well as the initial conditions, which include the initial displacement $w(x,0)$ and initial velocity $\dot{w}(x,0)$ at the time $t = 0$.

Based on the assumption of the inextensible beam along the bending neutral plane, the position of the neutral axis can be determined from Eq. (3.20a). This equation is fulfilled by setting the term in brackets to zero, resulting in

$$\zeta_0 = \frac{B}{\overline{A}} = \frac{\displaystyle\int_A E\,\zeta \,\mathrm{d}A}{\displaystyle\int_A E \,\mathrm{d}A} \tag{3.22}$$

According to this definition, derived from the assumption of the absence of extensional strain along the bending neutral plane, the normal force defined in Eq. (3.12a) becomes zero. Consequently, the actual neutral axis coincides with the bending neutral axis, resulting in the reference point O becoming the elastic centroid. As can be seen, the position of the neutral axis depends not only on the elastic material properties but also on the geometry of the cross-section. Hence, the absolute value of the neutral axis position and the stiffnesses, as defined in Eqs. (3.13), may differ between upward and downward bending in the case of bimodular structure. If such a difference exists, then Eq. (3.21) can be rewritten as

$$D_0 w(x,t)_{,xxxx} + \mu \ddot{w}(x,t) = p(x,t) \tag{3.23}$$

by introducing the effective bending or flexure stiffness D_0, defined as

$$D_0 = \begin{cases} D^{(+)} - B^{(+)}\zeta_0^{(+)} & w(x,t)_{,xx} > 0 \\ D^{(-)} - B^{(-)}\zeta_0^{(-)} & w(x,t)_{,xx} < 0 \end{cases} \tag{3.24}$$

In this context, the superscripts $(\cdot)^{(+)}$ and $(\cdot)^{(-)}$ indicate downward and upward bending, respectively.

3.5 Influence of cross-section and elastic properties on beam stiffnesses

This section analyzes the determination of neutral axis positions, as well as the stiffnesses, for different cross-sections in both upward and downward beam bending configurations. These quantities are expressed by means of the modular ratio defined as

$$\delta = \frac{E_t}{E_c} \tag{3.25}$$

where E_t and E_c denote Young's modulus in tension and compression, respectively. Additionally, it is assumed that Young's modulus in tension E_t is greater than the modulus in compression E_c. All quantities are referred to the Cartesian (η, ζ) coordinate system with the origin at the geometrical centroid S. However, to simplify the determination of the neutral axis position, an auxiliary Cartesian $(\overline{\eta}, \overline{\zeta})$ coordinate system is also introduced, with the origin located at the intersection of the upper edge of the cross-section and the vertical axis of symmetry. Based on Eq. (3.22), the position of neutral axis can be determined within the new auxiliary Cartesian $(\overline{\eta}, \overline{\zeta})$ coordinate system as follows

$$\overline{\zeta}_0 = \frac{\int\limits_A E\,\overline{\zeta}\,\mathrm{d}A}{\int\limits_A E\,\mathrm{d}A} = \frac{\sum\limits_{i=1}^{2} \overline{\zeta}_{S,i}\,E_i A_i}{\sum\limits_{i=1}^{2} E_i A_i} = \frac{\overline{\zeta}_{S,c} E_c A_c + \overline{\zeta}_{S,t} E_t A_t}{E_c A_c + E_t A_t} \tag{3.26}$$

Here, A_c and A_t represent the compression and tension areas, with corresponding $\overline{\zeta}$-coordinates of their centroids denoted as $\overline{\zeta}_{S,c}$ and $\overline{\zeta}_{S,t}$. These quantities can be expressed in terms of the position of the neutral axis $\overline{\zeta}_0$. Subsequently, substituting into Eq. (3.26) leads to an algebraic equation for determining the neutral axis position within the auxiliary $(\overline{\eta}, \overline{\zeta})$ coordinate system. Finally, utilizing the following transformation

$$\zeta_0 = \overline{\zeta}_0 - \overline{\zeta}_S \tag{3.27}$$

the neutral axis position can be expressed within (η, ζ) coordinate system, with the origin located in geometrical centroid S. Here, $\overline{\zeta}_S$ denotes the $\overline{\zeta}$-coordinate of the geometrical centroid of the cross-section with respect to the new Cartesian $(\overline{\eta}, \overline{\zeta})$ coordinate system.

Knowing the position of the neutral axis for both downward and upward bending, the beam stiffnesses, as well as the effective bending stiffness, can be obtained utilizing Eqs. (3.13) and (3.24).

However, an alternative expression for the effective bending stiffness exists, formulated as the product of a factor and the reference unimodular bending stiffness, as follows

$$D_0 = \begin{cases} \lambda_c^{(+)} E_c I_\eta & w(x,t)_{,xx} > 0 \\ \lambda_c^{(-)} E_c I_\eta & w(x,t)_{,xx} < 0 \end{cases} \tag{3.28}$$

where $\lambda_c^{(+)}$ and $\lambda_c^{(-)}$ denote the amplification factors of the unimodular bending stiffness $E_c I_\eta$ in the case of downward and upward bending, respectively. The unimodular bending stiffness is defined by Young's modulus in compression E_c and moment of inertia I_η with respect to the η-axis. Upon comparison of Eqs. (3.24) and (3.28), the definition of both amplification factors is as stated below

$$\lambda_c^{(+)} = \frac{D^{(+)} - B^{(+)}\zeta_0^{(+)}}{E_c I_\eta} \qquad \lambda_c^{(-)} = \frac{D^{(-)} - B^{(-)}\zeta_0^{(-)}}{E_c I_\eta} \tag{3.29}$$

Alternatively, when the unimodular bending stiffness $E_t I_\eta$, which is based on Young's modulus in tension, serves as the reference for expressing the effective bimodular bending stiffness D_0, the corresponding reduction factors of the unimodular stiffness $E_t I_\eta$ for downward and upward bending are defined as

$$\lambda_t^{(+)} = \frac{D^{(+)} - B^{(+)}\zeta_0^{(+)}}{E_t I_\eta} \qquad \lambda_t^{(-)} = \frac{D^{(-)} - B^{(-)}\zeta_0^{(-)}}{E_t I_\eta} \tag{3.30}$$

The amplification and reduction factors' relationship in each bending configuration is governed by the modular ratio, presented as follows

$$\frac{\lambda_c^{(+)}}{\lambda_t^{(+)}} = \frac{\lambda_c^{(-)}}{\lambda_t^{(-)}} = \delta \tag{3.31}$$

Conversely, comparing either the amplification factors or reduction factors between two bending cases results in the effective bending stiffness ratio being expressed as

$$\alpha = \frac{\lambda_c^{(-)}}{\lambda_c^{(+)}} = \frac{\lambda_t^{(-)}}{\lambda_t^{(+)}} = \frac{D^{(-)} - B^{(-)}\zeta_0^{(-)}}{D^{(+)} - B^{(+)}\zeta_0^{(+)}} \tag{3.32}$$

Finally, expressing only in terms of the amplification factor $\lambda_c^{(+)}$, the reference unimodular bending stiffness $E_c I_\eta$, and the effective bending stiffness ratio α, the effective bending stiffness can be rewritten as follows

$$D_0 = \begin{cases} \lambda_c^{(+)} E_c I_\eta & w(x,t)_{,xx} > 0 \\ \alpha \lambda_c^{(+)} E_c I_\eta & w(x,t)_{,xx} < 0 \end{cases} \tag{3.33}$$

In the forthcoming sections, this expression will be utilized to describe the stiffness characteristics of a bimodular beam.

3.5.1 Rectangular cross-section

Fig. 3.3. illustrates a rectangular cross-section, characterized by its dimensions of height h and width b, demonstrating both upward and downward bending configurations. For beams made from unimodular material ($\delta = 1$), the neutral axis coincides with the η-axis and passes through the geometrical centroid S. However, in the concave upward bending and downward bending of the bimodular beam, the neutral axis descends below and ascends above the geometrical centroid, under the assumption that $E_t > E_c$. Similarly, the elastic centroid O follows a similar trend.

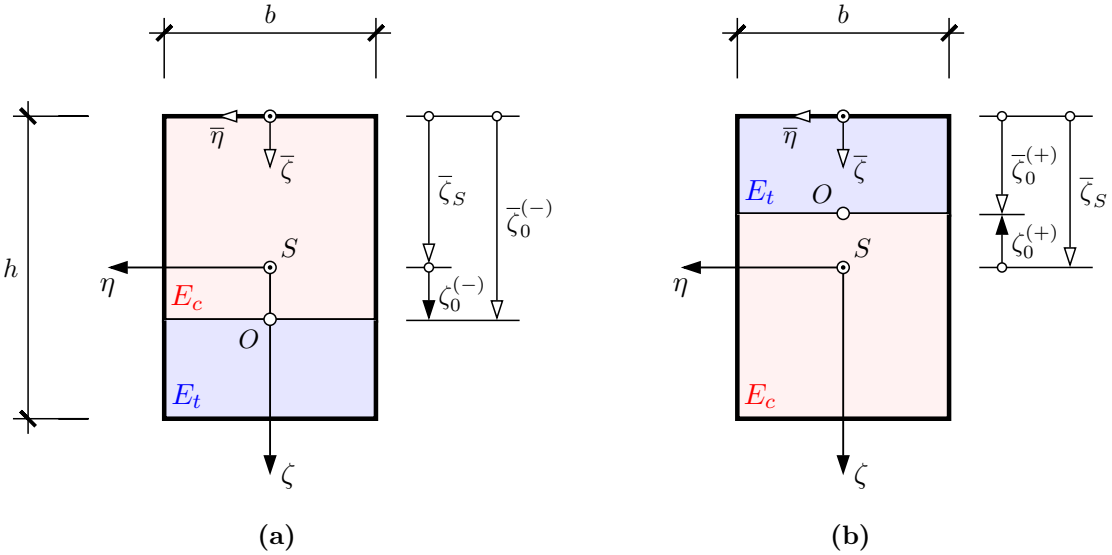

Fig. 3.3: Rectangular cross-section of a bimodular beam under (a) upward (b) downward bending

For the case of concave upward bending, expressing the compression and tension areas, as well as $\bar{\zeta}$-coordinates of their centroids, in terms of $\bar{\zeta}_0^{(-)}$ yields

$$A_c^{(-)} = b\bar{\zeta}_0^{(-)} \qquad A_t = b\Big(h - \bar{\zeta}_0^{(-)}\Big) \qquad \bar{\zeta}_{S,c}^{(-)} = \frac{\bar{\zeta}_0^{(-)}}{2} \qquad \bar{\zeta}_{S,t}^{(-)} = \frac{1}{2}\Big(h + \bar{\zeta}_0^{(-)}\Big) \tag{3.34}$$

The equation for determining the position of neutral axis can be derived by substituting Eqs. (3.34) in Eq. (3.26), resulting in the following quadratic equation in $\bar{\zeta}_0^{(-)}$

$$\Big(\delta - 1\Big)\bar{\zeta}_0^{(-)^2} - 2h\delta\bar{\zeta}_0^{(-)} + h^2\delta = 0 \tag{3.35}$$

which has two solutions

$$\bar{\zeta}_{0,1}^{(-)} = \frac{\delta + \sqrt{\delta}}{\delta - 1}h \qquad \bar{\zeta}_{0,2}^{(-)} = \frac{\delta - \sqrt{\delta}}{\delta - 1}h \tag{3.36}$$

Based on the assumption that Young's modulus in tension E_t is greater than the modulus in compression E_c, and thus the modular ratio $\delta > 1$, the first solution $\bar{\zeta}_{0,1}^{(-)}$ yields a neutral axis position greater than the height h, placing it outside the cross-sectional domain and thus lacking physical significance. In contrast, the second solution $\bar{\zeta}_{0,2}^{(-)}$ provides a value within the cross-sectional domain, which holds physical meaning. After implementing the coordinate

transformation given by Eq. (3.27), the neutral axis position for upward beam bending can be written as follows

$$\zeta_0^{(-)} = \frac{\sqrt{\delta}-1}{2(\sqrt{\delta}+1)}h \tag{3.37}$$

Similarly, in the case of downward bending configuration, the compression and tension areas, including corresponding $\overline{\zeta}$-coordinates of their centroids, can also be expressed by

$$A_c^{(+)} = b\Big(h-\overline{\zeta}_0^{(+)}\Big) \qquad A_t^{(+)} = b\overline{\zeta}_0^{(+)} \qquad \overline{\zeta}_{S,c}^{(+)} = \frac{1}{2}\Big(h+\overline{\zeta}_0^{(+)}\Big) \qquad \overline{\zeta}_{S,t}^{(+)} = \frac{\overline{\zeta}_0^{(+)}}{2} \tag{3.38}$$

Substituting these in Eq. (3.26) leads to a quadratic equation in $\overline{\zeta}_0^{(+)}$ for determining the position of neutral axis, which is given by

$$\Big(\delta-1\Big)\overline{\zeta}_0^{(+)^2} + 2h\overline{\zeta}_0^{(+)} - h^2 = 0 \tag{3.39}$$

This quadratic equation provides two solutions

$$\overline{\zeta}_{0,1}^{(+)} = \frac{-1+\sqrt{\delta}}{\delta-1}h \qquad \overline{\zeta}_{0,2}^{(+)} = \frac{-1-\sqrt{\delta}}{\delta-1}h \tag{3.40}$$

However, only the first solution $\overline{\zeta}_{0,1}^{(+)}$ is relevant in terms of physical interpretation, determining the position of the neutral axis within the cross-sectional domain and is therefore considered. Using the coordinate transformation, as defined in Eq. (3.27), the position of neutral axis for downward bending configuration can be written as

$$\zeta_0^{(+)} = -\frac{\sqrt{\delta}-1}{2(\sqrt{\delta}+1)}h \tag{3.41}$$

Both positions of the neutral axis normalized by height h, for upward and downward bending, are graphically depicted in Fig. (3.4), with the modular ratio ranging from 1 to 30. It is evident that the difference between them lies only in the sign.

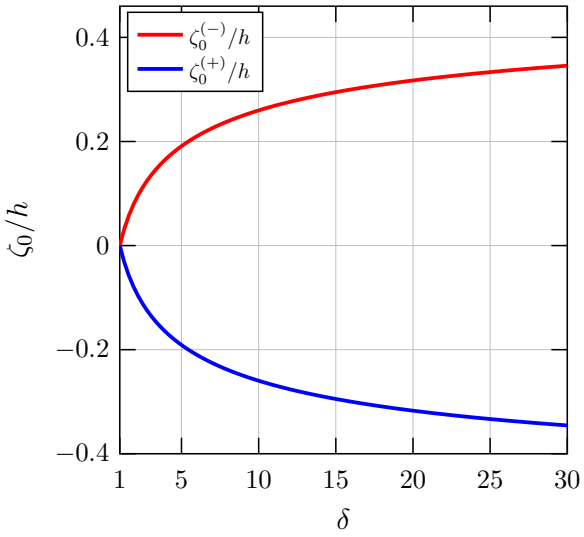

Fig. 3.4: Variation of neutral axis position with δ in the case of upward and downward bending

Having determined the neutral axis positions for both upward and downward bending using Eqs. (3.37) and (3.41), the extensional, bending-extensional coupling and bending stiffness can be obtained utilizing Eqs. (3.13). Since Young's modulus depends on the sign of the axial strain, beam stiffnesses A, B and D are influenced by the neutral plane's position, necessitating the piecewise integration of Eqs. (3.13). In the case of upward bending, where $w(x,t)_{,xx} < 0$, the cross-section is under compression from $-h/2$ to $\zeta_0^{(-)}$, while the bottom portion from $\zeta_0^{(-)}$ to $h/2$ experiences tension, resulting in the following stiffnesses

$$\overline{A}^{(-)} = \int_{-h/2}^{\zeta_0^{(-)}} E_c\, b\, \mathrm{d}\zeta + \int_{\zeta_0^{(-)}}^{h/2} E_t\, b\, \mathrm{d}\zeta = E_c b \left[\frac{h}{2}\Big(\delta+1\Big) - \Big(\delta-1\Big)\zeta_0^{(-)} \right] \tag{3.42a}$$

$$B^{(-)} = \int_{-h/2}^{\zeta_0^{(-)}} E_c\, \zeta b\, \mathrm{d}\zeta + \int_{\zeta_0^{(-)}}^{h/2} E_t\, \zeta b\, \mathrm{d}\zeta = E_c \frac{b}{2} \left[\frac{h^2}{4}\Big(\delta-1\Big) - \Big(\delta-1\Big)\zeta_0^{(-)^2} \right] \tag{3.42b}$$

$$D^{(-)} = \int_{-h/2}^{\zeta_0^{(-)}} E_c\, \zeta^2 b\, \mathrm{d}\zeta + \int_{\zeta_0^{(-)}}^{h/2} E_t\, \zeta^2 b\, \mathrm{d}\zeta = E_c \frac{b}{3} \left[\frac{h^3}{8}\Big(\delta+1\Big) - \Big(\delta-1\Big)\zeta_0^{(-)^3} \right] \tag{3.42c}$$

In similar fashion, the stiffnesses can be obtained for the downward bending, where $w(x,t)_{,xx} > 0$, given by

$$\overline{A}^{(+)} = \int_{-h/2}^{\zeta_0^{(+)}} E_t\, b\, \mathrm{d}\zeta + \int_{\zeta_0^{(+)}}^{h/2} E_c\, b\, \mathrm{d}\zeta = E_c\, b \left[\frac{h}{2}\Big(\delta+1\Big) + \Big(\delta-1\Big)\zeta_0^{(+)} \right] \tag{3.43a}$$

$$B^{(+)} = \int_{-h/2}^{\zeta_0^{(+)}} E_t\, \zeta b\, \mathrm{d}\zeta + \int_{\zeta_0^{(+)}}^{h/2} E_c\, \zeta b\, \mathrm{d}\zeta = E_c\, \frac{b}{2} \left[-\frac{h^2}{4}\Big(\delta-1\Big) + \Big(\delta-1\Big)\zeta_0^{(+)^2} \right] \tag{3.43b}$$

$$D^{(+)} = \int_{-h/2}^{\zeta_0^{(+)}} E_t\, \zeta^2 b\, \mathrm{d}\zeta + \int_{\zeta_0^{(+)}}^{h/2} E_c\, \zeta^2 b\, \mathrm{d}\zeta = E_c\, \frac{b}{3} \left[\frac{h^3}{8}\Big(\delta+1\Big) + \Big(\delta-1\Big)\zeta_0^{(+)^3} \right] \tag{3.43c}$$

By substituting the neutral axis positions $\zeta_0^{(-)}$ and $\zeta_0^{(+)}$, as defined in Eqs. (3.37) and (3.41), into Eqs. (3.42) and (3.43) leads to

$$\overline{A}^{(-)} = \overline{A}^{(+)} = \sqrt{\delta} E_c A \tag{3.44a}$$

$$B^{(-)} = -B^{(+)} = \frac{\delta - \sqrt{\delta}}{2(\sqrt{\delta}+1)} E_c A h \tag{3.44b}$$

$$D^{(-)} = D^{(+)} = \frac{3\sqrt{\delta}(\delta+1) - 2\delta}{(\sqrt{\delta}+1)^2} E_c I_\eta \tag{3.44c}$$

where $A = bh$ represents the cross-sectional area, and $I_\eta = bh^3/12$ denotes the moment of inertia with respect to the η-axis. It is evident that extensional and bending stiffnesses remain consistent regardless of the bending, whether downward or upward. On the other hand, the bending-extensional coupling varies only in sign, in accordance with the position of the neutral axis as indicated by Eqs. (3.37) and (3.41), being positive for upward bending and negative for downward bending. This property of the rectangular cross-section leads to an effective bending stiffness ratio of $\alpha = 1$ according to Eq. (3.32), resulting in no difference in effective bending stiffness between two curvature-dependent bending cases, as defined in Eq. (3.33). Therefore, the effective bending stiffness of the bimodular beam with a rectangular cross-section can be written as

$$D_0 = \lambda_c^{(+)} E_c I_\eta = \lambda_c^{(-)} E_c I_\eta \tag{3.45}$$

where both amplification factors are equal and given by

$$\lambda_c^{(+)} = \lambda_c^{(-)} = \frac{4\delta}{(\sqrt{\delta}+1)^2} \tag{3.46}$$

Fig. 3.5 graphically illustrates these two factors depending on the modular ratio δ.

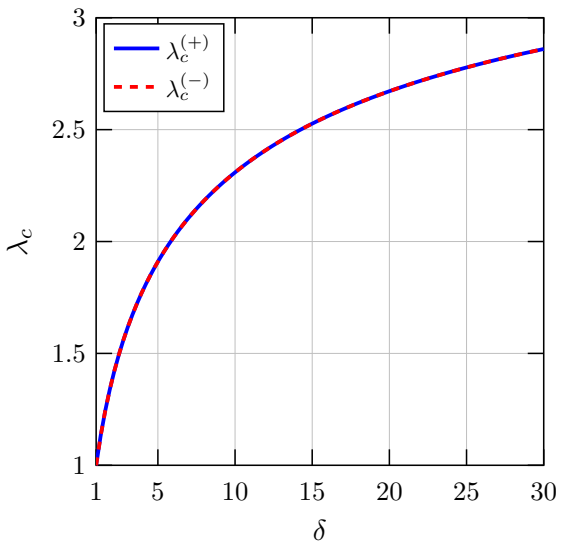

Fig. 3.5: Amplification factors of the corresponding unimodular bending stiffness

When considering a unimodular beam, the neutral axis position for both bending configurations can be determined by substituting $\delta = 1$ into Eqs. (3.37) and (3.41), yielding

$$\zeta_0^{(-)} = \zeta_0^{(+)} = 0 \tag{3.47}$$

Since both values are zero, the neutral axis passes through the geometrical centroid, indicating that the elastic centroid O coincides with the geometrical centroid S. Regarding the beam stiffnesses, as defined in Eq. (3.44), they undergo the following transformation in the unimodular case

$$\overline{A}^{(-)} = \overline{A}^{(+)} = E_c A \qquad B^{(-)} = B^{(+)} = 0 \qquad D^{(-)} = D^{(+)} = E_c I_\eta \tag{3.48}$$

In Fig. 3.5, it can be observed that both amplification factors for the unimodular bending stiffness $E_c I_\eta$ are equal to one. With the neutral axis position and bending-extensional coupling stiffness

being zero, the partial differential equation of motion, as expressed in Eq.(3.21), simplifies to the well-known equation governing flexural vibrations of an unimodular beam

$$E_c I_\eta w(x,t)_{,xxxx} + \mu \ddot{w}(x,t) = p(x,t) \tag{3.49}$$

3.5.2 Isosceles triangular cross-section

Consider a bimodular beam with an isosceles triangular cross-section, as shown in Fig. 3.6. The width can be expressed by the linear function

$$b(\overline{\zeta}) = b\left(1 - \frac{\overline{\zeta}}{h}\right) \tag{3.50}$$

where b represents the top width, and h stands for the height.

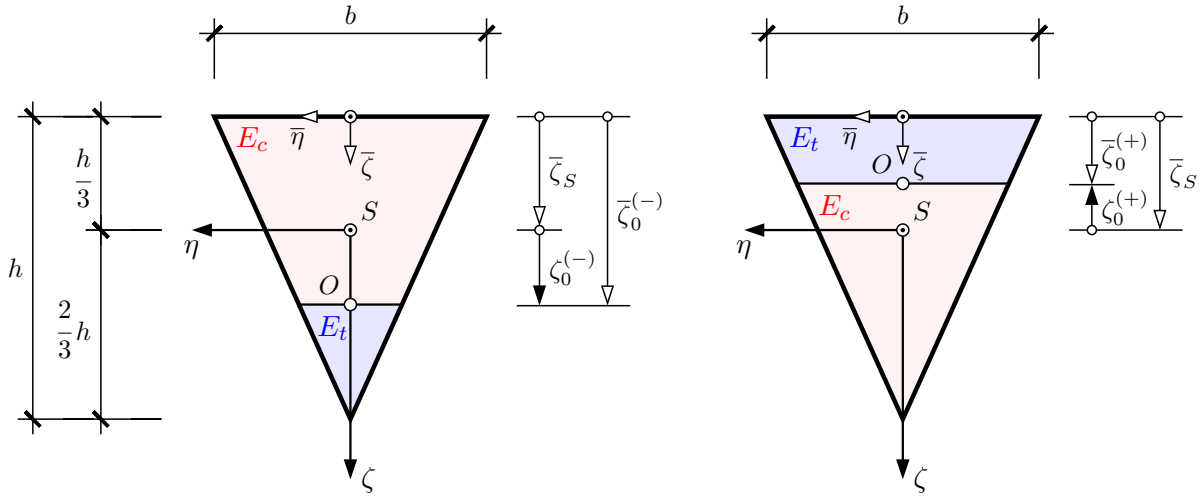

Fig. 3.6: Triangular cross-section of a bimodular beam under (a) upward (b) downward bending

The compression and tension areas can be determined using previously defined width, providing the areas for upward and downward bending configuration, respectively

$$A_c^{(-)} = \frac{b}{2h}\left(2h\overline{\zeta}_0^{(-)} - \overline{\zeta}_0^{(-)2}\right) \qquad A_t^{(-)} = \frac{b}{2h}\left(h^2 - 2h\overline{\zeta}_0^{(-)} + \overline{\zeta}_0^{(-)2}\right) \tag{3.51a}$$

$$A_t^{(+)} = \frac{b}{2h}\left(2h\overline{\zeta}_0^{(+)} - \overline{\zeta}_0^{(+)2}\right) \qquad A_c^{(+)} = \frac{b}{2h}\left(h^2 - 2h\overline{\zeta}_0^{(+)} + \overline{\zeta}_0^{(+)2}\right) \tag{3.51b}$$

Furthermore, the centroids of the compression and tension areas can also be obtained based on the width of the cross-section at the neutral axis position $b(\overline{\zeta}_0)$, giving

$$\overline{\zeta}_{S,c}^{(-)} = \frac{\overline{\zeta}_0^{(-)}\left(3h - 2\overline{\zeta}_0^{(-)}\right)}{3\left(2h - \overline{\zeta}_0^{(-)}\right)} \qquad \overline{\zeta}_{S,t}^{(-)} = \frac{1}{3}\left(h + 2\overline{\zeta}_0^{(-)}\right) \tag{3.52a}$$

$$\overline{\zeta}_{S,t}^{(+)} = \frac{\overline{\zeta}_0^{(+)}\left(3h - 2\overline{\zeta}_0^{(+)}\right)}{3\left(2h - \overline{\zeta}_0^{(+)}\right)} \qquad \overline{\zeta}_{S,c}^{(+)} = \frac{1}{3}\left(h + 2\overline{\zeta}_0^{(+)}\right) \tag{3.52b}$$

For the case of upward bending, where $w(x,t)_{,xx} < 0$, the equation for determining the neutral axis position can be derived by substituting Eqs. (3.51a) and (3.52a) in Eq. (3.26), resulting in the following fourth-degree algebraic equation

$$\left(\delta - 1\right)\overline{\zeta}_0^{(-)^4} - 5h\left(\delta - 1\right)\overline{\zeta}_0^{(-)^3} + h^2\left(9\delta - 6\right)\overline{\zeta}_0^{(-)^2} - 7h^3\delta\overline{\zeta}_0^{(-)} + 2h^4\delta = 0 \tag{3.53}$$

In a similar manner, an algebraic equation of fourth-degree for determining the neutral axis position in the case of downward bending, where $w(x,t)_{,xx} > 0$, is obtained by substituting Eqs. (3.51b) and (3.52b) into Eq. (3.26), giving

$$\left(\delta - 1\right)\overline{\zeta}_0^{(+)^4} - 5h\left(\delta - 1\right)\overline{\zeta}_0^{(+)^3} + h^2\left(6\delta - 9\right)\overline{\zeta}_0^{(+)^2} + 7h^3\overline{\zeta}_0^{(+)} - 2h^4 = 0 \tag{3.54}$$

Solving these two algebraic equations, which determine the position of the neutral axis for two bending configurations, indicates that only the lowest root holds physical relevance, being located within the cross-sectional domain. Following the implementation of the coordinate transformation provided in Eq. (3.27), the neutral axis locations can be expressed within the (η, ζ) coordinate system. Fig. (3.7) illustrates how the ratio of the neutral axis position to the height varies as the modular ratio ranges from 1 to 30.

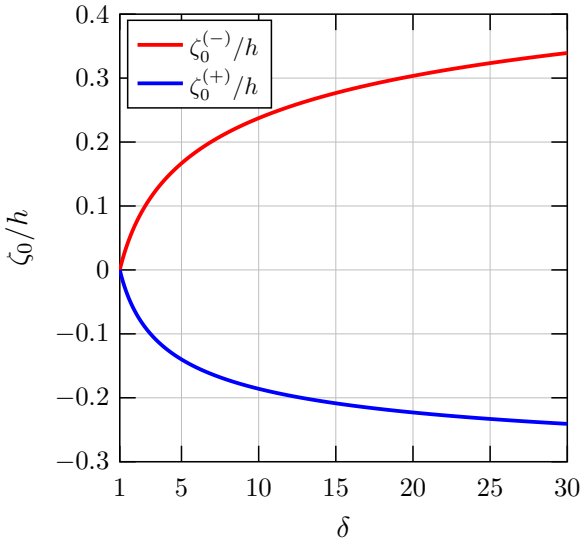

Fig. 3.7: Variation of neutral axis position with δ in the case of upward and downward bending

From Fig. 3.7, it is evident that the distance between the geometric and elastic centroids is larger for upward bending than for downward bending, except for the unimodular case, where the positions are identical.

By expressing the width as a linear function in terms of the ζ-coordinate of (η, ζ) coordinate system

$$b(\zeta) = b\left(\frac{2}{3} - \frac{\zeta}{h}\right) \tag{3.55}$$

the stiffnesses of a beam with an isosceles triangle cross-section can be determined through piecewise integration across the compression and tension regions according to Eqs. (3.13). This leads to the following stiffnesses for upward bending, $w(x,t)_{,xx} < 0$, [30]

$$\overline{A}^{(-)} = E_c b\left[\frac{h}{18}\left(4\delta + 5\right) - \frac{2}{3}\left(\delta - 1\right)\zeta_0^{(-)} + \frac{1}{2h}\left(\delta - 1\right)\zeta_0^{(-)^2}\right] \tag{3.56a}$$

$$B^{(-)} = E_c b\left[\frac{4}{81}h^2\left(\delta - 1\right) - \frac{1}{3}\left(\delta - 1\right)\zeta_0^{(-)^2} + \frac{1}{3h}\left(\delta - 1\right)\zeta_0^{(-)^3}\right] \tag{3.56b}$$

$$D^{(-)} = E_c b\left[\frac{h^3}{972}\left(16\delta + 11\right) - \frac{2}{9}\left(\delta - 1\right)\zeta_0^{(-)^3} + \frac{1}{4h}\left(\delta - 1\right)\zeta_0^{(-)^4}\right] \tag{3.56c}$$

and for the case of downward bending configuration, $w(x,t)_{,xx} > 0$

$$\overline{A}^{(+)} = E_c b\left[\frac{h}{18}\left(5\delta + 4\right) + \frac{2}{3}\left(\delta - 1\right)\zeta_0^{(+)} - \frac{1}{2h}\left(\delta - 1\right)\zeta_0^{(+)^2}\right] \tag{3.57a}$$

$$B^{(+)} = E_c b\left[-\frac{4}{81}h^2\left(\delta - 1\right) + \frac{1}{3}\left(\delta - 1\right)\zeta_0^{(+)^2} - \frac{1}{3h}\left(\delta - 1\right)\zeta_0^{(+)^3}\right] \tag{3.57b}$$

$$D^{(+)} = E_c b\left[\frac{h^3}{972}\left(11\delta + 16\right) + \frac{2}{9}\left(\delta - 1\right)\zeta_0^{(+)^3} - \frac{1}{4h}\left(\delta - 1\right)\zeta_0^{(+)^4}\right] \tag{3.57c}$$

Utilizing the neutral axis position-to-height ratio from Fig. 3.7 and these beam stiffness expressions, the amplification factors for upward and downward bending can be determined, as defined in Eq. (3.29). The variation of these factors with respect to the modular ratio is graphically depicted in Fig. 3.8a, illustrating their growth as the modular ratio increases. The difference between them is described by the effective bending stiffness ratio according to Eq. (3.32), and is also graphically represented in Fig. 3.8b. For example, when $\delta = 2$, the effective bending stiffness for upward bending is approximately 14% higher than for downward bending, while for $\delta = 10$, it increases to 50%.

When considering the unimodular material, where $\delta = 1$, all equations governing the determination of neutral axis positions and beam stiffnesses remain valid and simplify to the well-known case of the unimodular beam, as discussed in the previous subsection by Eq. (3.49).

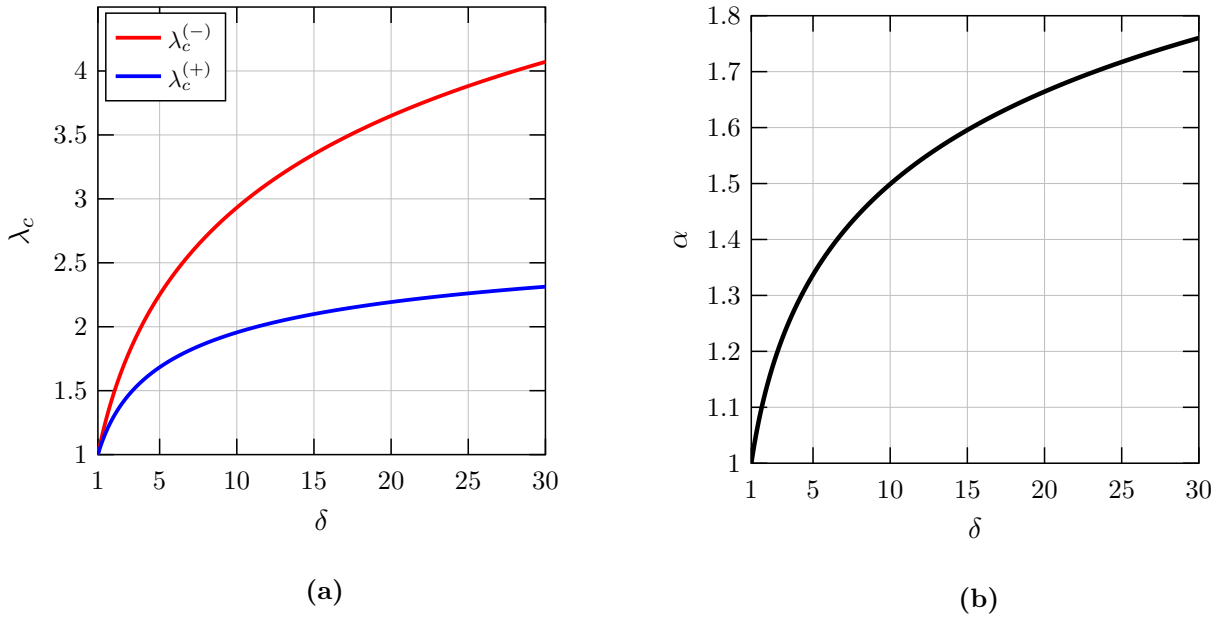

(a) (b)

Fig. 3.8: (a) Variation of amplification factors and (b) effective bending stiffness ratio with δ

3.5.3 Trapezoidal cross-section

A trapezoidal cross-section, defined by dimensions of height h, bottom width a, and top width b, is depicted in Fig. 3.9, illustrating both upward and downward bending configurations.

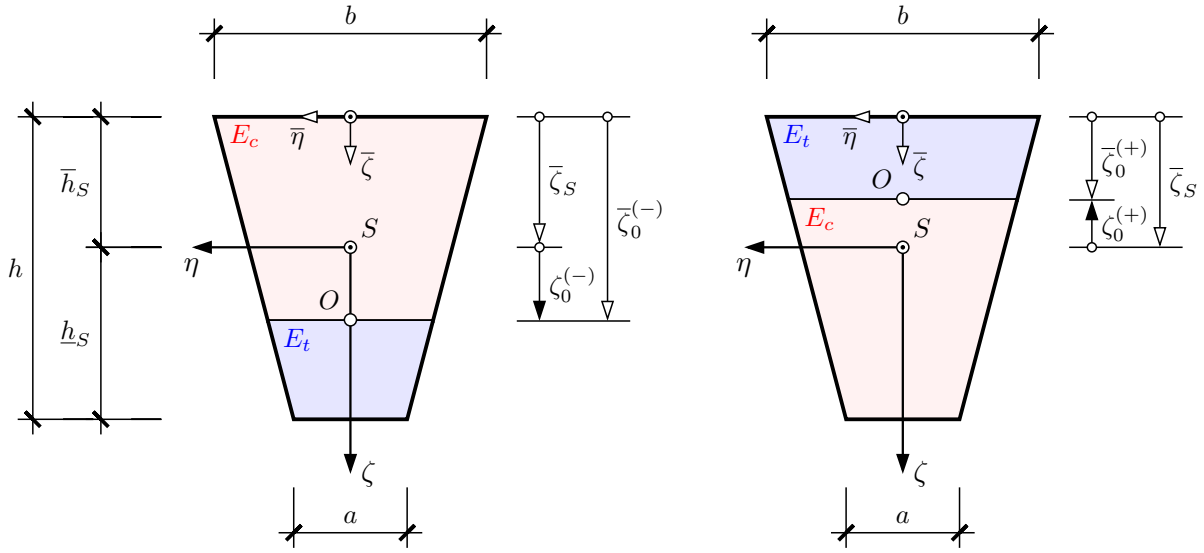

(a) (b)

Fig. 3.9: Trapezoidal cross-section of a bimodular beam under (a) upward (b) downward bending

By representing the width as a linear function of $\overline{\zeta}$, given by

$$b(\overline{\zeta}) = b - \frac{b-a}{h}\overline{\zeta} \tag{3.58}$$

the areas under compression and tension can be expressed for two bending cases as follows

$$A_c^{(-)} = \frac{1}{2h}\left[2bh\overline{\zeta}_0^{(-)} - \Big(b-a\Big)\overline{\zeta}_0^{(-)^2}\right] \qquad A_t^{(-)} = \frac{1}{2h}\left[\Big(b+a\Big)h^2 - 2bh\overline{\zeta}_0^{(-)} + \Big(b-a\Big)\overline{\zeta}_0^{(-)^2}\right] \tag{3.59a}$$

$$A_t^{(+)} = \frac{1}{2h}\left[2bh\overline{\zeta}_0^{(+)} - \Big(b-a\Big)\overline{\zeta}_0^{(+)^2}\right] \qquad A_c^{(+)} = \frac{1}{2h}\left[\Big(b+a\Big)h^2 - 2bh\overline{\zeta}_0^{(+)} + \Big(b-a\Big)\overline{\zeta}_0^{(+)^2}\right] \tag{3.59b}$$

The width of the cross-section at the neutral axis position, as determined by Eq. (3.58), also plays a role in determining the corresponding centroids of the defined areas in Eqs. (3.59), thereby resulting in the following expressions

$$\overline{\zeta}_{S,c}^{(-)} = \frac{3bh\overline{\zeta}_0^{(-)} - 2\Big(b-a\Big)\overline{\zeta}_0^{(-)^2}}{3\Big[2bh - \Big(b-a\Big)\overline{\zeta}_0^{(-)}\Big]} \qquad \overline{\zeta}_{S,t}^{(-)} = \frac{h^2\Big(b+2a\Big) + h\Big(b+2a\Big)\overline{\zeta}_0^{(-)} - 2\Big(b-a\Big)\overline{\zeta}_0^{(-)^2}}{3\Big[\Big(b+a\Big)h - \Big(b-a\Big)\overline{\zeta}_0^{(-)}\Big]} \tag{3.60a}$$

$$\overline{\zeta}_{S,t}^{(+)} = \frac{3bh\overline{\zeta}_0^{(+)} - 2\Big(b-a\Big)\overline{\zeta}_0^{(+)^2}}{3\Big[2bh - \Big(b-a\Big)\overline{\zeta}_0^{(+)}\Big]} \qquad \overline{\zeta}_{S,c}^{(+)} = \frac{h^2\Big(b+2a\Big) + h\Big(b+2a\Big)\overline{\zeta}_0^{(+)} - 2\Big(b-a\Big)\overline{\zeta}_0^{(+)^2}}{3\Big[\Big(b+a\Big)h - \Big(b-a\Big)\overline{\zeta}_0^{(+)}\Big]} \tag{3.60b}$$

Substituting Eqs. (3.59a) and (3.60a) into Eq. (3.26) yields a fifth-degree algebraic equation for determining the neutral axis position under upward bending conditions, where $w(x,t)_{,xx} < 0$, [31]

$$\begin{aligned}\Big(b-a\Big)^3\Big(\delta-1\Big)\overline{\zeta}_0^{(-)^5} - h\Big(6b^3 - 11b^2a + 4ba^2 + a^3\Big)\Big(\delta-1\Big)\overline{\zeta}_0^{(-)^4} + h^2\Big[b^3\Big(14\delta-11\Big) - b^2a\Big(9\delta-6\Big)\\ -ba^2\Big(8\delta-5\Big) + 3a^3\delta\Big]\overline{\zeta}_0^{(-)^3} - h^3\Big[b^3\Big(16\delta-6\Big) + b^2a\Big(9\delta-6\Big) - 12ba^2\delta - a^3\delta\Big]\overline{\zeta}_0^{(-)^2}\\ +h^4\Big(9b^3 + 16b^2a + ba^2 - 2a^3\Big)\delta\overline{\zeta}_0^{(-)} - 2h^5\Big(b^3 + 3b^2a + 2ba^2\Big)\delta = 0\end{aligned} \tag{3.61}$$

In the context of downward bending, where $w(x,t)_{,xx} > 0$, the equation for determinig the location of the neutral axis can be obtained by substituting Eqs. (3.59b) and (3.60b) into Eq. (3.26), leading to

$$\begin{aligned}\Big(b-a\Big)^3\Big(\delta-1\Big)\overline{\zeta}_0^{(+)^5} - h\Big(6b^3 - 11b^2a + 4ba^2 + a^3\Big)\Big(\delta-1\Big)\overline{\zeta}_0^{(+)^4} + h^2\Big[b^3\Big(11\delta-14\Big) - b^2a\Big(6\delta-9\Big)\\ -ba^2\Big(5\delta-8\Big) - 3a^3\Big]\overline{\zeta}_0^{(+)^3} - h^3\Big[b^3\Big(6\delta-16\Big) + b^2a\Big(6\delta-9\Big) + 12ba^2 + a^3\Big]\overline{\zeta}_0^{(+)^2}\\ -h^4\Big(9b^3 + 16b^2a + ba^2 - 2a^3\Big)\overline{\zeta}_0^{(+)} + 2h^5\Big(b^3 + 3b^2a + 2ba^2\Big) = 0\end{aligned} \tag{3.62}$$

Given the dimensions of the trapezoidal cross-section and elastic properties, the position of the neutral axis can be determined by solving Eqs. (3.61) and (3.62) for the unknowns $\overline{\zeta}_0^{(-)}$ and $\overline{\zeta}_0^{(+)}$, respectively. Notably, only the lowest root carries physical significance, as it locates the neutral axis within the cross-section. However, dividing these two equations by h^5 and solving for the ratio $\overline{\zeta}_0/h$ across a range of width ratios a/b from 0 to 1 and by employing the coordinate

transformation defined in Eq. (3.27), one can demonstrate the dependence of the neutral axis position on the modular and width ratios, as depicted in Fig. 3.10. During upward bending, the neutral axis-to-height ratio $\zeta_0^{(-)}/h$ follows the positive direction of the vertical axis, whereas in the case of downward bending, $\zeta_0^{(+)}/h$ pertains to negative regions.

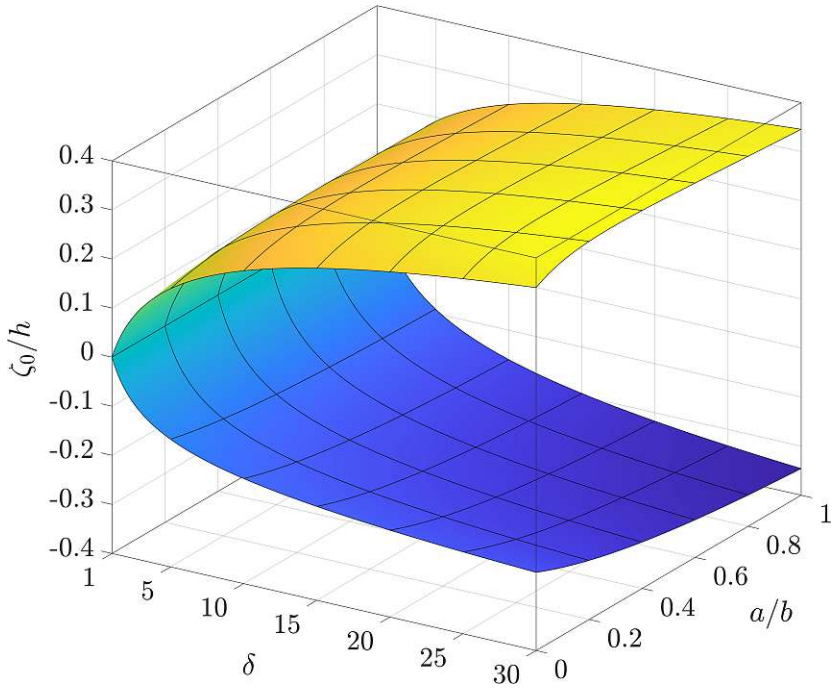

Fig. 3.10: Variation of neutral axis position with δ in the case of upward and downward bending

When the bottom width equals the top width, denoted as $a = b$, indicating a bimodular beam with a rectangular cross-section, Eqs. (3.61) and (3.62) reduce to quadratic equations used to determine the neutral axis position in cases of upward and downward bending, respectively

$$\Big(\delta-1\Big)\overline{\zeta}_0^{(-)^2}-2h\delta\overline{\zeta}_0^{(-)}+h^2\delta=0 \qquad\qquad \Big(\delta-1\Big)\overline{\zeta}_0^{(+)^2}+2h\overline{\zeta}_0^{(+)}-h^2=0 \tag{3.63}$$

It is evident that these two quadratic equations are completely identical to Eqs. (3.35) and (3.39), as derived from the analysis of the rectangular cross-section in Subsection 3.5.1. Accordingly, the positions of the neutral axis are determined by Eqs. (3.37) and (3.41). On the other hand, by specializing Eqs. (3.61) and (3.62) for $a = 0$, fifth-degree polynomials are formed to determine the neutral axis position of a bimodular beam with an isosceles triangular cross-section under condition of upward bending, $w(x,t)_{,xx} < 0$

$$\Big(\delta-1\Big)\overline{\zeta}_0^{(-)^5}-6h\Big(\delta-1\Big)\overline{\zeta}_0^{(-)^4}+h^2\Big(14\delta-11\Big)\overline{\zeta}_0^{(-)^3}-h^3\Big(16\delta-6\Big)\overline{\zeta}_0^{(-)^2}+9h^4\delta\overline{\zeta}_0^{(-)}-2h^5\delta=0 \tag{3.64}$$

and for the downward bending, $w(x,t)_{,xx} > 0$

$$\Big(\delta-1\Big)\overline{\zeta}_0^{(+)^5}-6h\Big(\delta-1\Big)\overline{\zeta}_0^{(+)^4}+h^2\Big(11\delta-14\Big)\overline{\zeta}_0^{(+)^3}-h^3\Big(6\delta-16\Big)\overline{\zeta}_0^{(+)^2}-9h^4\overline{\zeta}_0^{(+)}+2h^5=0 \tag{3.65}$$

Compared to the previous case of specializing equations for $a = b$, resulting in a reduction of polynomial degree from fifth to second, these equations for determining the neutral axis of a

beam with a triangular cross-section now remain fifth-degree polynomials but in a more compact form. Despite being fifth-degree polynomials, they yield exactly the same solution for the neutral axis position as the fourth-degree Eqs. (3.53) and (3.54) derived for the isosceles triangular cross-section in Subsection 3.5.2. It is clear from Fig. 3.10 that the neutral axis position of a beam with a trapezoidal cross-section lies between these two limit cases, namely the rectangular cross-section, where $a = b$, and the isosceles triangular cross-section, where $a = 0$.

The width of an isosceles trapezoidal cross-section can be expressed as a linear function of the ζ-coordinate as follows

$$b(\zeta) = b_0 + b_1\zeta \tag{3.66}$$

where the coefficients b_0 and b_1 are defined as

$$b_0 = \frac{2(b^2 + ba + a^2)}{3(b + a)} \qquad b_1 = -\frac{2b^2 - ba - a^2}{h(2b + a)} \tag{3.67}$$

Based on Eqs. (3.13), the determination of beam stiffnesses necessitates piecewise integration across the compression and tension regions. Specifically, for the analysis of upward bending, the stiffnesses are determined as, [31]

$$\overline{A}^{(-)} = E_c\left[b_0\Big(\underline{h}_S\delta + \overline{h}_S\Big) + \frac{b_1}{2}\Big(\underline{h}_S^2\delta - \overline{h}_S^2\Big) - b_0\Big(\delta - 1\Big)\zeta_0^{(-)} - \frac{b_1}{2}\Big(\delta - 1\Big)\zeta_0^{(-)^2}\right] \tag{3.68a}$$

$$B^{(-)} = E_c\left[\frac{b_0}{2}\Big(\underline{h}_S^2\delta - \overline{h}_S^2\Big) + \frac{b_1}{3}\Big(\underline{h}_S^3\delta + \overline{h}_S^3\Big) - \frac{b_0}{2}\Big(\delta - 1\Big)\zeta_0^{(-)^2} - \frac{b_1}{3}\Big(\delta - 1\Big)\zeta_0^{(-)^3}\right] \tag{3.68b}$$

$$D^{(-)} = E_c\left[\frac{b_0}{3}\Big(\underline{h}_S^3\delta + \overline{h}_S^3\Big) + \frac{b_1}{4}\Big(\underline{h}_S^4\delta - \overline{h}_S^4\Big) - \frac{b_0}{3}\Big(\delta - 1\Big)\zeta_0^{(-)^3} - \frac{b_1}{4}\Big(\delta - 1\Big)\zeta_0^{(-)^4}\right] \tag{3.68c}$$

Furthermore, in the case of downward bending, the determination of the beam stiffnesses results in

$$\overline{A}^{(+)} = E_c\left[b_0\Big(\overline{h}_S\delta + \underline{h}_S\Big) - \frac{b_1}{2}\Big(\overline{h}_S^2\delta - \underline{h}_S^2\Big) + b_0\Big(\delta - 1\Big)\zeta_0^{(+)} + \frac{b_1}{2}\Big(\delta - 1\Big)\zeta_0^{(+)^2}\right] \tag{3.69a}$$

$$B^{(+)} = E_c\left[-\frac{b_0}{2}\Big(\overline{h}_S^2\delta - \underline{h}_S^2\Big) + \frac{b_1}{3}\Big(\overline{h}_S^3\delta + \underline{h}_S^3\Big) + \frac{b_0}{2}\Big(\delta - 1\Big)\zeta_0^{(+)^2} + \frac{b_1}{3}\Big(\delta - 1\Big)\zeta_0^{(+)^3}\right] \tag{3.69b}$$

$$D^{(+)} = E_c\left[\frac{b_0}{3}\Big(\overline{h}_S^3\delta + \underline{h}_S^3\Big) - \frac{b_1}{4}\Big(\overline{h}_S^4\delta - \underline{h}_S^4\Big) + \frac{b_0}{3}\Big(\delta - 1\Big)\zeta_0^{(+)^3} + \frac{b_1}{4}\Big(\delta - 1\Big)\zeta_0^{(+)^4}\right] \tag{3.69c}$$

Here, $\overline{h}_S$ represents the vertical distance from the top width to the geometrical centroid S, while $\underline{h}_S$ denotes the distance from the bottom width to the centroid S, as illustrated in Fig. 3.9.

After establishing the neutral axis position-to-height ratio and the respective beam stiffnesses, as described previously, one can obtain the amplification factors for both upward and downward bending using Eq. (3.29). The influence of the modular and width ratio on the amplification factors is presented in Fig. 3.11. As can be seen, both factors increase with the growing modular ratio δ. However, they do not follow the same trend across the width ratio axis, ranging from

0 to 1. Specifically, while the amplification factor in upward bending decreases, it increases in downward bending, ultimately converging for both to the same value as the limit case $a/b = 1$ is reached, where the trapezoidal cross-section transforms into a rectangular cross-section.

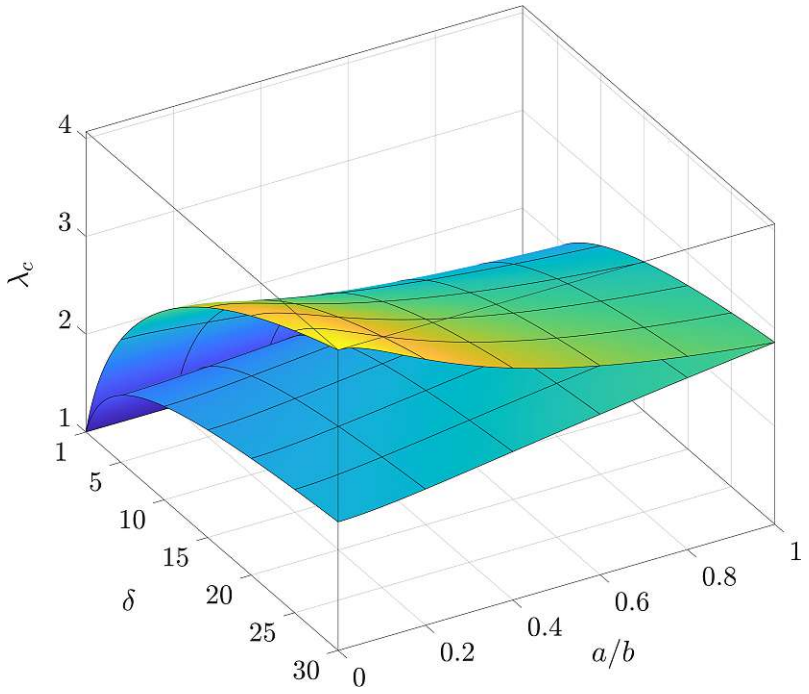

Fig. 3.11: Variation of amplification factors with modular and width ratio

To illustrate how the difference in effective bending stiffness between two curvature-dependent bending cases is affected by various modular and width ratios, the ratio α is determined using Eq. (3.32) and graphically depicted in Fig. 3.12. From the figure, it becomes evident that the effective bending stiffness ratio α generally increases with the modular ratio δ, except for the limit case $a/b = 1$, which signifies a rectangular cross-section. In this case, the ratio α remains constant at one, unaffected by changes in the modular ratio. In terms of the width ratio dependency, the ratio α decreases as the width ratio increases. More precisely, these values lie between two extreme cases, namely, the triangular cross-section with $a/b = 0$ and the rectangular cross-section with $a/b = 1$.

All relations presented in this subsection, describing a beam made from bimodular material with a trapezoidal cross-section, are equally applicable to the unimodular case, where the modular ratio equals 1. This scenario results in the well-known bending stiffness $E_c I_\eta$ and leads to the corresponding equation of motion, as defined in Eq. (3.49).

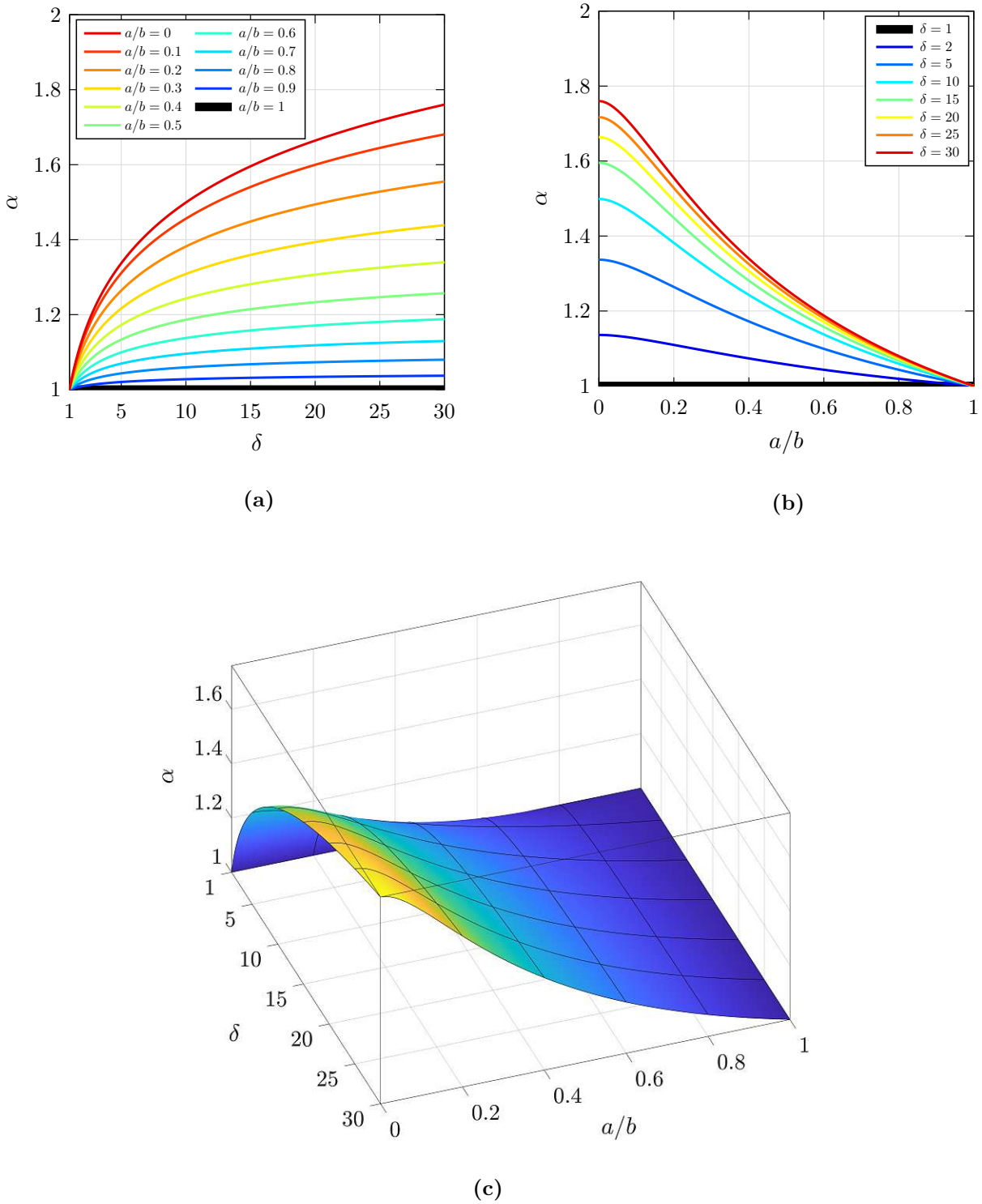

Fig. 3.12: Variation of effective bending stiffness ratio with modular and width ratio

3.5.4 T cross-section

Fig. 3.13 shows a T-shaped cross-section of a beam under upward and downward bending state, respectively.

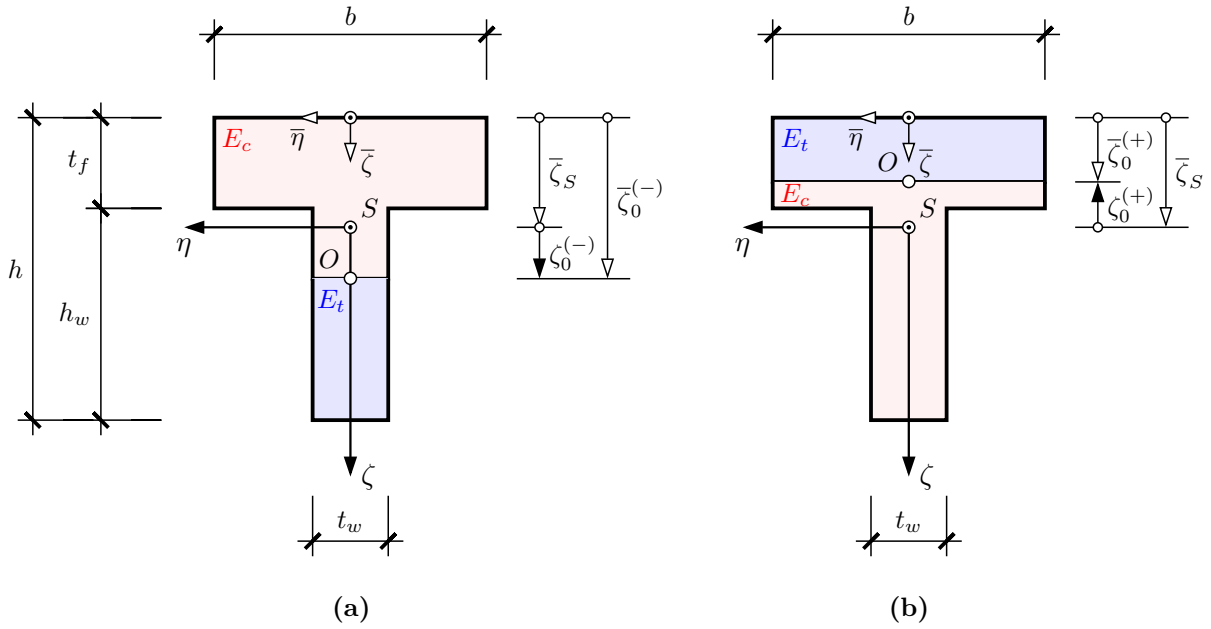

Fig. 3.13: T-shaped cross-section of a bimodular beam under (a) upward (b) downward bending

The calculation of the cross-sectional area can be determined using the formula

$$A = (b - t_w)t_f + t_w h \tag{3.70}$$

In this equation, b signifies the width, h represents the height, t_w denotes the web thickness, and t_f stands for the flange thickness, as depicted in Fig. 3.13. The distance from the top and bottom edges to the centroid of the cross-section S can be obtained from the following equations

$$\overline{h}_S = \overline{\zeta}_S = \frac{1}{2A}\Big[(b - t_w)t_f^2 + t_w h^2\Big] \qquad \underline{h}_S = h - \overline{h}_S \tag{3.71}$$

To characterize the cross-sectional and beam stiffness parameters through variations in the web and flange thickness, Eqs. (3.70) and (3.71) can be rewritten as

$$A = \Big[\gamma(1-\beta) + \beta\Big]bh \qquad \overline{h}_S = \left[\frac{\gamma^2(1-\beta) + \beta}{\gamma(1-\beta) + \beta}\right]\frac{h}{2} \tag{3.72}$$

where

$$\beta = \frac{t_w}{b} \qquad \gamma = \frac{t_f}{h} \tag{3.73}$$

Within each bending configuration, three distinct cases for the neutral axis location are possible, depending on the elastic properties and dimensions of the cross-section, particularly influenced by the ratios specified in Eq. (3.73). The neutral axis can be located either within the flange, within the web, or at the connection of the flange und web. All three cases for both bending states are considered.

3.5.4.1 Neutral axis position for the upward bending configuration, $w(x,t)_{,xx} < 0$

• Case 1: The neutral axis within the flange, $\overline{\zeta}_0^{(-)} < t_f$

When the neutral axis lies within the flange, the compression and tension areas can be determined using the following equation

$$A_c^{(-)} = b\overline{\zeta}_0^{(-)} \qquad A_t^{(-)} = \Big(b - t_w\Big)\Big(t_f - \overline{\zeta}_0^{(-)}\Big) + \Big(h - \overline{\zeta}_0^{(-)}\Big)t_w \tag{3.74}$$

The corresponding centroids can then be calculated as follows

$$\overline{\zeta}_{S,c}^{(-)} = \frac{\overline{\zeta}_0^{(-)}}{2} \qquad \overline{\zeta}_{S,t}^{(-)} = \frac{\Big(b - t_w\Big)\Big(t_f^2 - \overline{\zeta}_0^{(-)^2}\Big) + \Big(h^2 - \overline{\zeta}_0^{(-)^2}\Big)t_w}{2\Big[\Big(b - t_w\Big)\Big(t_f - \overline{\zeta}_0^{(-)}\Big) + \Big(h - \overline{\zeta}_0^{(-)}\Big)t_w\Big]} \tag{3.75}$$

Substituting Eqs. (3.74) and (3.75) into Eq. (3.26) results in a quadratic equation used to determine the neutral axis position within the flange thickness, expressed as

$$\Big(\delta - 1\Big)\overline{\zeta}_0^{(-)^2} - 2\delta\Big[\gamma(1-\beta) + \beta\Big]h\,\zeta_0^{(-)} + \delta\Big[\gamma^2(1-\beta) + \beta\Big]h^2 = 0 \tag{3.76}$$

This quadratic equation yields two solutions, but only one holds physical relevance, locating the neutral axis within the flange. In the context of a unimodular beam with a T cross-section, when $\delta = 1$, Eq. (3.76) simplifies to a linear equation, resulting in the neutral axis passing through the geometric centroid S. The neutral axis position can be written for both material cases as follows

$$\overline{\zeta}_0^{(-)} = \begin{cases} \dfrac{\delta\Big[\gamma(1-\beta) + \beta\Big] - \sqrt{\delta^2\Big[\gamma(1-\beta) + \beta\Big]^2 - \delta(\delta-1)\Big[\gamma^2(1-\beta) + \beta\Big]}}{\delta - 1}h & \delta > 1 \\ \overline{h}_S & \delta = 1 \end{cases} \tag{3.77}$$

• Case 2: The neutral axis within the web, $\overline{\zeta}_0^{(-)} > t_f$

In cases where the neutral axis lies within the web height h_w, the areas under compression and tension can be computed through the utilization of the following equation

$$A_c^{(-)} = \Big(b - t_w\Big)t_f + t_w\overline{\zeta}_0^{(-)} \qquad A_t^{(-)} = \Big(h - \overline{\zeta}_0^{(-)}\Big)t_w \tag{3.78}$$

The determination of centroids for the aforementioned areas is given by

$$\overline{\zeta}_{S,c}^{(-)} = \frac{\Big(b - t_w\Big)t_f^2 + t_w\overline{\zeta}_0^{(-)^2}}{2\Big[\Big(b - t_w\Big)t_f + t_w\overline{\zeta}_0^{(-)}\Big]} \qquad \overline{\zeta}_{S,t}^{(-)} = \frac{1}{2}\Big(\overline{\zeta}_0^{(-)} + h\Big) \tag{3.79}$$

An equation for determining the position of the neutral axis can be obtained by substituting the areas and their centroids into Eq. (3.26), leading to the following quadratic equation

$$\beta\Big(\delta - 1\Big)\overline{\zeta}_0^{(-)^2} - 2\Big[\gamma(1-\beta) + \delta\beta\Big]h\,\zeta_0^{(-)} + \Big[\gamma^2(1-\beta) + \delta\beta\Big]h^2 = 0 \tag{3.80}$$

Following the same approach as in the previous case, the neutral axis position can be determined by solving this quadratic equation and considering only the physically meaningful solution. Ultimately, the position for both bimodular and unimodular cases can be expressed as

$$\overline{\zeta}_0^{(-)} = \begin{cases} \dfrac{\Big[\gamma(1-\beta)+\delta\beta\Big] - \sqrt{\Big[\gamma(1-\beta)+\delta\beta\Big]^2 - \beta(\delta-1)\Big[\gamma^2(1-\beta)+\delta\beta\Big]}}{\beta(\delta-1)} h & \delta > 1 \\ \overline{h}_S & \delta = 1 \end{cases} \tag{3.81}$$

• Case 3: The neutral axis along the bottom flange edge, $\overline{\zeta}_0^{(-)} = t_f$

In order to determine whether the neutral axis position lies within the flange or web for the given material properties and dimensions of the cross-section, the transition value of the ratio γ will be defined. Denoted as $\gamma_{tr}^{(-)}$, this transition value precisely describes the neutral axis position where the flange meets the web, namely, along the bottom flange edge. In this case, where $\overline{\zeta}_0^{(-)} = t_f$, the equation for determining the transition ratio can be obtained by substituting $\overline{\zeta}_0^{(-)} = \gamma_{tr}^{(-)} h$ in Eq. (3.77) or (3.81). Both equations result in the same quadratic equation in $\gamma_{tr}^{(-)}$, given by

$$\Big(\delta\beta - 1\Big){\gamma_{tr}^{(-)}}^2 - 2\delta\beta\gamma_{tr}^{(-)} + \delta\beta = 0 \tag{3.82}$$

Although this quadratic equation provides two solutions, only one holds physical significance, precisely positioning the neutral axis at the intersection of the flange and web. This solution is expressed as

$$\gamma_{tr}^{(-)} = \frac{\delta\beta - \sqrt{\delta\beta}}{\delta\beta - 1} \tag{3.83}$$

Given the elastic properties and dimensions of the T cross-section, the actual ratio γ and the transition ratio $\gamma_{tr}^{(-)}$ can be calculated according to Eqs. (3.73) and (3.83), respectively. If $\gamma \geq \gamma_{tr}^{(-)}$, the neutral axis is located within the flange thickness and is determined by Eq. (3.77). Conversely, if $\gamma \leq \gamma_{tr}^{(-)}$, the neutral axis lies within the web and can be computed using Eq. (3.81). Subsequently, by utilizing the coordinate transformation defined in Eq. (3.27), the neutral axis position can be expressed with respect to (η, ζ) coordinate system, with its origin located at geometric centroid S.

The variation of the neutral axis concerning β and γ for the upward bending state with the modular ratio $\delta = 2$ is depicted in Fig. 3.14. While Fig. 3.14a illustrates the dependency across γ for different values of β, incrementing from 0 to 1 with a step of 0.1, Fig. 3.14b demonstrates how the neutral axis varies with β, where γ steps from 0 to 1. In this context, the red line delineates the neutral axis position along the bottom flange edge, serving as a transitional case between locating the neutral axis in the flange and the web. Both extreme cases, where the ratios are 0 and 1, correspond to the transformation of the T cross-section into a rectangular cross-section. However, if both ratios are simultaneously equal to zero, a cross-section does not exist.

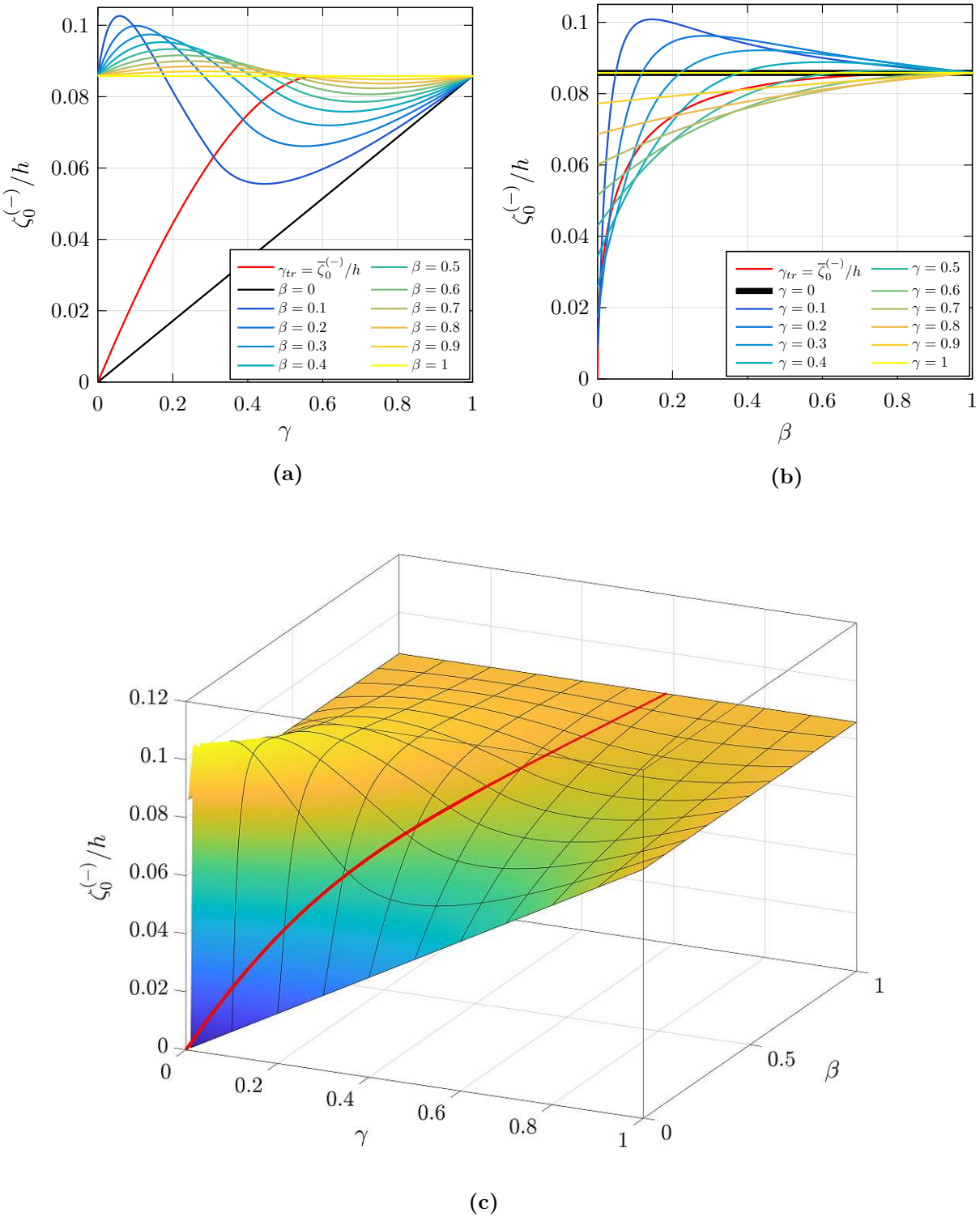

Fig. 3.14: Variation of neutral axis position with β and γ in the case of upward bending and modular ratio $\delta = 2$

3.5.4.2 Neutral axis position for the downward bending configuration, $w(x,t)_{,xx} > 0$

• Case 1: The neutral axis within the flange, $\overline{\zeta}_0^{(+)} < t_f$

In a manner similar to that of the upward bending case, the neutral axis position for the downward bending state can also be determined. The process begins with the consideration of the following compression and tension areas

$$A_t^{(+)} = b\overline{\zeta}_0^{(+)} \qquad A_c^{(+)} = \Big(b - t_w\Big)\Big(t_f - \overline{\zeta}_0^{(+)}\Big) + \Big(h - \overline{\zeta}_0^{(+)}\Big)t_w \tag{3.84}$$

and their corresponding centroids

$$\overline{\zeta}_{S,t}^{(+)} = \frac{\overline{\zeta}_0^{(+)}}{2} \qquad \overline{\zeta}_{S,c}^{(+)} = \frac{\Big(b - t_w\Big)\Big(t_f^2 - \overline{\zeta}_0^{(+)^2}\Big) + \Big(h^2 - \overline{\zeta}_0^{(+)^2}\Big)t_w}{2\Big[\Big(b - t_w\Big)\Big(t_f - \overline{\zeta}_0^{(+)}\Big) + \Big(h - \overline{\zeta}_0^{(+)}\Big)t_w\Big]} \tag{3.85}$$

Subsequently, an equation for determining the position of the neutral axis can be derived by substituting Eqs. (3.84) and (3.85) into Eq. (3.26), resulting in the following quadratic equation

$$\Big(\delta - 1\Big)\overline{\zeta}_0^{(+)^2} + 2\Big[\gamma(1-\beta) + \beta\Big]h\,\overline{\zeta}_0^{(+)} - \Big[\gamma^2(1-\beta) + \beta\Big]h^2 = 0 \tag{3.86}$$

While this quadratic equation yields two solutions, only one possesses the physical meaning when considering a beam made from bimodular material. Conversely, Eq. (3.86) reduces to a linear equation in the unimodular case, where $\delta = 1$. Both solutions can be written compactly as

$$\overline{\zeta}_0^{(+)} = \begin{cases} \dfrac{-\Big[\gamma(1-\beta) + \beta\Big] + \sqrt{\Big[\gamma(1-\beta) + \beta\Big]^2 + (\delta - 1)\Big[\gamma^2(1-\beta) + \beta\Big]}}{\delta - 1}h & \delta > 1 \\ \overline{h}_S & \delta = 1 \end{cases} \tag{3.87}$$

• Case 2: The neutral axis within the web, $\overline{\zeta}_0^{(+)} > t_f$

In instances where the neutral axis is located within the web, the computation of compression and tension areas can be carried out using the following equations

$$A_t^{(+)} = \Big(b - t_w\Big)t_f + t_w\overline{\zeta}_0^{(+)} \qquad A_c^{(+)} = \Big(h - \overline{\zeta}_0^{(+)}\Big)t_w \tag{3.88}$$

The centroids for these areas are determined by

$$\overline{\zeta}_{S,c}^{(+)} = \frac{\Big(b - t_w\Big)t_f^2 + t_w\overline{\zeta}_0^{(-)^2}}{2\Big[\Big(b - t_w\Big)t_f + t_w\overline{\zeta}_0^{(-)}\Big]} \qquad \overline{\zeta}_{S,t}^{(+)} = \frac{1}{2}\Big(\overline{\zeta}_0^{(-)} + h\Big) \tag{3.89}$$

Upon substitution of Eqs. (3.88) and (3.89) into Eq. (3.26), a quadratic equation is obtained for determining the neutral axis position within the flange, given by

$$\beta\Big(\delta - 1\Big)\overline{\zeta}_0^{(+)^2} + 2\Big[\delta\gamma(1-\beta) + \beta\Big]h\,\zeta_0^{(+)} - \Big[\delta\gamma^2(1-\beta) + \beta\Big]h^2 = 0 \tag{3.90}$$

This quadratic equation provides a physically meaningful solution for determining the neutral axis position within the web for both bimodular and unimodular beams subjected to downward bending, as expressed by

$$\overline{\zeta}_0^{(+)} = \begin{cases} \dfrac{-\Big[\delta\gamma(1-\beta)+\beta\Big] + \sqrt{\Big[\delta\gamma(1-\beta)+\beta\Big]^2 + \beta(\delta-1)\Big[\delta\gamma^2(1-\beta)+\beta\Big]}}{\beta(\delta-1)}h & \delta > 1 \\ \overline{h}_S & \delta = 1 \end{cases} \tag{3.91}$$

• Case 3: The neutral axis along the bottom flange edge, $\overline{\zeta}_0^{(+)} = t_f$

As in the previous bending case, the transition ratio $\gamma_{tr}^{(+)}$, which positions the neutral axis at the junction of the flange and web, can be determined by substituting $\overline{\zeta}_0^{(+)} = \gamma_{tr}^{(+)}h$ into either Eq. (3.87) or (3.91). Each equation leads to an identical quadratic equation in terms of $\gamma_{tr}^{(+)}$, given by

$$\Big(\delta-\beta\Big)\gamma_{tr}^{(+)^2} + 2\beta\gamma_{tr}^{(+)} - \beta = 0 \tag{3.92}$$

The equation, which defines the transition ratio in the case of downward bending and is obtained from solving this quadratic equation while considering physically meaningful solutions, is as follows

$$\gamma_{tr}^{(+)} = \frac{\beta - \sqrt{\delta\beta}}{\beta - \delta} \tag{3.93}$$

In cases where $\gamma \geq \gamma_{tr}^{(+)}$, the neutral axis is within the flange thickness and is calculated using Eq.(3.87). On the contrary, if $\gamma \leq \gamma_{tr}^{(+)}$, the neutral axis falls within the web and can be determined using Eq.(3.91).

Similar to the preceding bending state, Fig. 3.15 illustrates the graphical representation of the neutral axis' dependency on the ratios β and γ, as well as on the modular ratio δ, in the case of downward bending.

Given the dimensions of the T cross-section and bimodular ratio, the position of the neutral axis can be determined as described previously. It allows the neutral axis to be located either in the flange, the web, or at their junction, representing a transitional case. The beam stiffnesses can be obtained by integrating piecewise over the compression and tension regions. However, depending on the neutral axis position, two cases arise for determining the beam stiffnesses in each bending state, namely, when the neutral axis lies within the flange or the web. In the first case, where the neutral axis lies within the flange, the integration process for the area under the neutral axis should be performed piecewise due to the step in width discontinuity. Conversely, when the neutral axis is located within the web, the integration process for the area above the neutral axis should also be carried out piecewise. After integration implementation according to Eq. (3.13), the beam stiffnesses are obtained for both neutral axis positions, considering both bending configurations, as presented in the following two subsections.

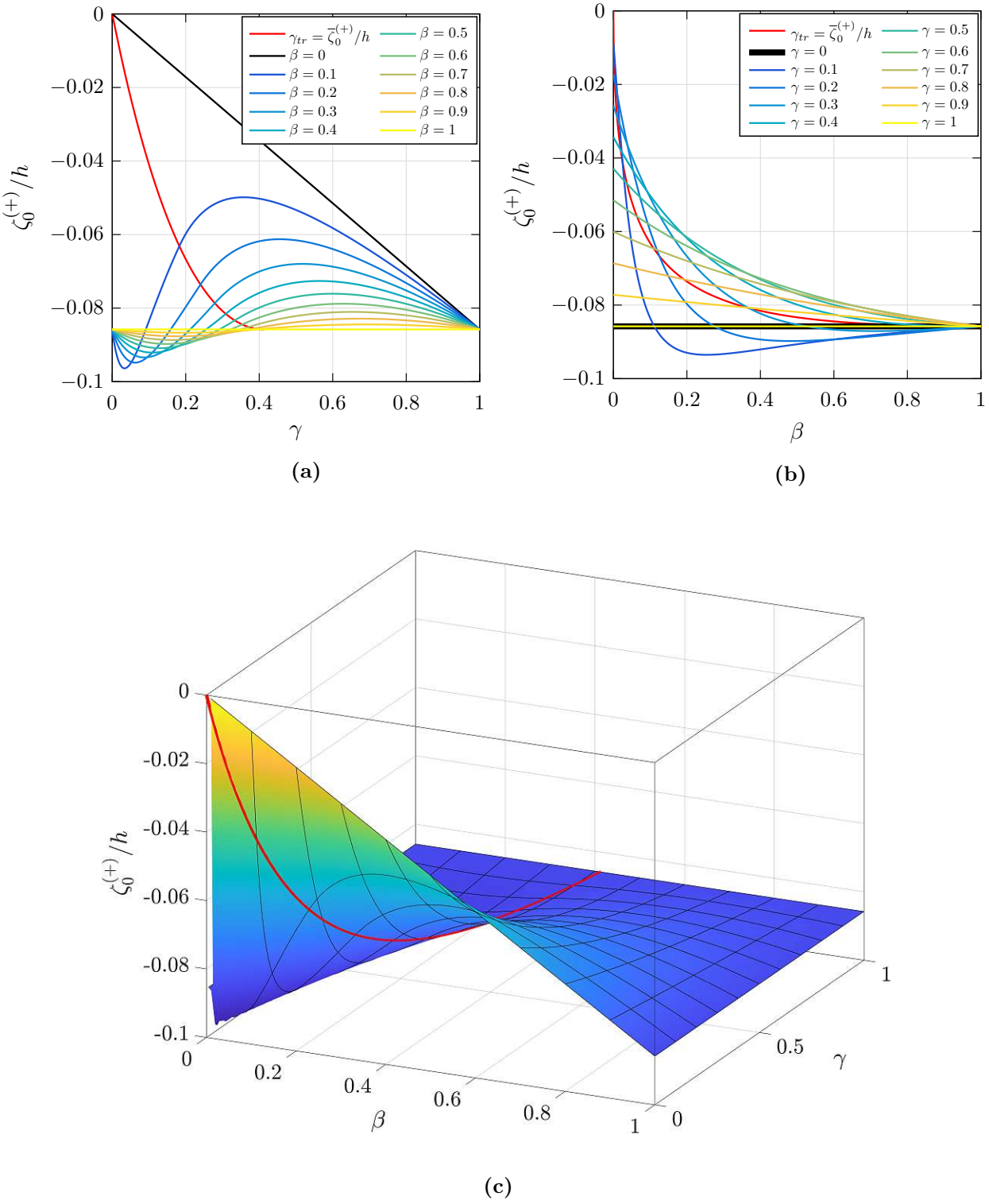

Fig. 3.15: Variation of neutral axis position with β and γ in the case of downward bending and modular ratio $\delta = 2$

3.5.4.3 Stiffnesses for the upward bending configuration, $w_{,xx}(x,t) < 0$

- Case 1: The neutral axis within the flange, $\gamma \geq \gamma_{tr}^{(-)}$

$$\overline{A}^{(-)} = E_c\, b \left[-\Big(\delta - 1\Big)\zeta_0^{(-)} + \delta\Big[\gamma\Big(1-\beta\Big) + \beta\Big]h - \Big(\delta - 1\Big)\overline{h}_S \right] \tag{3.94a}$$

$$B^{(-)} = E_c \frac{b}{2} \left[-\Big(\delta - 1\Big)\zeta_0^{(-)^2} + \delta\Big(1-\beta\Big)\Big(\gamma h - \overline{h}_S\Big)^2 - \overline{h}_S^2 + \delta\beta\underline{h}_S^2 \right] \tag{3.94b}$$

$$D^{(-)} = E_c \frac{b}{3} \left[-\Big(\delta - 1\Big)\zeta_0^{(-)^3} + \delta\Big(1-\beta\Big)\Big(\gamma h - \overline{h}_S\Big)^3 + \overline{h}_S^3 + \delta\beta\underline{h}_S^3 \right] \tag{3.94c}$$

- Case 2: The neutral axis within the web, $\gamma \leq \gamma_{tr}^{(-)}$

$$\overline{A}^{(-)} = E_c\, b \left[-\beta\Big(\delta - 1\Big)\zeta_0^{(-)} + \gamma\Big(1-\beta\Big)h + \beta\overline{h}_S + \delta\beta\underline{h}_S \right] \tag{3.95a}$$

$$B^{(-)} = E_c \frac{b}{2} \left[-\beta\Big(\delta - 1\Big)\zeta_0^{(-)^2} + \Big(1-\beta\Big)\Big(\gamma h - \overline{h}_S\Big)^2 - \overline{h}_S^2 + \delta\beta\underline{h}_S^2 \right] \tag{3.95b}$$

$$D^{(-)} = E_c \frac{b}{3} \left[-\beta\Big(\delta - 1\Big)\zeta_0^{(-)^3} + \Big(1-\beta\Big)\Big(\gamma h - \overline{h}_S\Big)^3 + \overline{h}_S^3 + \delta\beta\underline{h}_S^3 \right] \tag{3.95c}$$

3.5.4.4 Stiffnesses for the downward bending configuration, $w_{,xx}(x,t) > 0$

- Case 1: The neutral axis within the flange, $\gamma \geq \gamma_{tr}^{(+)}$

$$\overline{A}^{(+)} = E_c\, b \left[\Big(\delta - 1\Big)\zeta_0^{(+)} + \Big[\gamma\Big(1-\beta\Big) + \beta\Big]h + \Big(\delta - 1\Big)\overline{h}_S \right] \tag{3.96a}$$

$$B^{(+)} = E_c \frac{b}{2} \left[\Big(\delta - 1\Big)\zeta_0^{(+)^2} + \Big(1-\beta\Big)\Big(\gamma h - \overline{h}_S\Big)^2 - \delta\overline{h}_S^2 + \beta\underline{h}_S^2 \right] \tag{3.96b}$$

$$D^{(+)} = E_c \frac{b}{3} \left[\Big(\delta - 1\Big)\zeta_0^{(+)^3} + \Big(1-\beta\Big)\Big(\gamma h - \overline{h}_S\Big)^3 + \delta\overline{h}_S^3 + \beta\underline{h}_S^3 \right] \tag{3.96c}$$

- Case 2: The neutral axis within the web, $\gamma \leq \gamma_{tr}^{(+)}$

$$\overline{A}^{(+)} = E_c\, b \left[\beta\Big(\delta - 1\Big)\zeta_0^{(+)} + \delta\gamma\Big(1-\beta\Big)h + \delta\beta\overline{h}_S + \beta\underline{h}_S \right] \tag{3.97a}$$

$$B^{(+)} = E_c \frac{b}{2} \left[\beta\Big(\delta - 1\Big)\zeta_0^{(+)^2} + \delta\Big(1-\beta\Big)\Big(\gamma h - \overline{h}_S\Big)^2 - \delta\overline{h}_S^2 + \beta\underline{h}_S^2 \right] \tag{3.97b}$$

$$D^{(+)} = E_c \frac{b}{3} \left[\beta\Big(\delta - 1\Big)\zeta_0^{(+)^3} + \delta\Big(1-\beta\Big)\Big(\gamma h - \overline{h}_S\Big)^3 + \delta\overline{h}_S^3 + \beta\underline{h}_S^3 \right] \tag{3.97c}$$

3.5.4.5 Amplification factors and effective bending stiffness ratio

After determining the beam stiffnesses for both bending states, the comparison between the reference unimodular stiffness $E_c I_\eta$ and the effective bimodular bending stiffness is facilitated through the calculation of the amplification factor, as defined in Eq. (3.29). The dependency of this factor on the ratios δ, β, and γ is graphically illustrated in Appendix A.2, Figs. A.1 and A.2.

Based on the amplification factors, the corresponding differences in the effective bending stiffness between two bending cases, described by their ratio α, are also graphically represented in Figs. 3.16 and 3.17. As a result, the effective bending stiffness ratios α remain constant and equal to one for rectangular cross-sections, which represent limit cases of the ratios β and α. Furthermore, with regards to T cross-sections, the stiffness ratios α increase along the modular ratio axis, indicating higher values in the region characterized by lower values of β and γ. Fig. 3.18 demonstrates how the effective bending stiffness ratio α is influenced by different combinations of the geometric ratios β and γ, while maintaining a constant modular ratio of $\delta = 2$.

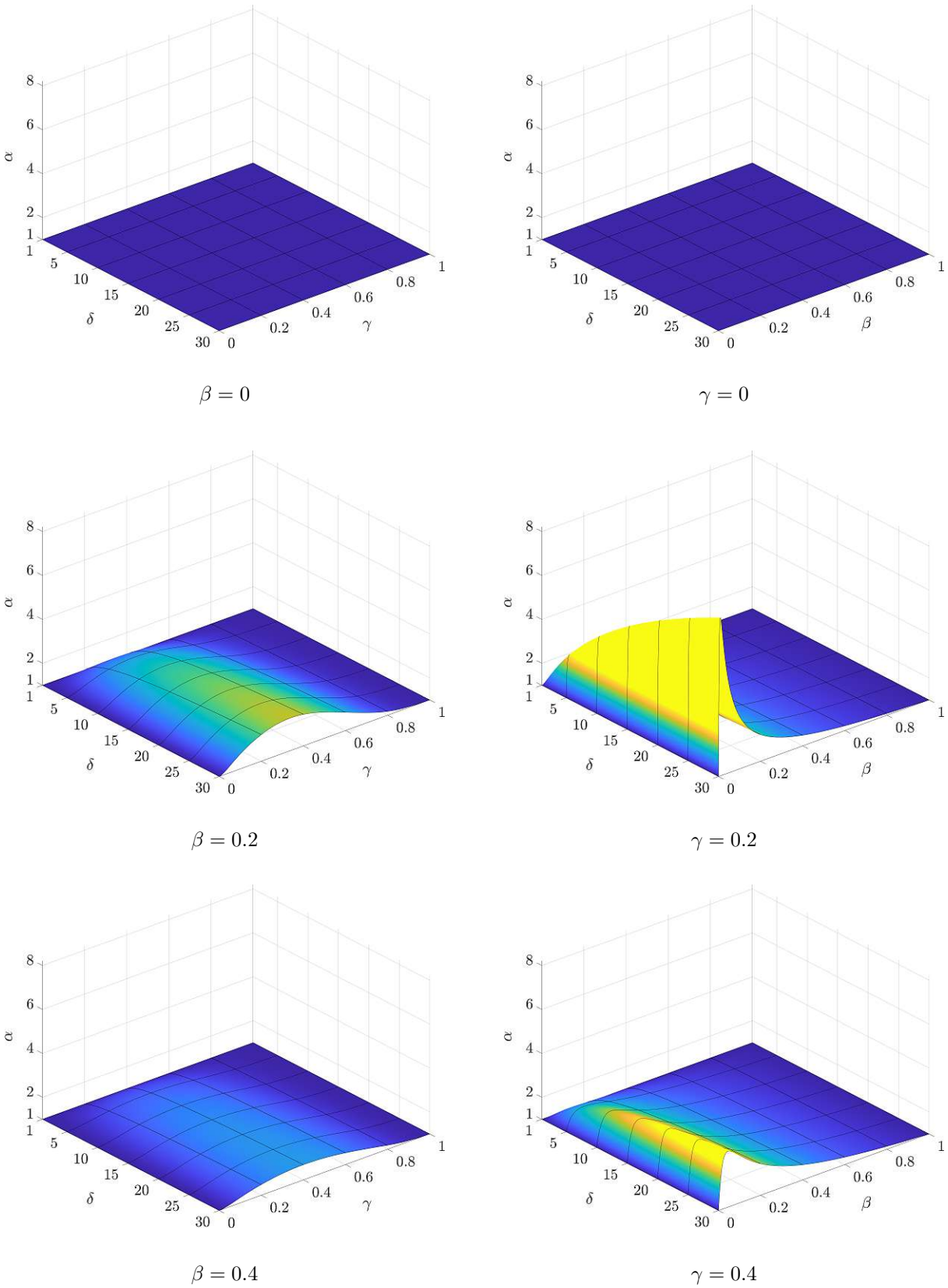

Fig. 3.16: Variation of effective bending stiffness ratio α with δ, β, and γ

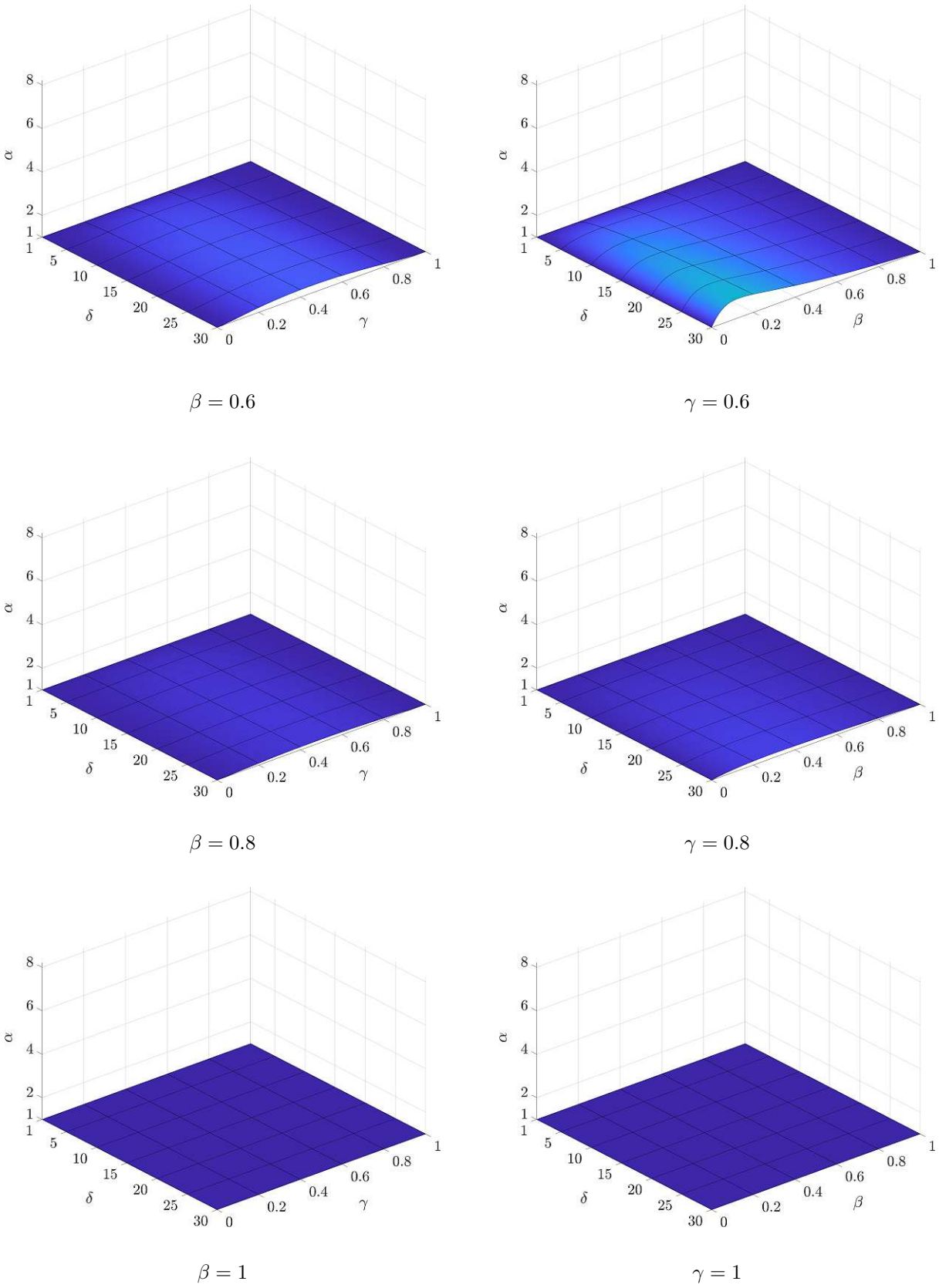

Fig. 3.17: Variation of effective bending stiffness ratio α with δ, β, and γ

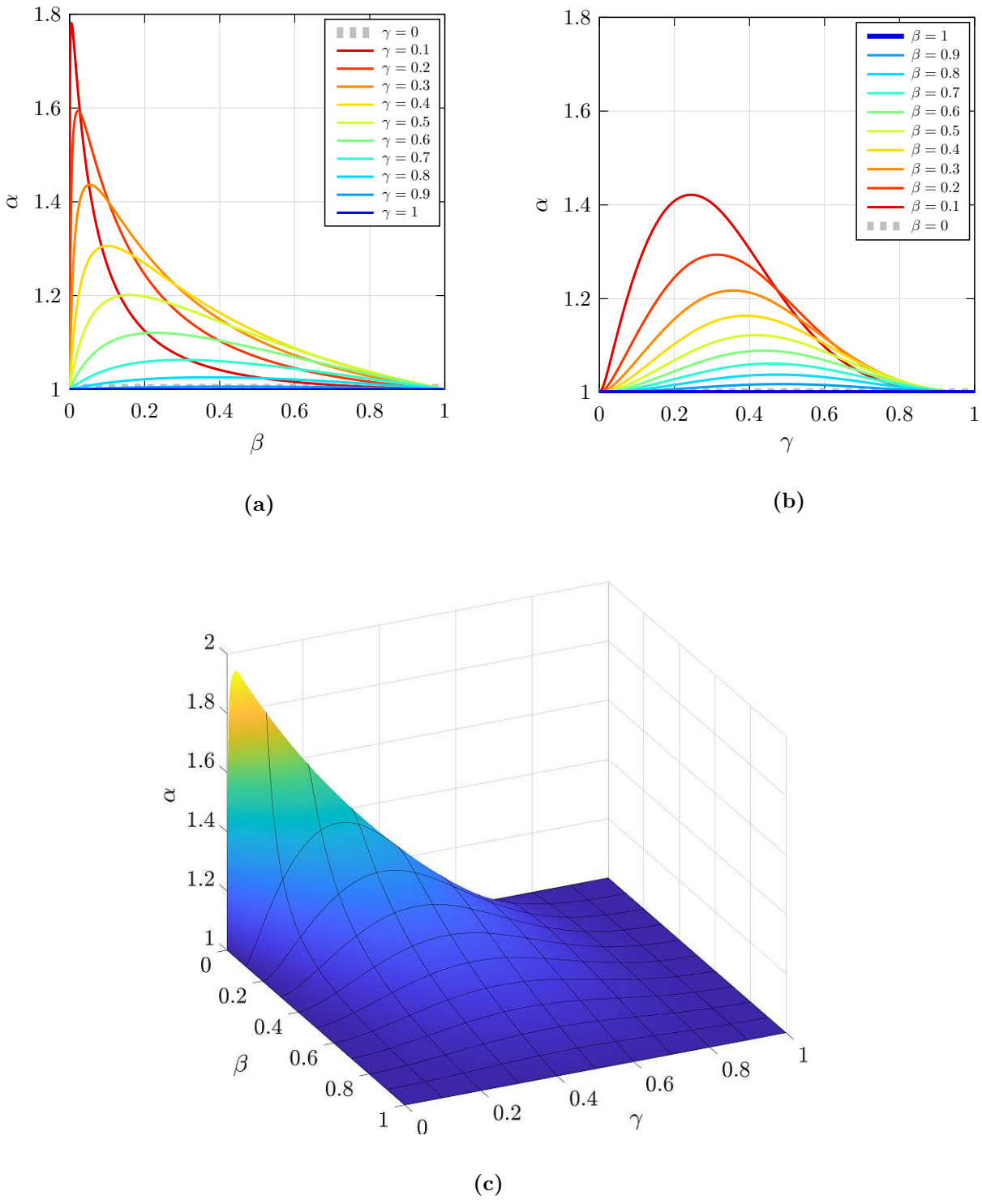

Fig. 3.18: Variation of effective bending stiffness ratio with β and γ for modular ratio $\delta = 2$

Chapter 4

Dynamic analysis of bimodular beams using isogeometric finite elements

This chapter introduces the fundamental concepts of the isogeometric discretization method and their application in the linear and nonlinear dynamic analysis of bimodular beams. The definition of B-splines and their properties is provided in Section 1. Following this, Section 2 presents the system matrices and the discretized governing equations for both linear and nonlinear cases. The harmonic balance method is also introduced as a powerful tool for analyzing the nonlinear steady-state frequency response due to periodic excitation.

4.1 B-splines

4.1.1 B-spline basis function

The starting point for the B-spline basis functions is a knot vector, defined as a non-decreasing set of coordinates in the parameter space

$$\Xi = [\xi_1, \xi_2, \ldots, \xi_{n+p+1}] \tag{4.1}$$

where $\xi_i \in \mathbb{R}$ is the i^{th} knot, i is the knot index, n is the number of basis functions and p is the polynomial degree. Knot vectors can be categorized as uniform or non-uniform and open or periodic. In a uniform knot vector, the knots are equally spaced in the parameter space. If this condition is not satisfied, a knot vector is called non-uniform. Moreover, a knot vector is said to be open if its first and last values appear $p+1$ times; otherwise, it is periodic.

Given a knot vector in one dimension, the B-spline basis functions are defined by the *Cox-de Bor* recursion formula starting with zeroth degree basis function $p = 0$ (piecewise constants)

$$N_{i,0}(\xi) = \begin{cases} 1 & \text{if } \xi_i \leq \xi < \xi_{i+1} \\ 0 & \text{otherwise} \end{cases} \tag{4.2}$$

and for polynomial degree $p \geq 1$

$$N_{i,p}(\xi) = \frac{\xi - \xi_i}{\xi_{i+p} - \xi_i} N_{i,p-1}(\xi) + \frac{\xi_{i+p+1} - \xi}{\xi_{i+p+1} - \xi_{i+1}} N_{i+1,p-1}(\xi) \tag{4.3}$$

The piecewise constant B-spline basis functions are defined on the entire parametric domain of a knot vector Ξ, taking a value of one only within the interval $[\xi_i, \xi_{i+1}]$, so-called i^{th} knot span, and are elsewhere zero. Higher-degree B-spline basis functions are linear combinations of two B-spline lower degree basis functions with corresponding coefficients. Eq. (4.3) can lead to a quotient of form 0/0, which is assumed to be zero. The *Cox-de Boor* recursion formula can be represented by a truncated triangle table, as shown in Fig. 4.1.

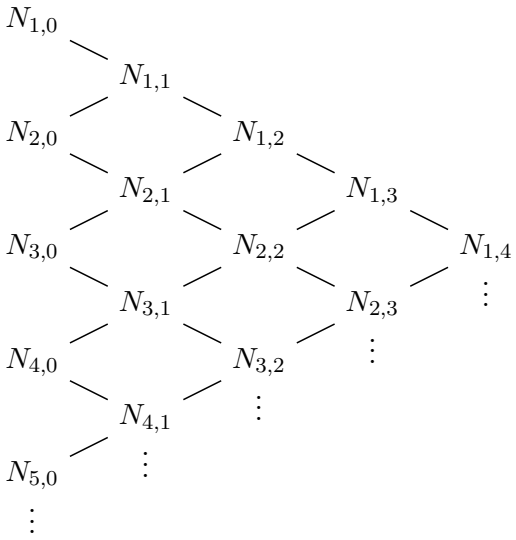

Fig. 4.1: Visualization of the *Cox-de Boor* algorithm for B-spline evaluation, [41]

Fig. 4.2 illustrates the B-spline basis functions for a uniform knot vector by applying the *Cox-de Boor* recursion expression shown in Eqs. (4.2) and (4.3), [16, 21, 32].

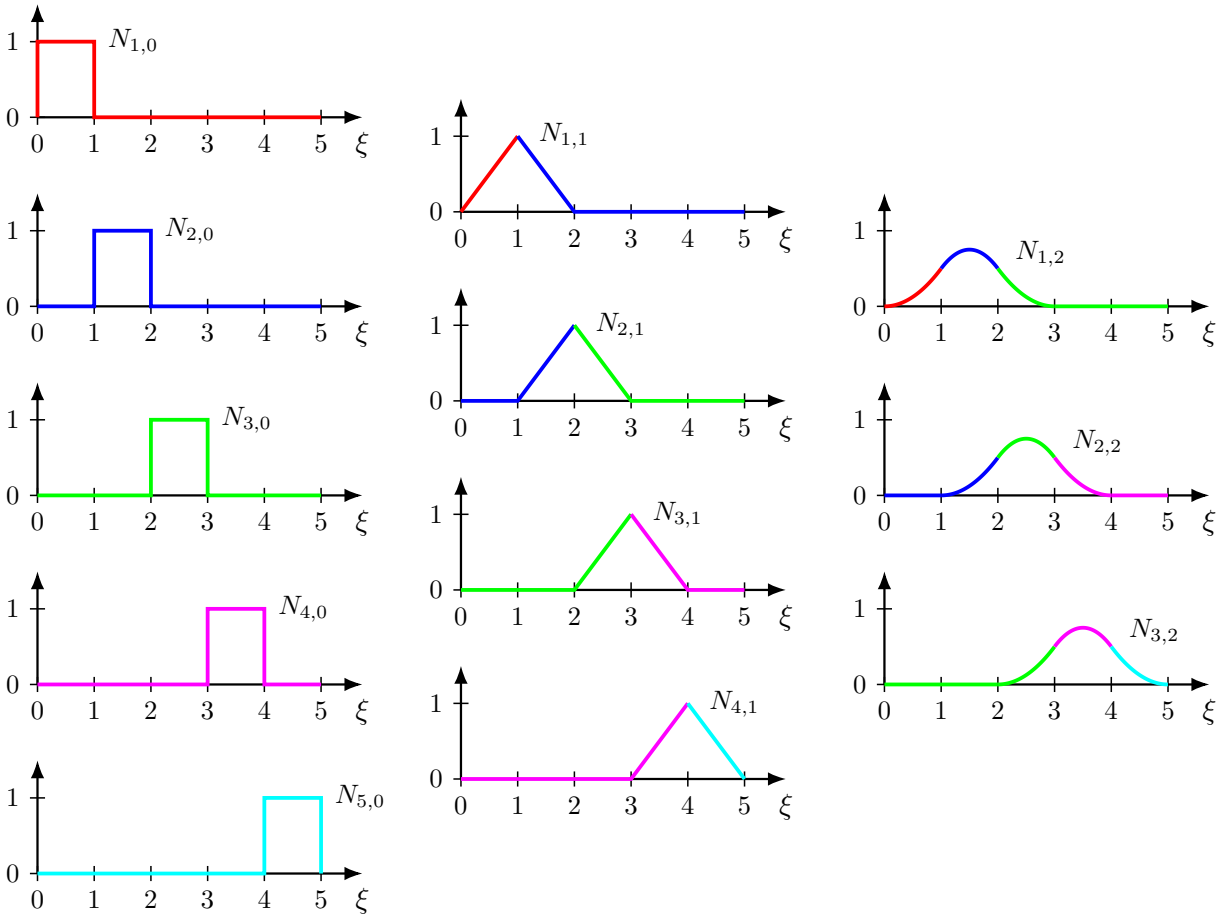

Fig. 4.2: Basis functions of degree 0,1,2 for uniform knot vector $\Xi = [0, 1, 2, 3, 4, 5]$

An example of constant, linear, quadratic and cubic B-spline basis functions generated from the open, uniform knot vector $\Xi = [0, 0, 0, 0, 1, 2, 3, 4, 5, 5, 5, 5]$ and the open, non-uniform knot vector $\Xi = [0, 0, 0, 0, 2, 2.8, 3.4, 4.5, 5, 5, 5, 5]$ is presented in Fig. 4.3.

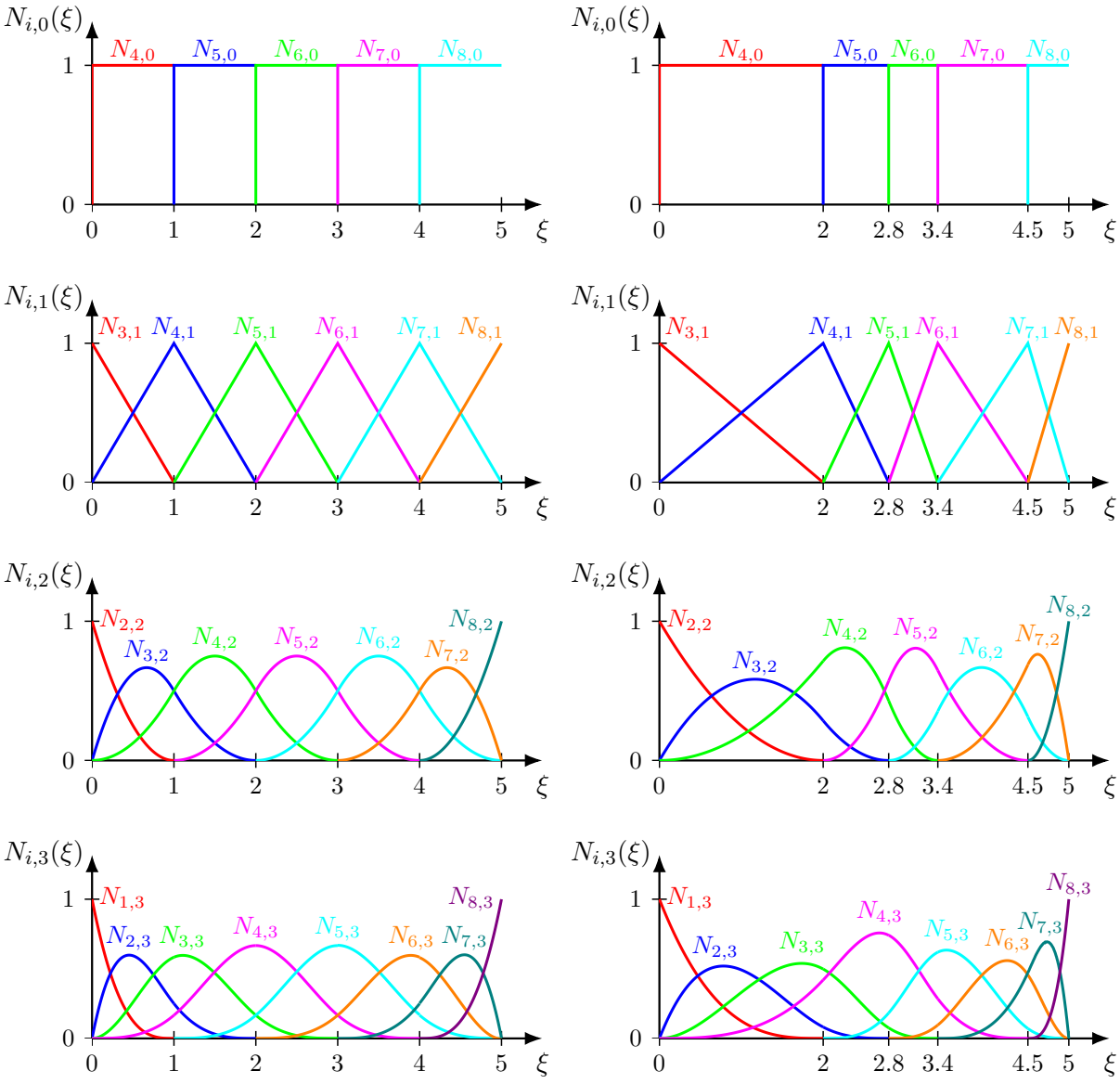

Fig. 4.3: Constant, linear, quadratic and cubic B-spline basis functions for
(a) open, uniform knot vector $\Xi = [0, 0, 0, 0, 1, 2, 3, 4, 5, 5, 5, 5]$
(b) open, non-uniform knot vector $\Xi = [0, 0, 0, 0, 2, 2.8, 3.4, 4.5, 5, 5, 5, 5]$

The B-spline basis functions of degree p are continuously differentiable inside knot spans and $p-1$ differentiable (C^{p-1} -continuous) across the knots. If a knot value ξ_i is repeated s times, then the functions are C^{p-s} -continuous across the knot ξ_i. When the multiplicity s of the knot is equal to the polynomial degree p, the basis function is interpolatory at that knot. In the case of the multiplicity $s = p+1$, the basis is discontinuous and the patch boundary is formed, [16, 21, 32]. Fig. 4.4 shows an example of a set of cubic B-spline functions generated from the open, non-uniform knot vector $\Xi = [0,0,0,0,1,2,2,3,3,3,4,5,5,5,5]$.

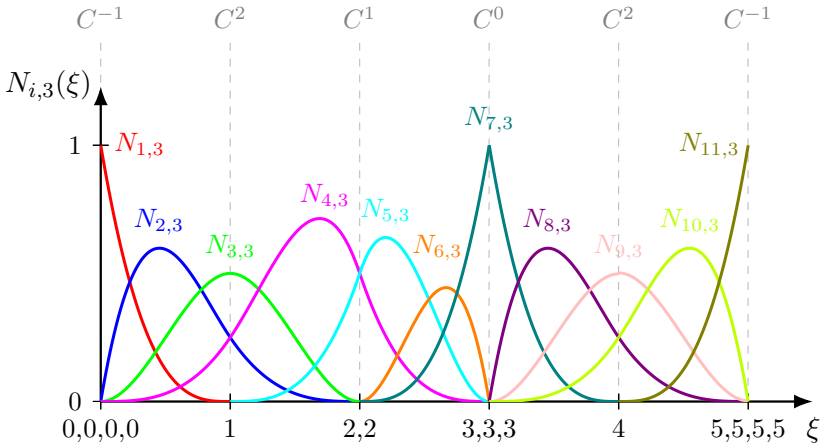

Fig. 4.4: Cubic basis functions for open, non-uniform knot vector $\Xi = [0,0,0,0,1,2,2,3,3,3,4,5,5,5,5]$

As can be seen, the basis functions are interpolatory at the ends of the parameter space interval (i.e., the patch) and at the p times repeated knot $\xi = 3$, where the continuity is only C^0. While only C^1 continuity is achieved at the second internal element boundary, $\xi = 2$, having multiplicity of $s = 2$, the basis functions are C^2 -continuous across the knots $\xi = 1$ and $\xi = 4$.

Some important properties of the B-spline basis functions are

- partition of unity: $\sum_{i=1}^{n} N_{i,p}(\xi) = 1, \quad \forall \xi \in \Xi$
- non-negativity: $N_{i,p}(\xi) \geq 0, \quad \forall \xi \in \Xi$
- continuity: Within knot spans, the basis functions $N_{i,p}(\xi)$ are continuous differentiable, while across knots, they show $p-s$ differentiability, where s denotes the multiplicity of the knot ξ_i.
- compact support: The support of each basis function $N_{i,p}(\xi)$ is compact and contained in the interval $[\xi_i, \xi_{i+p+1}]$.

The first derivative of a B-spline basis function with respect to the parametric coordinates is defined by the following recursive formula

$$N'_{i,p}(\xi) = \frac{p}{\xi_{i+p} - \xi_i} N_{i,p-1}(\xi) - \frac{p}{\xi_{i+p+1} - \xi_{i+1}} N_{i+1,p-1}(\xi) \tag{4.4}$$

By differentiating both sides of the Eq. (4.4), higher derivatives can be generalized as follows

$$N^{(k)}_{i,p}(\xi) = \frac{p}{\xi_{i+p} - \xi_i} N^{(k-1)}_{i,p-1}(\xi) - \frac{p}{\xi_{i+p+1} - \xi_{i+1}} N^{(k-1)}_{i+1,p-1}(\xi) \tag{4.5}$$

where (k) denotes the k^{th} derivative.

The first and second derivatives of the cubic B-spline basis functions shown in Fig. 4.4 are presented in Fig. 4.5 below.

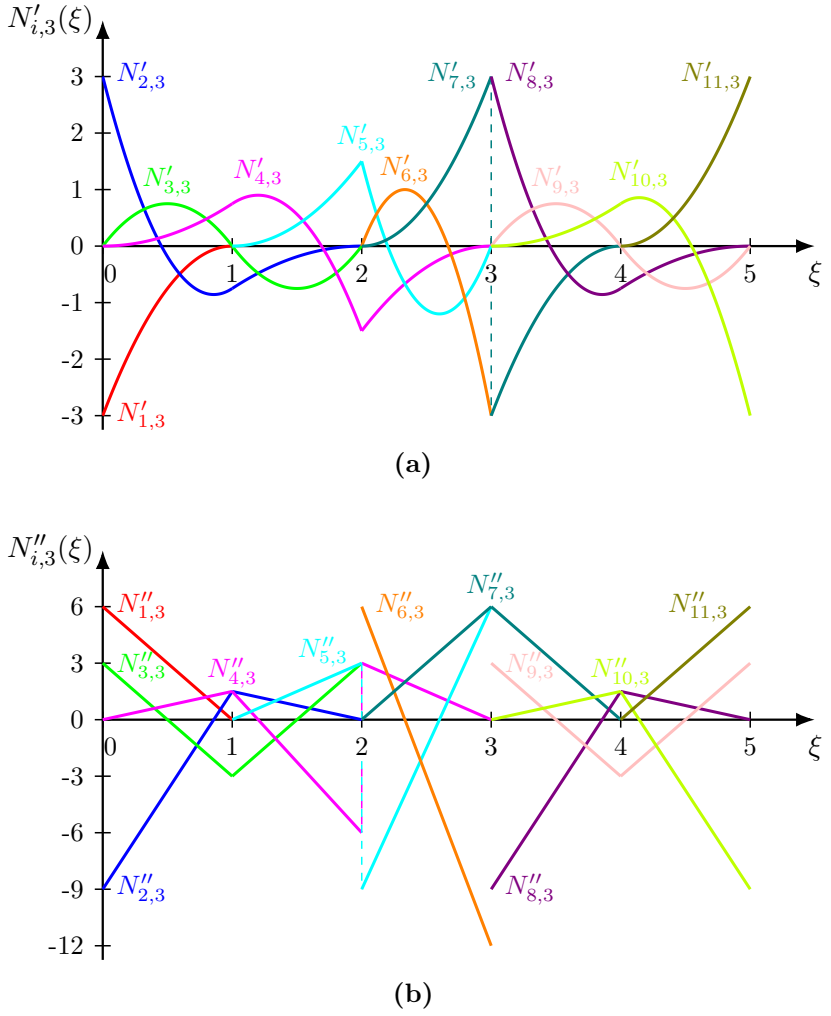

Fig. 4.5: (a) First (b) Second derivatives corresponding to the B-spline basis functions in Fig. 4.4

4.1.2 B-spline curves

A piecewise-polynomial B-spline curve of the degree p can be obtained by taking a linear combination of n B-spline basis functions and control points $\mathbf{P}_i$, which are points in the physical space

$$\mathbf{C}(\xi) = \sum_{i=1}^{n} N_{i,p}(\xi)\,\mathbf{P}_i \tag{4.6}$$

4.1.3 Refinement

4.1.3.1 Knot insertion (h-refinement)

Inserting an additional new knot $\bar{\xi} \in [\xi_k, \xi_{k+1}]$ into an initial knot vector $\Xi = [\xi_1, \xi_2, \ldots, \xi_{n+p+1}]$ gives an extended knot vector $\bar{\Xi} = [\xi_1, \xi_2, \ldots, \xi_k, \bar{\xi}, \xi_{k+1}, \ldots, \xi_{n+p+1}]$, such that $\Xi \subset \bar{\Xi}$. Applying the Eqs. (4.2) and (4.3) to the new knot vector $\bar{\Xi}$ provides the new $n+1$ basis functions. The new set of $n+1$ control points, $[\bar{\mathbf{P}}_1, \bar{\mathbf{P}}_2, \ldots, \bar{\mathbf{P}}_{n+1}]$, can be expressed as a linear combination of the initial control points, $[\mathbf{P}_1, \mathbf{P}_2, \ldots, \mathbf{P}_n]$, by

$$\bar{\mathbf{P}}_i = \alpha_i \mathbf{P}_i + (1 - \alpha_i)\mathbf{P}_{i-1} \tag{4.7}$$

where

$$\alpha_i = \begin{cases} 1 & 1 \leq i \leq k-p \\ \dfrac{\bar{\xi} - \xi_i}{\xi_{i+p} - \xi_i} & k-p+1 \leq i \leq k \\ 0 & k+1 \leq i \leq n+p+2 \end{cases} \tag{4.8}$$

During knot insertion, both the geometry and parametrization remain completely unchanged, namely the newly formed curve is identical to the initially unrefined curve. However, the basis functions and control points are changed and each increased by one. This refinement process splits an initial element into two new elements, just as in classical finite element analysis with h-refinement strategy. Compared to the classical h-refinement process in finite element analysis, the continuity of the basis functions across the newly inserted knot is C^{p-1}. In order to reproduce the h-refinement exactly according to finite element analysis, the multiplicity of the new knot $\bar{\xi}$ needs to be inserted p times, so that the basis functions achieve the C^0 continuity at the new boundary.

4.1.3.2 Degree elevation (p-refinement)

Degree elevation involves increasing the polynomial degree p of basis functions without changing the curve geometrically or parametrically. This strategy of degree elevation starts by subdividing the curve into multiple Bézier segments by inserting existing internal knot values until their multiplicity is equal to the polynomial degree. Next, polynomial degree elevation can be performed on each of these Bézier segments. Finally, unnecessary knots introduced during subdivision can be removed, and the knot segments are connected, forming a higher-degree B-spline curve. This refinement process requires calculating $n+1$ new control point positions, $[\bar{\mathbf{P}}_1, \bar{\mathbf{P}}_2, \ldots, \bar{\mathbf{P}}_{n+1}]$, using the initial control point values, $[\mathbf{P}_1, \mathbf{P}_2, \ldots, \mathbf{P}_n]$, and coefficients α_i according to the following equation

$$\bar{\mathbf{P}}_i = (1 - \alpha_i)\mathbf{P}_i + \alpha_i \mathbf{P}_{i-1} \tag{4.9}$$

where

$$\alpha_i = \frac{i-1}{p+1} \qquad i = 1, \ldots, p+2 \tag{4.10}$$

In particular, elevating the degree from p to $p+t$ in a single step is also attainable. Expressing multiple recursive applications of Eq. (4.9) and rearranging coefficients gives

$$\mathbf{P}_i^t = \sum_{j=\max(1,i-t)}^{\min(p+1,i)} \frac{\binom{p}{j-1}\binom{t}{i-j}}{\binom{p+t}{i-1}} \mathbf{P}_j \qquad i = 1, \ldots, p+t+1 \tag{4.11}$$

The process of degree elevation shares significant commonalities with the classical p-refinement in finite element analysis, involving the utilization of higher-degree polynomials at the element level. The fundamental difference lies in the fact that p-refinement starts with C^0 continuity of the basis everywhere, whereas in isogeometric analysis, continuity at inner knots is preserved and not reduced to C^0. For a special case of a mesh, in which all basis functions maintain C^0 continuity across knots, degree elevation coincides completely with the classical p-refinement.

4.1.3.3 k-refinement

An alternative refinement strategy, known as k-refinement, is based on a combination of the aforementioned refinement techniques, namely knot insertion and degree elevation, which exhibit non-commutative behavior. This behavior implies that the outcome depends on the sequence in which these operations are performed. In order to achieve higher-degree and increased continuity of basis functions, the k-refinement process begins with elevating the degree from p to the desired degree $p+t$. The subsequent step involves the insertion of new, distinct knot values into the previously degree-elevated knot vector. Maintaining maximum C^{p-1} continuity across element boundaries for all basis functions can only be ensured when the coarsest mesh consists of a single element. The initial continuity constraints across element boundaries will be preserved on all meshes during this process. Importantly, this refinement procedure does not have an analogue in classical finite element analysis.

Additional insights into refinement can be found in [16, 18, 32].

4.2 Isogeometric analysis of bimodular beam vibration

4.2.1 Linear vibration analysis

Starting from the bimodular beam, which shows no difference in effective bending stiffness between upward and downward bending, the free vibration equation can be derived by setting $p(x,t) = 0$ in Eq. (3.21), leading to

$$\Big(D - B\zeta_0\Big)w(x,t)_{,xxxx} + \mu\ddot{w}(x,t) = 0 \tag{4.12}$$

The solution to this homogeneous partial differential equation can be found using the method of separating variables, [10, 14, 15], given by

$$w(x,t) = \phi(x)q(t) \tag{4.13}$$

Substituting this equation along with its corresponding derivatives in Eq. (4.12) yields to

$$-\frac{\ddot{q}(t)}{q(t)} = \frac{\Big(D - B\zeta_0\Big)\phi(x)_{,xxxx}}{\mu\phi(x)} \equiv \omega^2 \tag{4.14}$$

Since this equation must be satisfied for arbitrary values of x and t, both sides can only be the same constant, which is denoted by ω^2. As a result, this equation gives two ordinary differential equations, one governing time function $q(t)$ and the other governing the spatial function $\phi(x)$. These equations are expressed as follows

$$\ddot{q}(t) + \omega^2 q(t) = 0 \tag{4.15a}$$

$$\Big(D - B\zeta_0\Big)\phi(x)_{,xxxx} - \omega^2\mu\phi(x) = 0 \tag{4.15b}$$

The first equation shows the same form as the governing equation for the free vibration of a linear undamped single-degree-of-freedom (SDOF) system characterized by a natural circular frequency ω. With the stiffness and mass characteristics of the system, an infinite series of frequencies ω and their corresponding modes $\phi(x)$ can be identified, satisfying the eigenvalue problem and boundary conditions for the bimodular beam.

Specifically, when considering a simply supported bimodular beam with the following homogeneous boundary conditions, [14, 15, 38]

$$w(x=0,t) = 0 \qquad w(x=l,t) = 0 \tag{4.16a}$$

$$w(x=0,t)_{,xx} = 0 \qquad w(x=l,t)_{,xx} = 0 \tag{4.16b}$$

the general solution of Eq. (4.15b) under the application of these boundary conditions provides the natural circular frequencies, obtained analytically as

$$\omega_k = \left(\frac{k\pi}{l}\right)^2 \sqrt{\frac{D - B\zeta_0}{\mu}} \qquad k = 1, 2, \ldots \tag{4.17}$$

The determination of numerical values for these natural circular frequencies ω_k involves the derivation of the weak form of Eq. (4.15b) using the method of weighted residuals. Multiplying

Eq. (4.15b) by a test function $v(x)$, integrating over the length of the beam l, and applying integration by parts twice to the first term gives the weak form as follows

$$\int_0^l \Big(D - B\zeta_0\Big)\,\phi(x)_{,xx}\,v(x)_{,xx}\,\mathrm{d}x - \omega^2 \int_0^l \mu\phi(x)\,v(x)\,\mathrm{d}x$$
$$= \Big(D - B\zeta_0\Big)\Big[\phi(x)_{,xx}\,v(x)_{,x} - \phi(x)_{,xxx}\,v(x)\Big]_0^l \tag{4.18}$$

In the case of a simply supported bimodular beam with homogeneous boundary conditions as defined in Eq. (4.16), the weak form reduces to

$$\int_0^l \Big(D - B\zeta_0\Big)\,\phi(x)_{,xx}\,v(x)_{,xx}\,\mathrm{d}x - \omega^2 \int_0^l \mu\,\phi(x)\,v(x)\,\mathrm{d}x = 0 \tag{4.19}$$

Isogeometric analysis employs the isoparametric concept, which involves using the same basis function to construct both the exact original geometric model and to approximate the unknown solution fields. By utilizing a B-spline basis function of degree p generated from an open knot vector Ξ and control points $\mathbf{P}_i \in \mathbb{R}^1$, the parametrization of the x-coordinate is given by

$$x(\xi) = \sum_{i=1}^{n} N_{i,p}(\xi)\mathbf{P}_i \tag{4.20}$$

To solve the weak formulation, represented by Eq. (4.19), Galerkin's method is applied, approximating the spatial function $\phi(x)$ of the bimodular beam as follows

$$\phi^h(x) = \sum_{i=1}^{n} N_{i,p}(x)\hat{w}_i \tag{4.21}$$

where $\hat{w}_i$ denotes the control variables. In the standard Galerkin formulation, the test function $v(x)$ involves the same shape functions as the approximated solution $\phi(x)$. Therefore, substituting the shape function expansions into the weak form (4.19) gives the well-known discrete eigenvalue or characteristic value problem, [14, 16, 17]

$$\Big(\mathbf{K} - \omega^2\mathbf{M}\Big)\boldsymbol{\phi} = \mathbf{0} \tag{4.22}$$

Here, $\mathbf{K}$ and $\mathbf{M}$ represent the global stiffness and mass matrices, respectively. These global matrices are determined through the assembly of the element matrices, [30, 35], defined as

$$\mathbf{K}_e = \int_0^{l_e} \mathbf{N}_{,xx}\Big(D - B\zeta_0\Big)\mathbf{N}_{,xx}^T\,\mathrm{d}x \tag{4.23a}$$

$$\mathbf{M}_e = \int_0^{l_e} \mathbf{N}\mu\,\mathbf{N}^T\,\mathrm{d}x \tag{4.23b}$$

where $\mathbf{N}$ represents the vector of shape functions at the element level, and l_e is the length of the element. Within this context, elements are defined by the knot spans. Each element, together with its local function number, is connected to a global number within the framework of the index

space. At the element level, numerical integration is carried out utilizing the Gauss quadrature rule. To achieve this, the integral needs to be transformed back into the bi-unit parent element, which requires the application of the inverses of two mappings. Namely, the first inverse mapping transforms from the physical space to the parameter space, while the second inverse mapping transforms from the parameter space to the bi-unit parent element. The basis functions and their derivatives must be evaluated at each quadrature point within the parent element. Moreover, the Jacobian determinant of the mappings must also be determined to perform the numerical integration, [16].

After determining the stiffness and mass matrices, the scalar quantity ω^2 and vector $\boldsymbol{\phi}$ can be obtained from Eq. (4.22), which represents a homogeneous algebraic equation system. The equation system has a trivial solution $\boldsymbol{\phi} = \mathbf{0}$, which provides no useful information as it indicates no motion. However, the nontrivial solutions exist under the following condition

$$\det\left[\mathbf{K} - \omega^2\mathbf{M}\right] = \mathbf{0} \tag{4.24}$$

This equation is commonly referred to as the characteristic equation or frequency equation. Expanding the determinant yields an algebraic equation in terms of ω^2, whose roots are also known as eigenvalues or characteristic values. These roots determine N natural circular frequencies ω_k $(k = 1, 2, ..., N)$ of vibration, arranged in increasing sequence from the smallest to the largest. Knowing natural frequencies ω_k, the corresponding vectors $\boldsymbol{\phi}_k$ can be obtained from Eq. (4.22), referred to as eigenvectors or characteristic vectors. These vectors are also known as the natural modes or shapes of vibration, [14, 15].

The assembly of N eigenvalues ω_n^2 into a diagonal matrix forms the spectral matrix of the eigenvalue problem as

$$\boldsymbol{\Omega}^2 = \begin{bmatrix} \omega_1^2 & & & \\ & \omega_2^2 & & \\ & & \ddots & \\ & & & \omega_N^2 \end{bmatrix} \tag{4.25}$$

The set of N corresponding eigenvectors can also be compactly arranged into a square matrix, termed the modal matrix, given by

$$\boldsymbol{\Phi} = \begin{bmatrix} \boldsymbol{\phi}_1 & \boldsymbol{\phi}_2 & \cdots & \boldsymbol{\phi}_N \end{bmatrix} = \begin{bmatrix} \phi_{11} & \phi_{12} & \cdots & \phi_{1N} \\ \phi_{21} & \phi_{22} & \cdots & \phi_{2N} \\ \vdots & \vdots & \ddots & \vdots \\ \phi_{N1} & \phi_{N2} & \cdots & \phi_{NN} \end{bmatrix} \tag{4.26}$$

The equations governing the relationship between all eigenvalues and eigenvectors can be rewritten utilizing the spectral and modal matrices as follows

$$\mathbf{K}\boldsymbol{\Phi} = \mathbf{M}\boldsymbol{\Phi}\boldsymbol{\Omega}^2 \tag{4.27}$$

There are several techniques for normalizing vibration modes. One commonly used method involves normalizing each mode such that it satisfies the following conditions

$$\boldsymbol{\Phi}^T\mathbf{M}\boldsymbol{\Phi} = \mathbf{I} \qquad \boldsymbol{\Phi}^T\mathbf{K}\boldsymbol{\Phi} = \boldsymbol{\Omega}^2 \tag{4.28}$$

where $\mathbf{I}$ denotes identity matrix. This equation ensures that the vibration modes are orthogonal to each other and simultaneously normalized with respect to the mass matrix. The mode shapes, normalized in this manner, are called orthonormal relative to the mass matrix.

Finally, the discretized equation of motion of a viscously damped bimodular beam can be written as

$$\mathbf{M}\ddot{\mathbf{q}}(t) + \mathbf{C}\dot{\mathbf{q}}(t) + \mathbf{K}\mathbf{q}(t) = \mathbf{f}_{ex}(t) \tag{4.29}$$

where $\mathbf{C}$ is the viscous damping matrix, $\mathbf{q}(t)$ is the displacement vector, $\dot{\mathbf{q}}(t) = \mathrm{d}\mathbf{q}(t)/\mathrm{d}t$ is the velocity vector, $\ddot{\mathbf{q}}(t) = \mathrm{d}^2\mathbf{q}(t)/\mathrm{d}t^2$ is the acceleration vector and $\mathbf{f}_{ex}(t)$ is the external force vector.

4.2.2 Nonlinear vibration analysis

Compared to a system with uniform effective bending stiffness for upward and downward bending, resulting in a linear vibrational response, the bimodular beam exhibits nonlinear behavior in the presence of a difference in the effective stiffnesses. In this case, the analysis of the bimodular structure entails considering linear and nonlinear internal forces, which arise from the difference in effective bending stiffness. The discretized equation of motion can be formulated by extending the previously derived equation for the linear case, as represented in Eq. (4.29), to include additional internal forces. In this nonlinear case, the equation of motion is expressed as

$$\underbrace{\mathbf{M}\ddot{\mathbf{q}}(t) + \mathbf{C}\dot{\mathbf{q}}(t) + \mathbf{K}\mathbf{q}(t)}_{\mathbf{f}_{lin}(\mathbf{q},\dot{\mathbf{q}},\ddot{\mathbf{q}})} + \mathbf{f}_{nl}(\mathbf{q}) = \mathbf{f}_{ex}(t) \tag{4.30}$$

Here, $\mathbf{f}_{lin}(\mathbf{q}, \dot{\mathbf{q}}, \ddot{\mathbf{q}})$ and $\mathbf{f}_{nl}(\mathbf{q})$ denote the linear and nonlinear internal force vectors, respectively. However, the stiffness matrix $\mathbf{K}$ within the linear internal force vector is determined by the element stiffness matrices, which are defined by the effective bending stiffness corresponding to the downward bending state, expressed as

$$\mathbf{K}_e = \int_0^{l_e} \mathbf{N}_{,xx}\left(D^{(+)} - B^{(+)}\zeta_0^{(+)}\right)\mathbf{N}_{,xx}^T \,\mathrm{d}x \tag{4.31}$$

Consequently, the global stiffness matrix does not depend on the displacement vector $\mathbf{q}(t)$ and remains constant throughout the entire motion. In contrast, the introduced additional internal force vector, denoted by $\mathbf{f}_{nl}(\mathbf{q})$, depends on the displacement vector and is defined as

$$\mathbf{f}_{nl}(\mathbf{q}) = \begin{cases} (\alpha - 1)\mathbf{K}\mathbf{q}(t) & \mathbf{q}(t) \geq 0 \\ 0 & \mathbf{q}(t) < 0 \end{cases} \tag{4.32}$$

where α indicates the effective bending stiffness ratio, as defined in Eq. (3.32). For this nonlinear behavior, Eq. (4.30) represents the dynamic equilibrium of linear and nonlinear internal forces on the one side and external forces on the other.

In this thesis, the vibration response due to the initial conditions or excitations varying arbitrarily with time will be analyzed using the modified Newmark's method, as detailed in Table 2.1 in Chapter 2, adjusted for multi-degree-of-freedom systems. However, for systems under periodic excitation where the focus lies on steady-state response, employing time integration methods such as Newmark, central difference, Euler, or Runge-Kutta can result in significant computational effort. To achieve sufficient accuracy using these methods, the time step size must be selected to be significantly smaller than the period of vibration. Additionally, the time integration process must be conducted over multiple periods until a steady-state response is

attained. For this reason, the analysis of the steady-state response will utilize the harmonic balance method.

4.2.2.1 Derivation of harmonic balance equations

For an ordinary or differential-algebraic equation system, a regular periodic solution can be expressed using a Fourier series. Often, sufficient accuracy is achieved by considering only a small subset of the series' terms. Therefore, a logical approach involves seeking an approximate solution through a truncated Fourier series. This method, known as Harmonic Balance (HB), relies on a truncated Fourier series expansion to approximate periodic solutions, [11, 12, 36, 54–56]. When a system is subjected to a T_p-periodical external forces $\mathbf{f}_{ex}(t) = \mathbf{f}_{ex}(t + jT_p)$, the system's response is expected to be periodic and can be expressed as a harmonic series with a finite number N of cosine and sine terms, as follows

$$\mathbf{q}(t) = \mathbf{a}^0 + \sum_{j=1}^{N} \mathbf{a}^{(j)} \cos \nu_j t + \sum_{j=1}^{N} \mathbf{b}^{(j)} \sin \nu_j t \tag{4.33}$$

where j denotes the harmonic index. The circular frequency of the j^{th} harmonic is defined as

$$\nu_j = j\nu_1 = j\frac{2\pi}{T_p} \tag{4.34}$$

The term with frequency ν_1 is known as the fundamental harmonic, while those with frequencies where $j \geq 2$ are classified as higher harmonics. Furthermore, $\mathbf{a}^0$ represents a vector containing the average value of the unknown amplitudes, whereas $\mathbf{a}^j$ and $\mathbf{b}^j$ refer to collections of Fourier coefficients in vectors, representing the unknown amplitudes of the j^{th} harmonic with exciting circular frequency ν_j. After substituting Eq. (4.33) and its corresponding time derivatives into the discretized equation of motion, as shown in Eq. (4.30), a non-zero residual, denoted by a residual vector $\mathbf{r}(t)$, arises due to the Fourier approximation, which is given by

$$\mathbf{M}\ddot{\mathbf{q}}(t) + \mathbf{C}\dot{\mathbf{q}}(t) + \mathbf{K}\mathbf{q}(t) + \mathbf{f}_{nl}(\mathbf{q}) - \mathbf{f}_{ex}(t) =: \mathbf{r}(t) \neq 0 \tag{4.35}$$

Given the periodic nature of the solution approximation in Eq. (4.33), the corresponding residual $\mathbf{r}(t)$ also exhibits periodicity. However, an alternative approach to representing the displacement vector approximation is through the exponential form of the Fourier series, utilizing the inverse Euler relations, which yields

$$\mathbf{q}(t) = \sum_{j=-N}^{N} \hat{\mathbf{Q}}_j(i\nu_j) e^{i\nu_j t} \tag{4.36}$$

where $e^{i\nu_j t}$ indicate Fourier base functions, and i denotes the imaginary unit, defined as $i^2 = -1$. The complex Fourier coefficient vectors are given by

$$\hat{\mathbf{Q}}_j(i\nu_j) = \frac{1}{T_p} \int_0^{T_p} \mathbf{q}(t) e^{-i\nu_j t} \, \mathrm{d}t \qquad j = 0, \pm 1, \pm 2, ..., \pm N \tag{4.37}$$

The complex-valued coefficient vector $\hat{\mathbf{Q}}_j$ defines both the amplitudes and phases of the j^{th} harmonic. It is evident from Eq. (4.37) that the following relation holds

$$\hat{\mathbf{Q}}_j(i\nu_j) = \hat{\mathbf{Q}}^*_{-j}(i\nu_j) \tag{4.38}$$

where the asterisk denotes the complex conjugate. This complex conjugate pair ensures the elimination of the imaginary parts, leading to the formation of a real-valued sum over these pairs. Moreover, when $j = 0$, a real-valued term emerges as well. Therefore, these two properties contribute to the formation of the real-valued sum presented in Eq. (4.36), which is essential for ensuring the real-valued nature of $\mathbf{q}(t)$. Finally, the approximation of the unknown displacement vector can be rewritten as follows

$$\mathbf{q}(t) = \Re\left\{ \sum_{j=0}^{N} \mathbf{Q}_j(i\nu_j) e^{i\nu_j t} \right\} \tag{4.39}$$

In this case, the Fourier coefficient vectors for each harmonic are defined as

$$\mathbf{Q}_0 = \hat{\mathbf{Q}}_0 \tag{4.40a}$$

$$\mathbf{Q}_j(i\nu_j) = 2\hat{\mathbf{Q}}_j(i\nu_j) \qquad j = 1, 2, ..., N \tag{4.40b}$$

The first and second derivatives of the Fourier series in Eq. (4.39) with respect to time can be determined as follows

$$\dot{\mathbf{q}}(t) = \Re\left\{ \sum_{j=0}^{N} i\nu_j \mathbf{Q}_j(i\nu_j) e^{i\nu_j t} \right\} \qquad \ddot{\mathbf{q}}(t) = \Re\left\{ \sum_{j=0}^{N} -\nu_j^2 \mathbf{Q}_j(i\nu_j) e^{i\nu_j t} \right\} \tag{4.41}$$

Substituting Eq. (4.39) and its first and second time derivatives from Eq. (4.41) into Eq. (4.35) results in

$$\Re\left\{ \sum_{j=0}^{N} \Big(-\nu_j^2 \mathbf{M} + i\nu_j \mathbf{C} + \mathbf{K} \Big) \mathbf{Q}_j(i\nu_j) e^{i\nu_j t} \right\} + \mathbf{f}_{nl}(\mathbf{q}) - \mathbf{f}_{ex}(t) = \mathbf{r}(t) \tag{4.42}$$

The nonlinear force vector $\mathbf{f}_{nl}(\mathbf{q})$ and external force vector $\mathbf{f}_{ex}(t)$ can be also represented by Fourier series of the truncation order N, leading to the following expression

$$\Re\left\{ \sum_{j=0}^{N} \Big[\mathbf{S}_j(i\nu_j) \mathbf{Q}_j(i\nu_j) + \mathbf{F}_{nl,j}(\mathbf{Q}_j) - \mathbf{F}_{ex,j}(i\nu_j) \Big] e^{i\nu_j t} \right\} = \mathbf{r}(t) \tag{4.43}$$

The appearing linear internal forces in this equation, represented by $\mathbf{S}_j(i\nu_j)\mathbf{Q}_j(i\nu_j)$, are expressed using the dynamic stiffness matrix $\mathbf{S}_j(i\nu_j)$, which is defined for each harmonic index j as

$$\mathbf{S}_j(i\nu_j) = -\nu_j^2 \mathbf{M} + i\nu_j \mathbf{C} + \mathbf{K} \tag{4.44}$$

Given an external force vector $\mathbf{f}_{ex}(t)$ in the time domain, its Fourier coefficients are generally known or can be obtained using a similar approach as described in the derivation of Eq. (4.39), resulting in

$$\mathbf{f}_{ex}(t) = \Re\left\{ \sum_{j=0}^{N} \mathbf{F}_{ex,j}(i\nu_j) e^{i\nu_j t} \right\} \tag{4.45}$$

In the absence of nonlinear forces, specifically when only linear internal and external forces are present, the equations depicted in Eq. (4.43) become decoupled for distinct harmonics. However, in the presence of nonlinear forces, the equations become coupled across different harmonics, making it impossible to solve them independently for each harmonic index j. The Fourier coefficients of the nonlinear forces, gathered in the vector $\mathbf{F}_{nl,j}(\mathbf{Q}_j)$, can be formally expressed as follows

$$\frac{1}{\pi}\int_0^{2\pi} \mathbf{f}_{nl}(\mathbf{q})\, e^{-i\nu_j t}\, \mathrm{d}(\nu t) = \begin{cases} \mathbf{F}_{nl,0} & \\ 2\mathbf{F}_{nl,j}(\mathbf{Q}_j) & j = 1, 2, ..., N \end{cases} \tag{4.46}$$

Alternatively, the discrete Fourier transform (DFT) can also serve as a useful tool for approximating the continuous integral when calculating Fourier coefficients.

Eq. (4.43) represents the dynamic force equilibrium formulated in the frequency domain, which can be rewritten in the following form

$$\Re\left\{\sum_{j=0}^{N} \mathbf{R}_j(i\nu_j) e^{i\nu_j t}\right\} = \mathbf{r}(t) \tag{4.47}$$

where $\mathbf{R}_j(i\nu_j)$ denote residual vector of the corresponding j^{th} harmonic, containing the unknown complex Fourier coefficients, defined as

$$\mathbf{R}_j(i\nu_j) = \mathbf{S}_j(i\nu_j)\mathbf{Q}_j(i\nu_j) + \mathbf{F}_{nl,j}(\mathbf{X}_j) - \mathbf{F}_{ex,j}(i\nu_j) \tag{4.48}$$

The unknown Fourier coefficients can be determined using the method of mean weighted residuals, which involves satisfying the equation of motion in a weighted average sense, given by

$$\frac{1}{T}\int_0^{T} \mathbf{r}(t) w_k(t)\, \mathrm{d}t = \mathbf{0} \qquad k = 1, 2, ..., 2N+1 \tag{4.49}$$

Here, $w_k(t)$ represents the weight function. When utilizing $2N+1$ Fourier basis functions as weights, Eq. (4.49) necessitates the orthogonality of the residual to the Fourier basis functions. In practical terms, this implies that the Fourier coefficients of the residual should vanish up to the truncation order N. This observation suggests that harmonic balance can be interpreted as a Galerkin method, where Fourier basis functions serve as both approximate solutions and weight functions, [53]. Since the Fourier coefficients of the residual $\mathbf{r}(t)$ vanish in the sine-cosine representation, it follows that they should also become zero in the complex-exponential representation due to the properties of complex conjugates. This can be expressed as

$$\mathbf{R}_j(i\nu_j) = \mathbf{0} \qquad j = 0, 1, ..., N \tag{4.50}$$

This equation represents the individual balancing of each harmonic, as implied by the method's name. As a result, an algebraic equation system arises for determining the Fourier coefficients of the approximate solution, denoted by

$$\mathbf{R}(\tilde{\mathbf{x}}) = \mathbf{0} \tag{4.51}$$

where $\mathbf{R}$ denotes the residual function, and $\widetilde{\mathbf{x}}$ represents the vector of unknowns, defined as

$$\mathbf{R} = \begin{bmatrix} \mathbf{R}_0(i\nu_j) \\ \Re\{\mathbf{R}_1(i\nu_j)\} \\ \Im\{\mathbf{R}_1(i\nu_j)\} \\ \vdots \\ \Im\{\mathbf{R}_N(i\nu_j)\} \end{bmatrix} \qquad \widetilde{\mathbf{x}} = \begin{bmatrix} \mathbf{Q}_0(i\nu_j) \\ \Re\{\mathbf{Q}_1(i\nu_j)\} \\ \Im\{\mathbf{Q}_1(i\nu_j)\} \\ \vdots \\ \Im\{\mathbf{Q}_N(i\nu_j)\} \end{bmatrix} \tag{4.52}$$

The nonlinear algebraic equation system can be exactly solved only under particular conditions, such as when the system has one or few degrees of freedom, uncomplicated nonlinear terms, and involves one or two harmonics, as presented in [37]. However, in most cases, obtaining an exact solution is not feasible, necessitating the use of appropriate numerical methods for approximation. Newton's method and its variants are frequently utilized for iteratively solving nonlinear vibration problems.

4.2.2.2 The Newton-Raphson method

One of the most straightforward and widely recognized methods for solving nonlinear algebraic equations is the Newton-Raphson method, [14, 16, 36]. Its key idea involves expanding the residual in a Taylor series about the known estimate $\widetilde{\mathbf{x}}^{(i)}$ as

$$\mathbf{R}\left(\widetilde{\mathbf{x}}^{(i+1)}\right) = \mathbf{R}\left(\widetilde{\mathbf{x}}^{(i)}\right) + \left.\frac{\partial \mathbf{R}(\widetilde{\mathbf{x}})}{\partial \widetilde{\mathbf{x}}}\right|_{\widetilde{\mathbf{x}}^{(i)}} \left(\widetilde{\mathbf{x}}^{(i+1)} - \widetilde{\mathbf{x}}^{(i)}\right) + \frac{1}{2}\left.\frac{\partial^2 \mathbf{R}(\widetilde{\mathbf{x}})}{\partial \widetilde{\mathbf{x}}^2}\right|_{\widetilde{\mathbf{x}}^{(i)}} \left(\widetilde{\mathbf{x}}^{(i+1)} - \widetilde{\mathbf{x}}^{(i)}\right)^2 + \ldots \tag{4.53}$$

If the estimate $\widetilde{\mathbf{x}}^{(i)}$ is near the solution, the change in $\widetilde{\mathbf{x}}$, represented as $\Delta\widetilde{\mathbf{x}}^{(i)} = \widetilde{\mathbf{x}}^{(i+1)} - \widetilde{\mathbf{x}}^{(i)}$, will be minimal. Consequently, the second and higher-order terms become negligible, resulting in the following linearized expression

$$\mathbf{R}\left(\widetilde{\mathbf{x}}^{(i+1)}\right) \approx \mathbf{R}\left(\widetilde{\mathbf{x}}^{(i)}\right) + \left.\frac{\partial \mathbf{R}(\widetilde{\mathbf{x}})}{\partial \widetilde{\mathbf{x}}}\right|_{\widetilde{\mathbf{x}}^{(i)}} \Delta\widetilde{\mathbf{x}}^{(i)} = \mathbf{0} \tag{4.54}$$

Following the rearrangement of this equation, the change in $\widetilde{\mathbf{x}}$ can be obtained as

$$\Delta\widetilde{\mathbf{x}}^{(i)} = -\left(\left.\frac{\partial \mathbf{R}(\widetilde{\mathbf{x}})}{\partial \widetilde{\mathbf{x}}}\right|_{\widetilde{\mathbf{x}}^{(i)}}\right)^{-1} \mathbf{R}\left(\widetilde{\mathbf{x}}^{(i)}\right) \tag{4.55}$$

After determining $\Delta\widetilde{\mathbf{x}}^{(i)}$, an improved estimate is defined as

$$\widetilde{\mathbf{x}}^{(i+1)} = \widetilde{\mathbf{x}}^{(i)} + \Delta\widetilde{\mathbf{x}}^{(i)} \tag{4.56}$$

Within this context, the matrix $\partial\mathbf{R}(\widetilde{\mathbf{x}})/\partial\widetilde{\mathbf{x}}$, known as the Jacobian matrix, comprises the partial derivatives of the residual with respect to the unknown Fourier coefficients. The iterative process begins with an initial vector $\widetilde{\mathbf{x}}^{(0)}$ and iterates until the residual becomes sufficiently small concerning an appropriate norm, in accordance with a specified tolerance ϵ, which is expressed by

$$\left\|\mathbf{R}\left(\widetilde{\mathbf{x}}^{(i)}\right)\right\| \leq \epsilon \tag{4.57}$$

This iterative procedure is also graphically illustrated in Fig. 4.6.

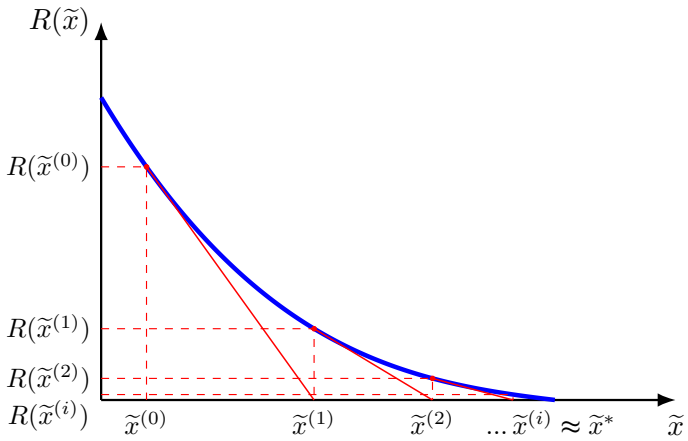

Fig. 4.6: Newton-Raphson iterations in the one-dimensional case, [14, 16]

4.2.2.3 Path continuation method

Generally, there is interest in determining how the amplitude of a response changes with the exciting frequency, thus yielding a frequency-response curve. For this reason, it becomes necessary to define a sequence of exciting frequencies and determine the system's response for each. Since the solution depends strongly on an initial guess, it is practical to use the solution obtained for one frequency value as the initial guess for the next. This iterative procedure is commonly known as sequential continuation. However, nonlinear vibrational behavior may exhibit bifurcations with multiple solution branches and turning points with respect to the exciting frequency as a free parameter, see Fig. 4.7a. In this case, when starting from either the left or the right and stepping until the turning point is reached, any subsequent step leads to a significant jump, resulting in the next solution being far removed from the previous one. Consequently, the procedure may confront convergence difficulties or require a considerable number of iterations to reach a solution. Therefore, the aim is to produce solutions within the defined frequency parameter range and effectively overcome any potential turning points. This approach is referred to as the numerical path continuation method, [36].

This numerical method improves numerical efficiency not only at turning points but also near resonances, characterized by significant gradient changes. Due to the limitations of equidistant spacing of solution points along the frequency parameter and the typical lack of a priori knowledge regarding the exact location of significant gradient changes with respect to the frequency parameter, this frequency parameter is treated as an additional unknown. Therefore, it is included into the vector of unknowns, defined as

$$\mathbf{X} = \begin{bmatrix} \widetilde{\mathbf{x}} \\ \nu \end{bmatrix} \tag{4.58}$$

In this case, the nonlinear algebraic equation system, represented by

$$\mathbf{R}(\mathbf{X}) = \mathbf{0} \tag{4.59}$$

is undetermined and requires an additional equation to ensure the uniqueness of the solution.

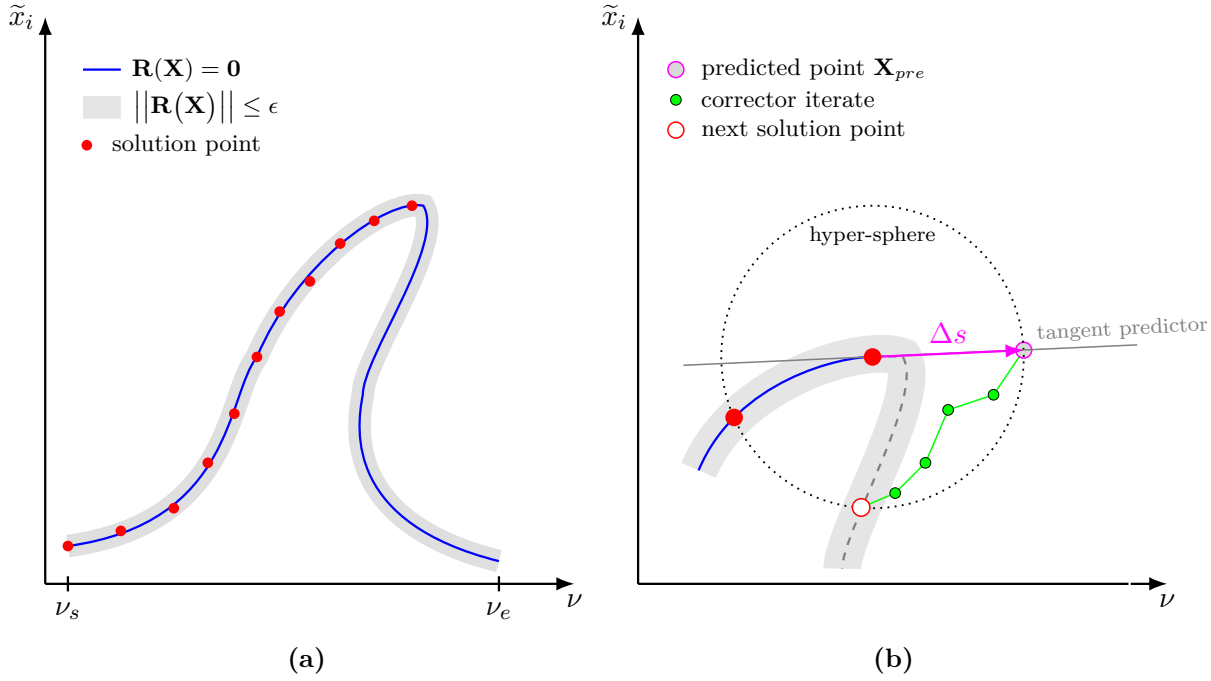

Fig. 4.7: Path continuation method (a) solution branch (b) predictor-corrector method, [36, 56]

Starting from a given solution, denoted by $\mathbf{X}_0$, the next solution point can be predicted by going a certain step Δs in the direction of the tangent to the solution branch, see Fig. 4.7b, which is given by

$$\mathbf{X}_{pre} \approx \mathbf{X}_0 + \Delta s \mathbf{X}_1^* \tag{4.60}$$

where $\mathbf{X}_1^*$ denotes the normalized tangent vector. In general, the tangent vector is determined by solving the following linear algebraic equation system

$$\left.\frac{\partial \mathbf{R}(\mathbf{X})}{\partial \mathbf{X}}\right|_{\mathbf{X}_0} \mathbf{X}_1 = \mathbf{0} \tag{4.61}$$

This equation corresponds to the first-order Taylor series expansion of the residual around the initial solution $\mathbf{X}_0$, which is set to zero to ensure progression in the direction of the tangent. However, Eq. (4.61) specifies the direction of the tangent without defining its length. To determine the length of the tangent vector, the following expression is provided

$$\mathbf{t}^T \mathbf{X}_1 = 1 \tag{4.62}$$

where the vector $\mathbf{t}$ is required to satisfy the condition $\mathbf{t}^T \mathbf{X}_1 \neq 0$, while it is otherwise arbitrary. Usually, the previous tangent vector is employed for this purpose, assuming that the tangent does not make a turn around a 90° angle. Another approach is to normalize the tangent vector to a unit length, as follows

$$\mathbf{X}_1^* = \frac{\mathbf{X}_1}{\sqrt{\mathbf{X}_1^T \mathbf{X}_1}} \tag{4.63}$$

The current tangent vector will be compared with either the tangent vector or the secant vector from the previous step to ensure the process is progressing in the correct direction. In the case of a positive inner product and an appropriate step length, the normalized vector $\mathbf{X}_1^*$ should

accurately indicate the desired direction, predicting the new step according to Eq. (4.60). Another method for predicting the new solution point involves using a secant through the previous two solution points, while an alternative approach is based on a Taylor series expansion of the solution branch using a pseudo-arc-length parameter, as utilized in asymptotic numerical method (ANM), [36, 56].

After determining the solution point through prediction, the current state can be represented by the following equation

$$\mathbf{R}(\mathbf{X}_{pre}) \neq \mathbf{0} \tag{4.64}$$

This implies that a correction is needed to decrease the residual to a desired threshold and obtain an acceptable next solution. As mentioned previously, the nonlinear algebraic equation system is underdetermined, requiring an additional equation to determine the next solution point on the solution path. This necessary additional equation is also denoted as a parametrization constraint. With a specified step size, the goal is to determine a sequence of points along the solution branch, maintaining a constant distance between each point. However, accurately determining the arc length can be challenging, often leading to approximations using the Euclidean distance, as follows

$$(\mathbf{X} - \mathbf{X}_0)^T (\mathbf{X} - \mathbf{X}_0) - \Delta s^2 = 0 \tag{4.65}$$

This additional equation requires that the next solution point is positioned on the surface of a hypersphere with radius Δs around the previous solution point $\mathbf{X}_0$. Now, with the number of equations matching that of the unknowns, the residual can be reformulated as

$$\mathbf{R}_{tot}(\mathbf{X}) = \begin{bmatrix} \mathbf{R}(\mathbf{X}) \\ (\mathbf{X} - \mathbf{X}_0)^T (\mathbf{X} - \mathbf{X}_0) - \Delta s^2 \end{bmatrix} = \mathbf{0} \tag{4.66}$$

The solution to this nonlinear algebraic equation system can be determined by applying the Newton-Raphson method, as represented in the previous subsection, where $\mathbf{R}(\mathbf{x})$ will be replaced by $\mathbf{R}_{tot}(\mathbf{X})$ and the procedure starts with the initial guess

$$\mathbf{X}^{(0)} = \mathbf{X}_0 + \Delta s \mathbf{X}_1^* \tag{4.67}$$

and ends when the residual becomes sufficiently small, as determined by $||\mathbf{R}_{tot}(\mathbf{X}^{(i)})|| \leq \epsilon$.

Chapter 5

Numerical studies

This chapter focuses on the numerical investigation of the beam's response to different types of excitation. The primary aim of this analysis is to show the influence of the beam's elastic properties on its dynamic behavior, with particular attention given to its cross-section. After introducing the material and geometrical properties, as well as determining the natural circular frequencies in Section 5.1, the subsequent section investigates the behavior of both unimodular and bimodular beams during free vibration induced by initial conditions, as elaborated in Section 5.2. In Section 5.3, the variation of system response to pulse excitation is analyzed, whereas the analysis of system response to harmonic excitation is presented in Section 5.4.

5.1 Structural model, material properties and cross-sections

A simply supported Bernoulli-Euler beam with a length of $l = 0.4$ m, as shown in Fig. 5.1, serves as an illustrative example to demonstrate how the system responds to different types of excitations and cross-sections, particularly when the beam is composed of bimodular material characterized by the properties presented in Table 5.1.

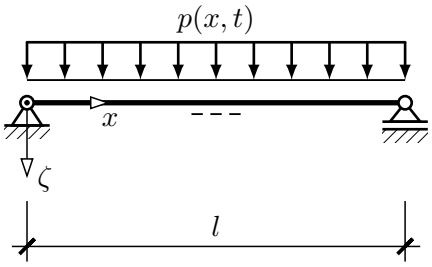

Fig. 5.1: Simply supported beam

Tab. 5.1: Material properties

Young's modulus in tesion:	$E_t = 640$	MPa
Young's modulus in compression:	$E_c = 40$	MPa
Mass density:	$\rho = 1000$	kg/m^3

The effect of the damping is expressed in terms of the mass proportional damping matrix as follows

$$\mathbf{C} = 0.001\omega_1^2\mathbf{M}$$

where ω_1 denotes the fundamental circular frequency of the beam in the case of downward bending motion. This analysis considers three different cross-sections, namely the rectangular, triangular, and T cross-sections, whose parameters are listed in Table 5.2. However, it is evident from this table that the dimensions of cross-sections are chosen in such a way that they have equal cross-sectional area and approximately equal moment of inertia with respect to the η-axis. Note that these cross-sectional parameters are rounded to the nearest whole number.

Tab. 5.2: Cross-sectional parameters

			Rectangular cross-section	Triangular cross-section	T cross-section
Height	h	[mm]	31	38	34 ($t_f = 6.61$)
Width	b	[mm]	15	24.5	50 ($t_w = 4.91$)
Cross-sectional area	A	[mm^2]	465	465	465
Moment of inertia	I_η	[mm^4]	37 239	37 343	37 236
Neutral axis, $w(x,t)_{,xx} < 0$	$\zeta_0^{(-)}$	[mm]	9.30	10.75	12.98
Neutral axis, $w(x,t)_{,xx} > 0$	$\zeta_0^{(+)}$	[mm]	-9.30	-8.05	-5.59
Eff. bending stiffness, $w(x,t)_{,xx} < 0$	D_0	[kNmm^2]	3 813	5 104	6 682
Eff. bending stiffness, $w(x,t)_{,xx} > 0$	D_0	[kNmm^2]	3 813	3 333	2 253
Stiffness ratio	α	[−]	1.00	1.53	2.97

Within this numerical investigation, the B-spline basis functions of degree $p = 4$ are used for constructing the geometric beam model and for approximating the unknown displacement field. For this analysis, the beam is discretized using 16 elements.

Table 5.3 displays the first five natural circular frequencies of the unimodular and bimodular beams. These natural circular frequencies are obtained using Eq. (4.24), where the stiffness matrix is defined by the corresponding effective bending stiffnesses.

Tab. 5.3: Natural circular frequencies ω_k [rad/s] of the unimodular (left) and bimodular (right) beams

k	Rectangular cross-section	Triangular cross-section	T cross-section	Rectangular cross-section	Triangular cross-section	T cross-section
1	110.40	110.50	110.40	176.64	165.06	135.78
2	441.61	441.99	441.60	706.58	660.26	543.12
3	993.63	994.49	993.60	1 589.80	1 485.58	1 222.02
4	1 766.46	1 767.99	1 766.42	2 826.33	2 641.05	2 172.48
5	2 760.13	2 762.53	2 760.08	4 416.21	4 126.70	3 394.56

With the natural circular frequencies of the bimodular beam and the effective bending stiffness ratio α from Table 5.2, the fundamental circular frequency $\omega_{1,bi}$ can be calculated using Eq.(2.38). These circular frequencies for beams with three cross-sections are also provided in the following table

Tab. 5.4: Fundamental circular frequency $\omega_{1,bi}$ [rad/s]

Rectangular cross-section	Triangular cross-section	T cross-section
176.64	182.58	171.80

5.2 Free vibration response

To determine the free vibration response, the beam is subjected to initial displacement and velocity, expressed respectively as spatial sine functions of the beam axis x, as follows

$$w_0(x) = w(x,0) = 0.0001 \sin\left(\frac{\pi x}{l}\right) \qquad \dot{w}_0(x) = \dot{w}(x,0) = 0.03 \sin\left(\frac{\pi x}{l}\right) \tag{5.1}$$

In Fig. 5.2, the transverse displacements at midspan, represented by $w(l/2,t)$ and normalized with respect to the initial displacement at midspan denoted by $w_0(l/2)$, are plotted against the ratio of time t to the fundamental period of vibration of the unimodular beam, denoted by $T_{1,uni}$. More precisely, this period of vibration pertains to the unimodular beam with a rectangular cross-section. However, due to negligible differences in moment of inertia among cross-sections, resulting in almost identical vibration periods of unimodular beams, the period $T_{1,uni}$ universally denotes across all three without specific reference to the cross-section.

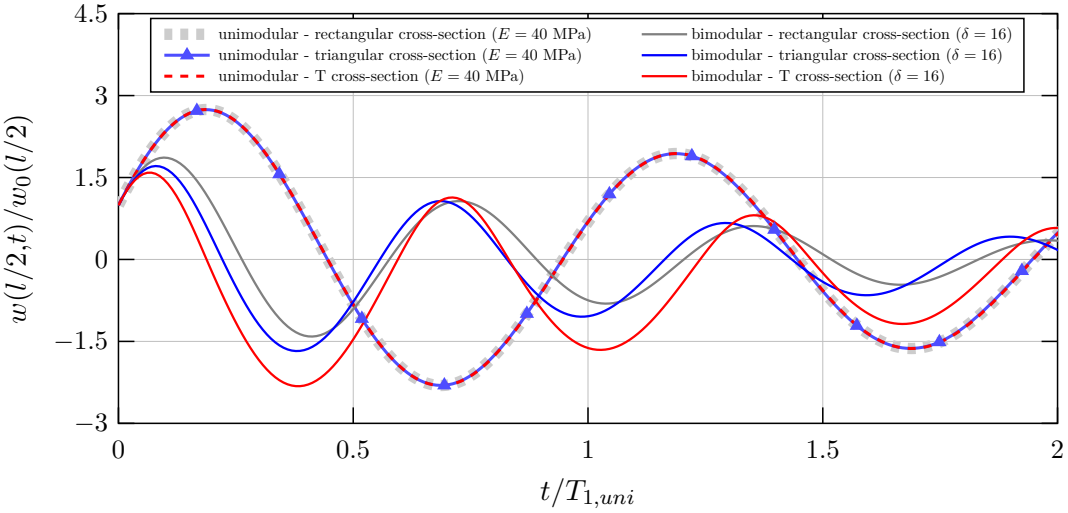

Fig. 5.2: Free-vibration response, time normalized by $T_{1,uni}$

From this figure, it becomes apparent that there are significant differences not only in amplitude but also in period of vibration between the displacement responses of unimodular and bimodular beams, arising from differing bending stiffnesses. However, due to the nearly identical bending stiffnesses of beams made from unimodular material with three cross-sections, their displacement responses coincide. In this unimodular case, the bending stiffness is determined by Young's modulus in compression $E = E_c = 40$ MPa. On the other hand, the dynamic responses of beams composed of materials with different Young's moduli for tension and compression, characterized by a modular ratio $\delta = 16$, do not coincide, demonstrating variations in both amplitude and vibration period. This discrepancy arises from the influence of cross-sectional geometry on determining the position of the neutral axis, which consequently affects the bending stiffness of the beam. Table 5.2 clearly indicates that absolute values of the neutral axis position differ for upward and downward bending in the case of the isosceles triangle and T cross-section, but are equal in the case of the rectangular cross-section, as also discussed in Section 3.5. This implies that beams with triangular and T cross-sections possess a higher effective bending stiffness during upward bending than downward bending, resulting in smaller amplitudes and shorter durations. In contrast, the beam with a rectangular cross-section maintains consistent amplitudes

and durations for both upward and downward bending. The following Fig. 5.3 illustrates how the response of each bimodular beam varies over its own fundamental period of vibration, as indicated by the normalized time t/T_1.

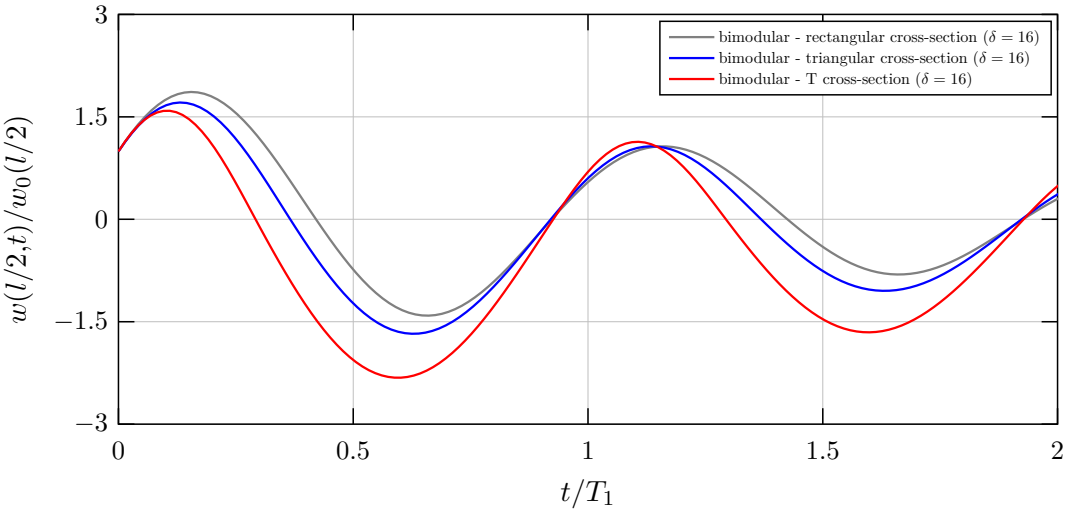

Fig. 5.3: Free-vibration response, time normalized by T_1

5.3 Dynamic response to half-cycle sine pulse excitation

As part of this numerical analysis, the second type of excitation is represented by a half-cycle sinusoidal pulse. For the purpose of dynamic investigation, an impulse load, denoted by $p(x,t)$, is uniformly applied along the beam, as illustrated in Fig. 5.1. Referring to Fig. 5.4, the pulse excitation is defined as follows

$$p(x,t) = \begin{cases} p_0 \sin \dfrac{\pi t}{t_d} & t/T_{1,uni} \leq t_d/T_{1,uni} \\ 0 & t/T_{1,uni} \geq t_d/T_{1,uni} \end{cases}$$

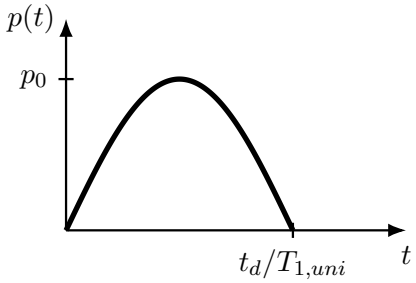

Fig. 5.4: Half-cycle sine pulse

where $p_0 = 5$ N/m represents the amplitude of the uniformly distributed transverse dynamic load across the entire beam length $l = 0.40$ m, while $t_d/T_{1,uni} = 1.25$ denotes the duration of the half-cycle sine pulse, normalized by the fundamental period of vibration. The corresponding initial conditions, displacement $w_0(x)$ and velocity $\dot{w}_0(x)$ are assumed to be zero.

Fig. 5.5 shows the normalized time variation of the normalized displacement at the midspan, denoted by $w(l/2,t)/w_{st,uni}(l/2)$, for the given ratio $t_d/T_{1,uni}$. Here, $w_{st,uni}(l/2)$ represents the static deformation of the unimodular beam with rectangular cross-section at the midspan due to pulse load amplitude p_0. Similar to $T_{1,uni}$, this static deformation is denoted without reference

to the rectangular cross-section due to the negligible difference in the moment of inertia and, consequently, in bending stiffness. This leads not only to identical static deformations but also to the dynamic responses of unimodular beams, as depicted in Fig. 5.5. However, this is not observed in the case of bimodular beams, which exhibit differing responses in both phases. More precisely, the responses to the pulse are segmented into two phases, namely, the initial phase corresponds to the forced vibration phase, occurring while the load is applied and visually indicated in the figure by light red color, followed by the subsequent free vibration phase.

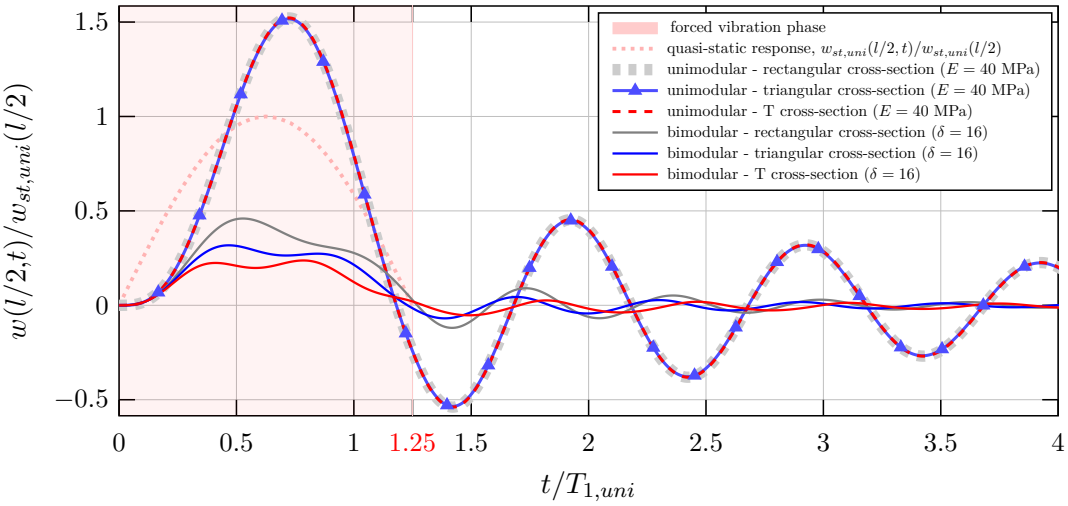

Fig. 5.5: Dynamic responses to half-cycle sine pulse

In order to provide a clearer illustration of the differences in dynamic responses exclusively between bimodular beams, their responses are depicted separately in the following Fig. 5.6 below.

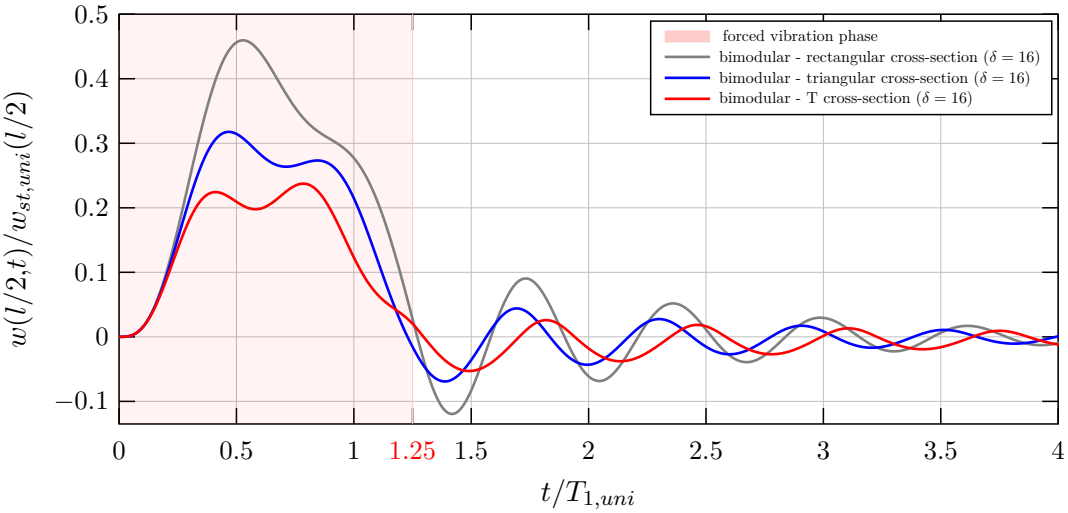

Fig. 5.6: Dynamic responses of bimodular beams to half-cycle sine pulse

From this figure, it becomes evident that bimodular beams with different cross-sections exhibit significant differences in their responses, which are caused by the geometric characteristics of the

cross-sections affecting the effective bending stiffnesses. Remarkably, the maximum deformations occur during the pulse. However, in this forced vibration phase, the bimodular beam with triangular cross-section experiences a reduction in maximum deformation of about 30% compared to the beam with a rectangular cross-section, while the beam with T cross-section shows an even more significant decrease of approximately 50%. After the pulse ends, the beams vibrate freely, influenced by the displacements and velocities at the end of the pulse. As a result of the varying behavior of the beams during the forced vibration phase, the displacements and velocities at the beginning of the free vibration phase also differ. Compared to the dynamic responses observed under initial displacement and velocity, which were consistent across all beams, as analyzed in the previous Subsection 5.2 and depicted in Figs. 5.2 and 5.3, the disparities become more significant immediately at the beginning of the free vibration phase. Specifically, the amplitudes of the bimodular beam with a rectangular cross-section exceed those of beams with the other two cross-sections.

5.4 Dynamic response to harmonic excitation

In the following case, the focus shifts to periodic excitation, representing the final type of excitation in this numerical study. The system is subjected to a uniformly distributed transverse load across its entire length $l = 0.40$ m, as depicted in Fig. 5.1. This load varies harmonically in time according to the following expression

$$p(x,t) = p_0 \cos \nu t \tag{5.2}$$

Here, the ratio of exciting circular frequency to the fundamental circular frequency of unimodular beam with the rectangular cross-section is chosen to be $\nu/\omega_{1,uni} = 0.54$. The amplitude of the dynamic load remains unchanged from the previous subsection, set at $p_0 = 5$ N/m. Similar to these two quantities, $T_{1,uni}$ and $w_{st,uni}$, the fundamental circular frequency $\omega_{1,uni}$ is referred to without specifying the rectangular cross-section. This frequency represents the first circular frequency of all three unimodular beams due to their negligible differences in bending stiffness, resulting in consistent static and dynamic responses, as elaborated in the preceding subsections. The coinciding dynamic responses of unimodular beams mentioned are represented in Fig. 5.7.

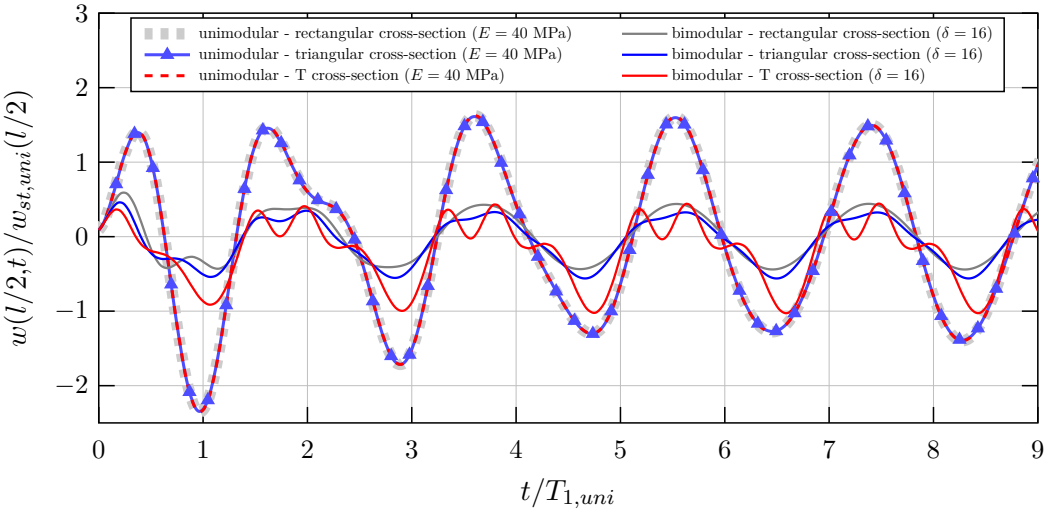

Fig. 5.7: Dynamic responses to cosine-wave load

This analysis assumes the same initial conditions as those given in Subsection 5.2 and expressed by Eq. (5.1). The influence of transient vibrations is clearly evident in the figure, gradually diminishing exponentially over time until it becomes negligible in both unimodular and bimodular cases. As expected, the dynamic responses of bimodular beams exhibit variations also with this excitation case due to the aforementioned differences in effective bending stiffness. Additionally, Fig. 5.8 exclusively illustrates the dynamic responses of only bimodular beams, providing a more transparent comparison of their differences.

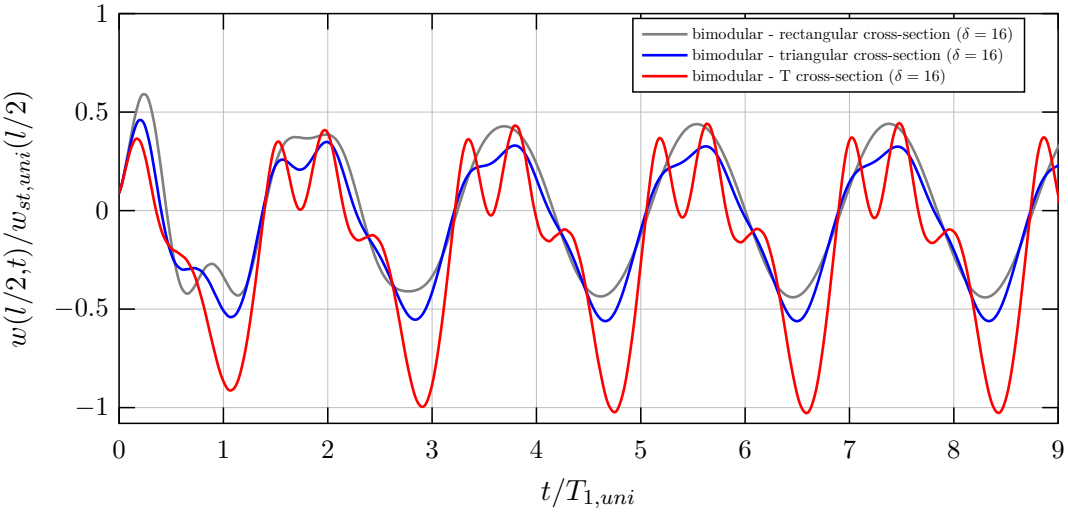

Fig. 5.8: Dynamic responses of bimodular beams to cosine-wave load

Due to the consistent effective bending stiffness of the rectangular cross-section beam for both bending states, as indicated in Table 5.2, the corresponding dynamic response remains uniform, showing no variation in steady-state amplitude between vibration half-cycles. In contrast, beams with triangular and T cross-sections demonstrate distinct behavior under the two bending configurations. Fig. 5.8 illustrates that the triangular cross-section beam exhibits approximately 45% smaller amplitudes during downward bending compared to the T cross-section, while the rectangular cross-section shows about 57% smaller amplitudes. During upward bending, the differences in maximum displacement values are considerably diminished. However, as shown in the figure, the bimodular beam with the rectangular cross-section shows purely linear vibration behavior due to the absence of stiffness differences, as indicated by the effective bending stiffness ratio $\alpha = 1$. On the other hand, the steady-state responses of bimodular beams with triangular and T cross-sections contain additional harmonics, indicating the presence of nonlinear phenomena. This nonlinear behavior is significantly more pronounced in the case of the T cross-section due to its higher effective bending stiffness ratio α, which is almost double that of the triangular cross-section. For this reason, it is necessary to analyse the system's behavior not only in the time domain but also in the frequency domain to identify how the amplitudes vary with excitation frequency.

The unimodular and bimodular beams are analyzed in the frequency domain using the harmonic balance method outlined in the Chapter 4. Fig. 5.9 shows the frequency-response functions of the midspan deflection, denoted by the amplitude $|a|$, for each material-specific beam with three different cross-sections. These frequency-response curves are normalized by static deformation at the midspan of the unimodular beam with rectangular cross-section, represented by $a_{st,uni}$. In a similar manner, the excitation circular frequency ν is also normalized by the fundamental circular frequency of the unimodular beam with the rectangular cross-section, denoted by $\omega_{1,uni}$.

In this case, there is no reference to the rectangular cross-section for the same reasons previously mentioned regarding other quantities employed in normalization. Starting from a frequency ratio of $\nu/\omega_{1,uni} = 0.2$, the solution points necessary to define the frequency-response curve are determined following the procedure detailed in Subsection 4.2.2, concluding when $\nu/\omega_{1,uni} = 3$.

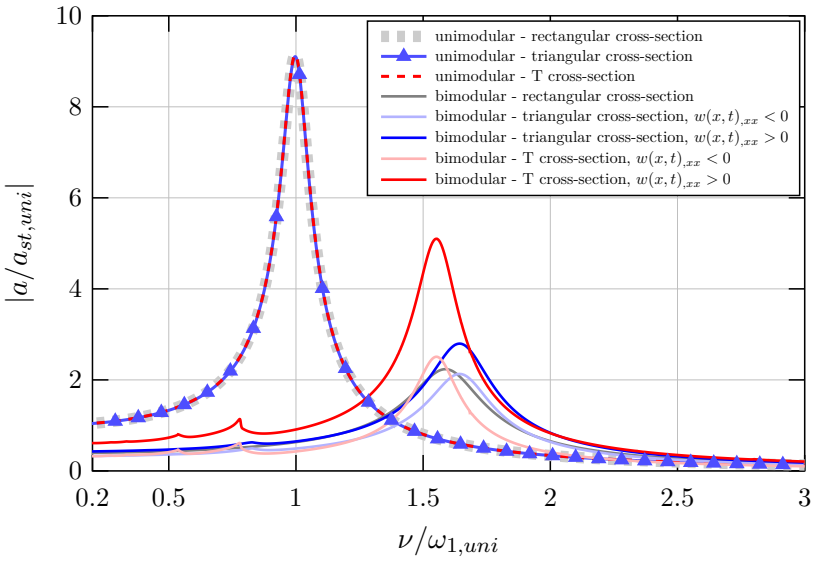

Fig. 5.9: Frequency-response curves at midspan

It is evident that the responses of the unimodular beam across all three analyzed cross-sections are not only identical in the time domain, as previously demonstrated but also in the frequency domain. This consistency directly results from the previously discussed facts concerning bending stiffnesses. However, due to stiffening effect caused by Young's modulus in tension, the peaks of the frequency-response curves for the bimodular beams are reduced in magnitude and shifted to the right along the frequency ratio axis. For a clearer illustration of the differences between them, they are presented separately in Fig. 5.10 below.

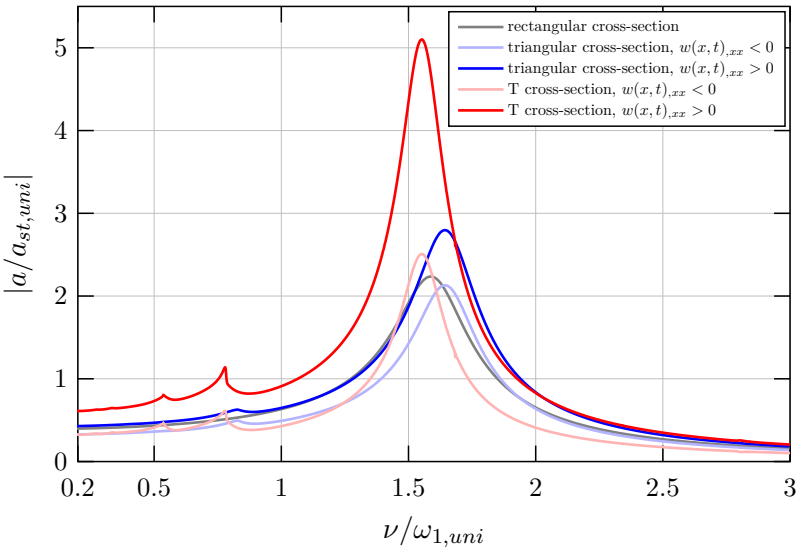

Fig. 5.10: Frequency-response curves at midspan of bimodular beams

A single gray curve represents the frequency-response function of the bimodular beam with the rectangular cross-section. In this case, the system behaves linearly due to the absence of nonlinear forces, resulting in the absolute values of amplitudes remaining equal for both bending states. Conversely, the bimodular beams with triangular and T cross-sections show nonlinear effects caused by additional forces arising from differences in effective bending stiffnesses between the two bending configurations. As a consequence, the varying amplitudes between upward and downward bending require amplitude-frequency curves to be provided for both bending cases, as illustrated in Fig. 5.10. Remarkably, as previously demonstrated through analysis in the time domain with a single excitation circular frequency, the amplitudes are generally larger during downward bending across the entire considered frequency range.

As stated before, the stiffening effect induced by Young's modulus in tension not only decreases the amplitude but also shifts the resonances rightward along the frequency ratio axis, approximately reaching a circular frequency ratio of $\omega_{1,bi}/\omega_{1,uni}$. In contrast to the fundamental circular frequencies of the unimodular beams, the circular frequency $\omega_{1,bi}$ varies among the bimodular beams, resulting in different circular frequency ratios at which their resonances occur. More precisely, in this numerical investigation, the peak of the frequency-response curve of the bimodular beam with a rectangular cross-section shifts by 60% towards higher frequencies. Additionally, the peaks for the beam with a triangular cross-section moves by 65%, while for the T cross-section, they shift by 56%, all relative to the peak of unimodular beams. Therefore, when compared to the peak of the frequency-response curve of the bimodular beam with a rectangular cross-section as a reference, both peaks of the beam with a triangular cross-section are shifted by 5% towards higher frequencies. In contrast, the peaks of the beam with the T cross-section are located 4% lower towards lower frequencies.

From Fig. 5.10, it is evident that there are additional small peaks within the frequency ratio range between 0.2 and 1. However, these peaks are exclusively present in the bimodular beams with triangular and especially with T cross-sections, indicating the nonlinear behavior of the systems arising from differences in stiffness. In other words, they are induced by additional forces that depend on the effective stiffness differences represented by stiffness ratio α. These asymmetric additional forces, varying between upward and downward bending, lead to significant interactions between the fundamental and higher harmonics. Consequently, the bimodular beam undergoes vibrations not only with external excitation frequency but also with higher frequencies, which are integer multiples of a given fundamental excitation frequency. The steady-state responses of a system are particularly amplified at these small peaks, well-known as superharmonic resonances, occurring when one of the higher generated frequencies matches the resonant frequency, approximately corresponding to $\omega_{1,bi} \approx 2\nu$, $\omega_{1,bi} \approx 3\nu$, ... , see [37].

Since the nonlinear effect is more emphasized in the case of the bimodular beam with T cross-section, this type of cross-section will be used to analyze the influence of different harmonic truncation orders N on determining the frequency-response curve. Figs. 5.11 and 5.12 illustrate the frequency-response functions of the bimodular beam with T cross-section during downward and upward bending, determined for five different harmonic order truncations. These functions are normalized by corresponding static deformation of the bimodular beam at the midspan in the case of downward bending, denoted by $a^{(+)}_{st,bi}$, while the frequency axis is normalized by the circular frequency $\omega_{1,bi}$. The frequency-response curve near the primary resonance is satisfactorily approximated by the single term $N = 1$ for both bending cases. However, in this case, the absence of superharmonic resonances indicates the necessity of including additional harmonics for a more accurate approximation. Remarkably, as more harmonics are included, the accuracy of the current frequency-response curve improves, revealing additional superharmonic peaks. While the truncation order of $N = 3$ effectively approximates the primary resonance, additional harmonics are required to better approximate the superharmonic resonance peak at $\nu/\omega_{1,bi} \approx 1/3$.

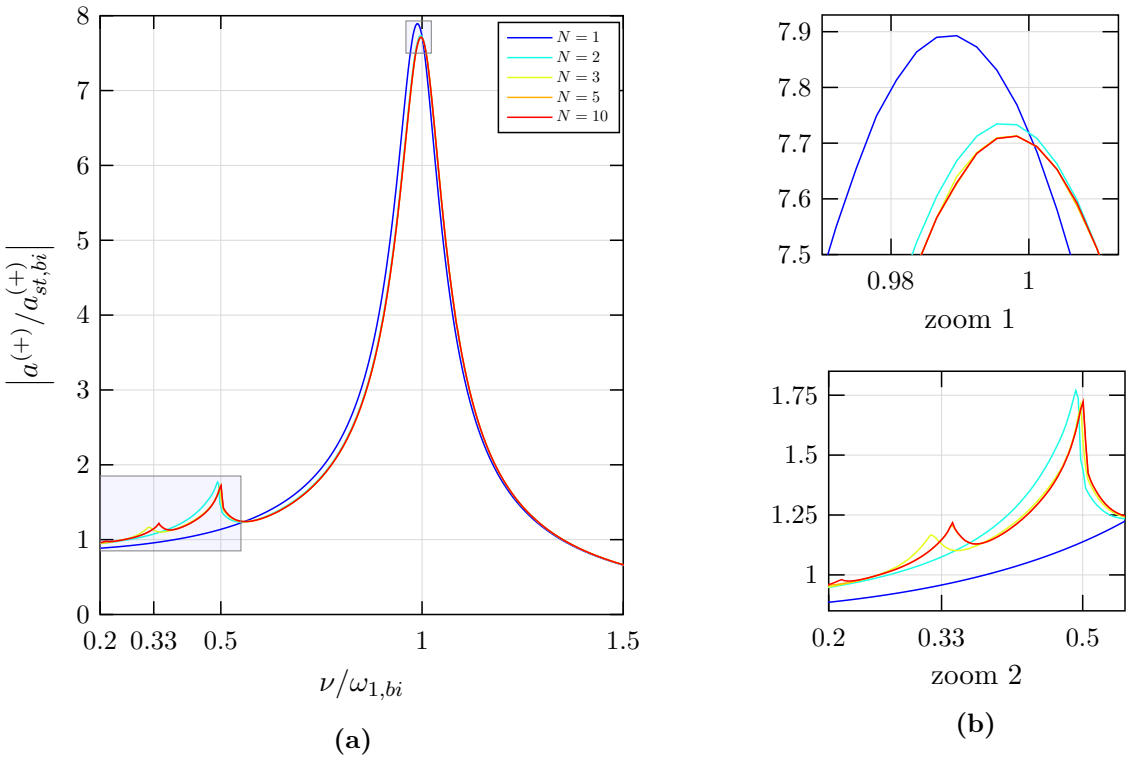

Fig. 5.11: (a) Frequency-response curve, $w(x,t) \geq 0$ (b) zoom into peaks

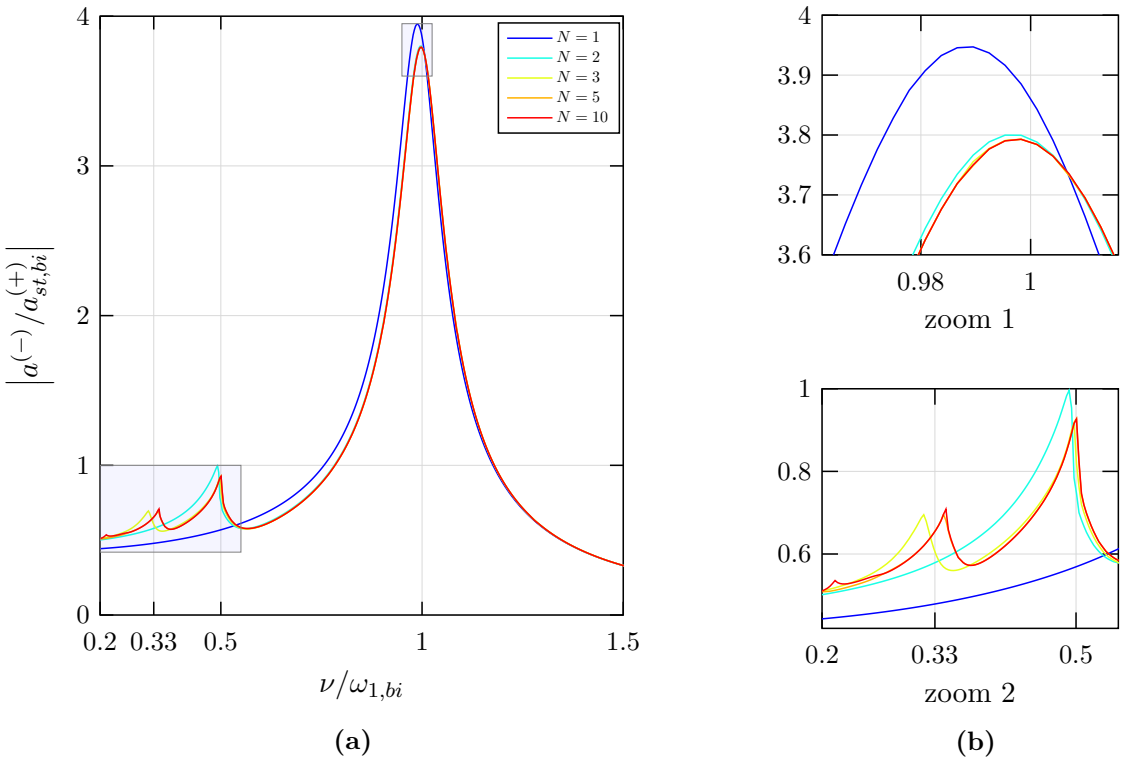

Fig. 5.12: (a) Frequency-response curve, $w(x,t) \leq 0$ (b) zoom into peaks

As shown in Fig. 5.10, the analysis includes a harmonic order truncation of $N = 10$ to illustrate higher harmonics' disparities and convergence rates. In contrast to this figure, which presents the resulting frequency-response curve from different numbers of higher harmonics, Fig. 5.13 provides a separate representation of the amplitude-frequency curve for each of the first ten harmonics, denoted by $|a_j|$, where j ranges from 1 to 10. Here, $|a_1^{(+)}|$ and $|a_1^{(-)}|$ denote the amplitudes of the fundamental harmonic during downward and upward bending, respectively. The higher harmonics, denoted by subscripts from 2 to 10, are additionally shown in two zoomed figures to offer a more detailed insight into their frequency ratio variation, as depicted in Figs. 5.13a and 5.13b. Light blue areas indicate these zoomed regions.

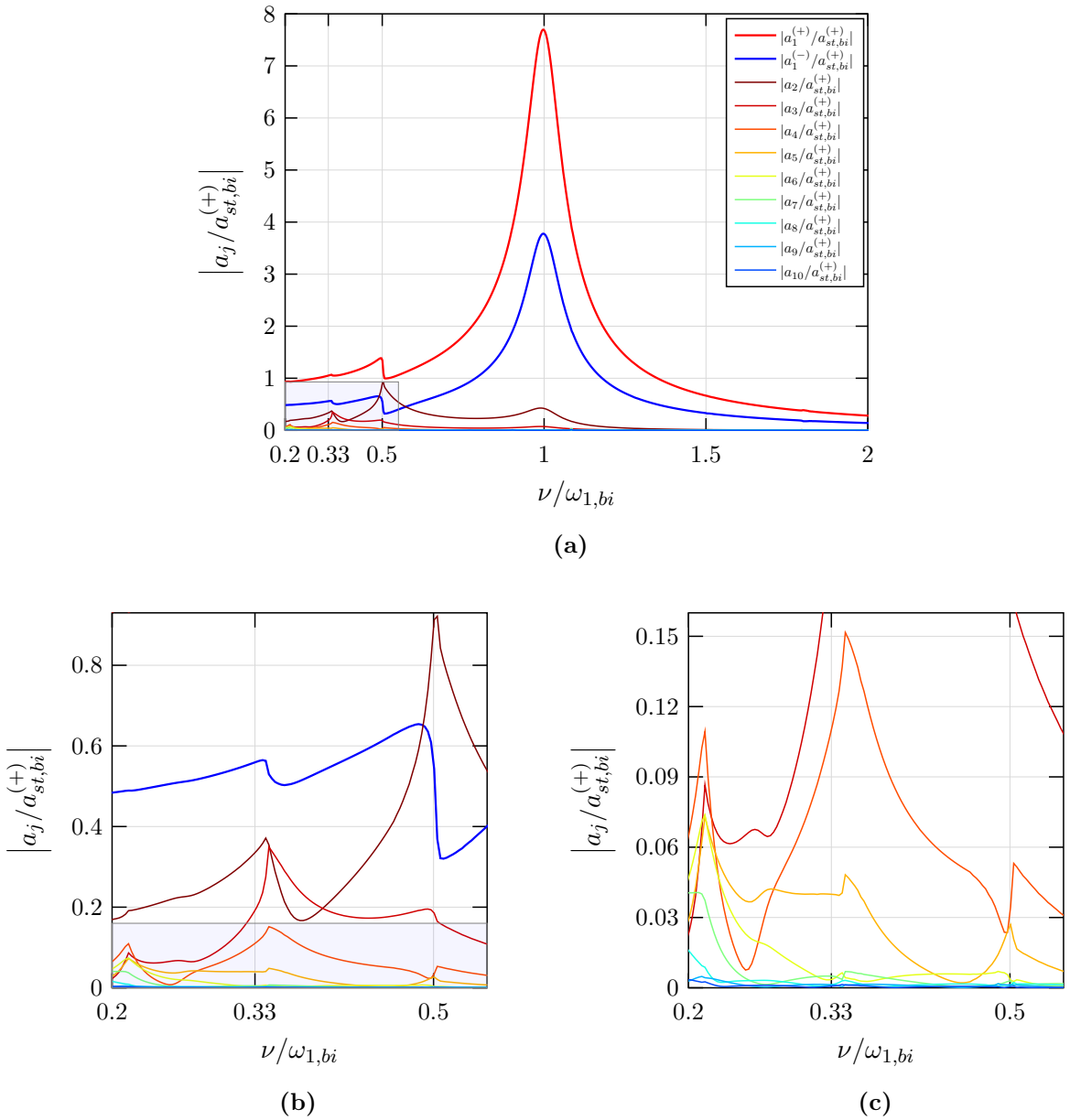

Fig. 5.13: Bimodular beam with T cross-section (a) frequency-response curves at midspan
(b) zoom into superharmonics $0 \leq |a_j/a_{st,bi}^{(+)}| \leq 0.93$
(c) zoom into superharmonics $0 \leq |a_j/a_{st,bi}^{(+)}| \leq 0.16$

As illustrated in the previous figures, each frequency curve is amplified at its own resonance location but undergoes additional amplification at the precise locations of other harmonic resonances. The following analysis will exclusively focus on bimodular beams to show their varying behaviors, particularly influenced by cross-sectional geometry. For this reason, the frequency-response curves of the bimodular beams are additionally represented in Fig. 5.14, where the bimodular beam with a rectangular cross-section is selected as a reference, showing linear behavior. This implies that the frequency-response curves are normalized based on the amplitude of static deflection of the bimodular beam with a rectangular cross-section at the midspan, denoted by a^r_{st}. Furthermore, the frequency axis is also normalized relative to the natural circular frequency of the bimodular beam with the rectangular cross-section, represented by ω^r_1.

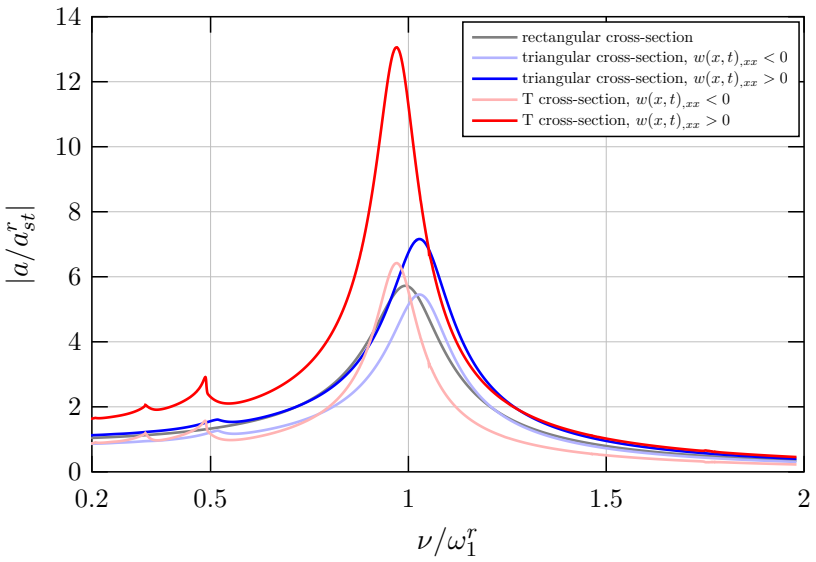

Fig. 5.14: Frequency-response curves at midspan of bimodular beams, normalized by ω^r_1 and a^r_{st}

Knowing the amplitudes, which correspond to the Fourier coefficients, it is possible to determine the response in the time domain for a selected circular frequency ratio using the Fourier series approximation defined in Eq. (4.33). The frequency ratio $\nu/\omega_{1,uni}$ is initially set to 0.54. However, when expressed in the new normalized ratio, it becomes $\nu/\omega^r_1 = 0.34$. The time-domain dynamic responses of bimodular beams under harmonic excitation with a circular frequency ν, analyzed using the harmonic balance method, are graphically illustrated in Fig. 5.15. In order to validate the results, the responses of bimodular beams with three different cross-sections obtained using the Newmark method are also included in Fig. 5.15. It is evident that all responses obtained by the harmonic balance method, regardless of the harmonic truncation order N, do not initially match those obtained using the Newmark method. The reason for this discrepancy is that the harmonic balance method analyzes only steady-state responses resulting from periodic excitation. This indicates that differences observed initially result from transient responses, which are effectively handled by the Newmark method. As the transient vibration diminishes exponentially over time until it becomes negligible, the solution obtained with the harmonic balance method will converge to the one obtained by the Newmark method. When considering the beam with rectangular cross-section, the responses coincide still by a single term $N = 1$, as represented in Fig. 5.15a. This can be explained by the absence of additional internal forces, which results in

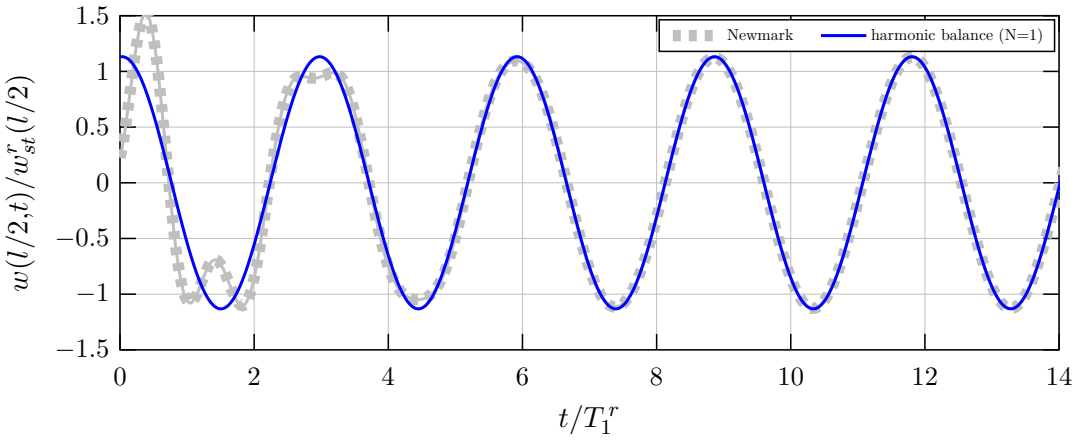

(a)

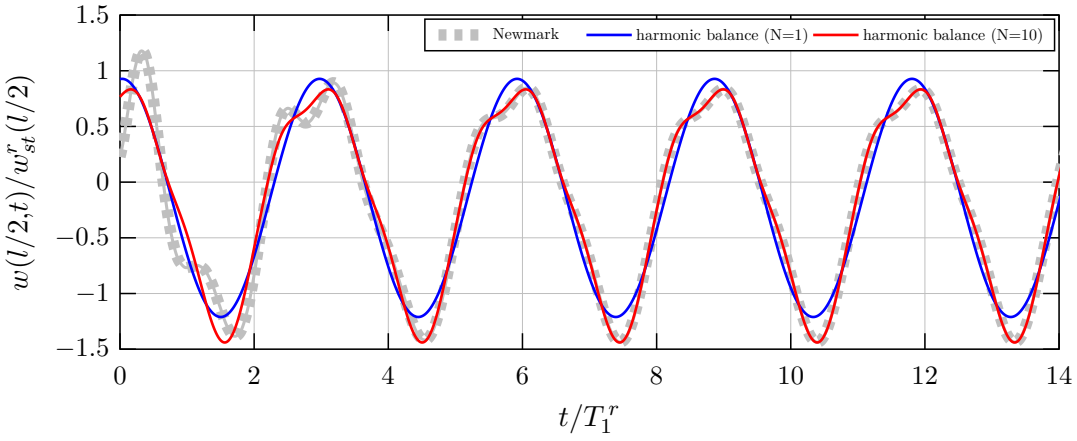

(b)

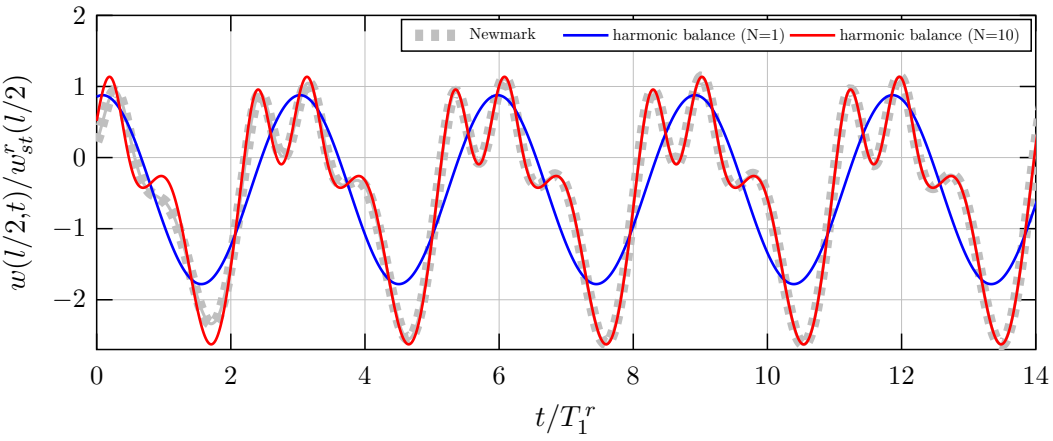

(c)

Fig. 5.15: Comparison of dynamic responses of bimodular beam determined by Newmark and harmonic balance method (a) rectangular cross-section (b) triangular cross-section (c) T cross-section

the linear behavior of the system. In other words, the steady-state response is characterized by a single fundamental frequency at which the system vibrates without higher harmonics. However, this behavior is not observed in beams with the triangular and T cross-sections due to additional internal non-symmetric forces. Consequently, the initial approximation with $N = 1$ does not provide sufficient accuracy, especially for beams with T cross-sections, necessitating the inclusion of higher harmonics for a better approximation. The influence of the harmonic truncation order has been already illustrated in the frequency domain in Fig. 5.12, and thus, it will not be separately provided here for the time domain. In general, a satisfactory approximation can often be achieved with a low truncation order due to the efficiency of the Fourier series in representing periodic functions. Based on the frequency ratio and the information provided in Fig. 5.12, it becomes evident that for a sufficiently accurate solution, at least four harmonics are required when the frequency ratio is approximately equal to 1/3, specifically in the case of the T cross-section. Figure 5.15 graphically illustrates the approximated solutions considering ten terms represented by the red curves. As evident, they perfectly coincide with the solutions obtained using the Newmark method, thereby verifying the validity and efficiency of this approach in analyzing the nonlinear vibration of bimodular beams.

Fig. 5.16 shows the corresponding phase plane of steady-state response obtained by the harmonic balance method.

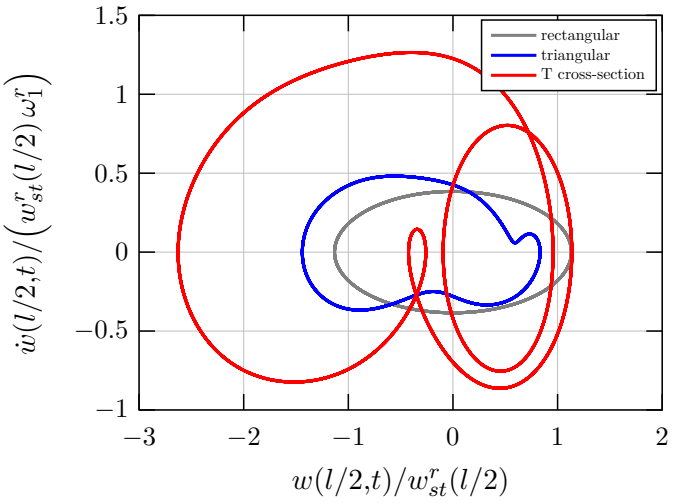

Fig. 5.16: Phase plane of harmonic vibration, $\nu/\omega^r_1 = 0.34$

The responses of bimodular beams to harmonic excitation, where the excitation circular frequency is equal to the circular frequency $\omega^r_{1,bi}$ of the bimodular beam with the rectangular cross-section (as provided in Table 5.4), are depicted in Fig. 5.17a. It is apparent that all beams exhibit resonant responses, although with varying amplitudes. Similarly, the bimodular beams are individually subjected to two other circular frequencies, namely $\omega^t_{1,bi}$ and $\omega^T_{1,bi}$, where the superscripts t and T denote the triangular and T cross-sections, respectively. As previously mentioned, these circular frequencies are listed in Table 5.4. The obtained resonant responses are also depicted in Fig. 5.17. Each dynamic response is visually represented in the phase plane in Fig. 5.18. However, it should be noted that the responses in the phase plane represent only the steady-state solutions.

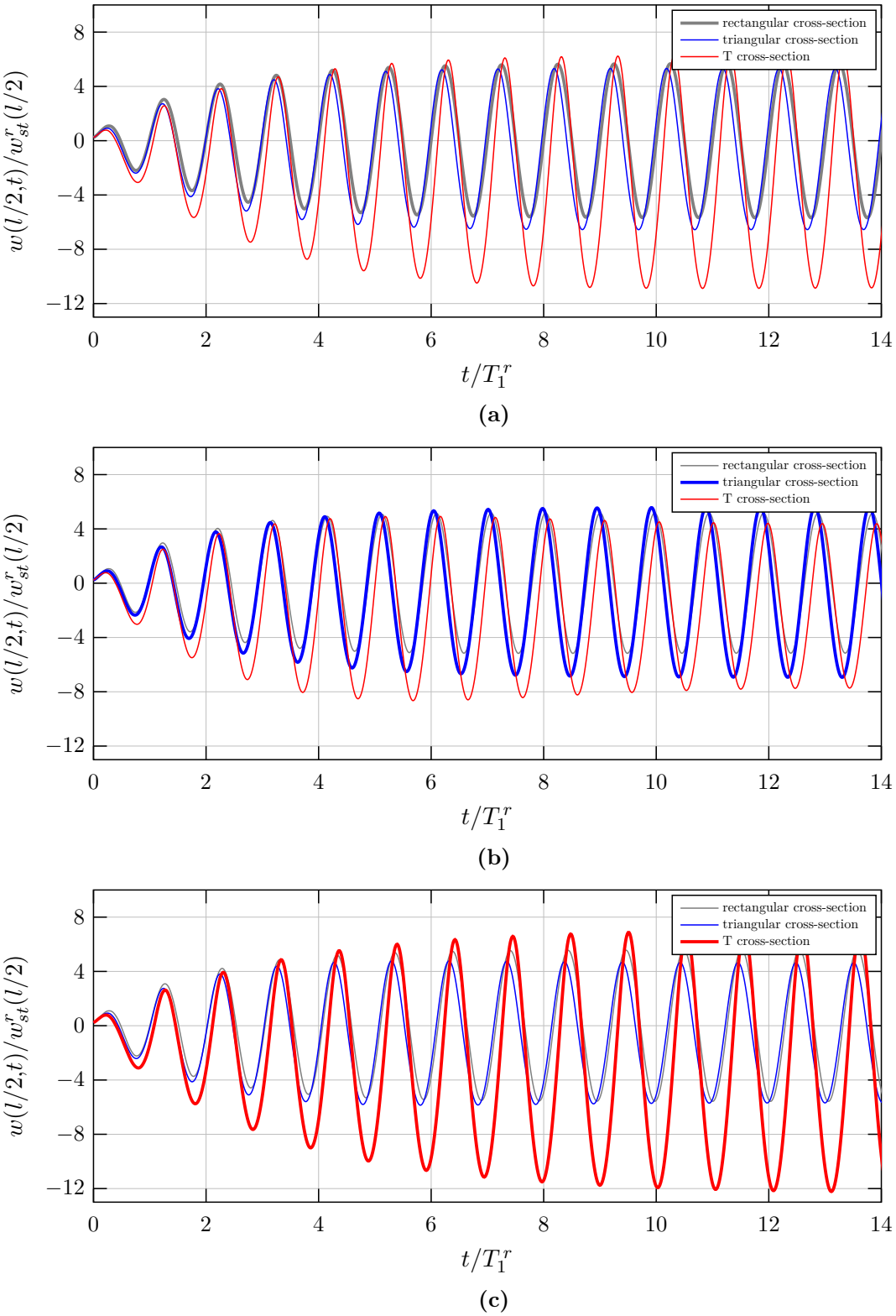

Fig. 5.17: Response to harmonic excitation for three values of the exciting frequency (a) $\nu = \omega^r_{1,bi}$ (b) $\nu = \omega^t_{1,bi}$ (c) $\nu = \omega^T_{1,bi}$

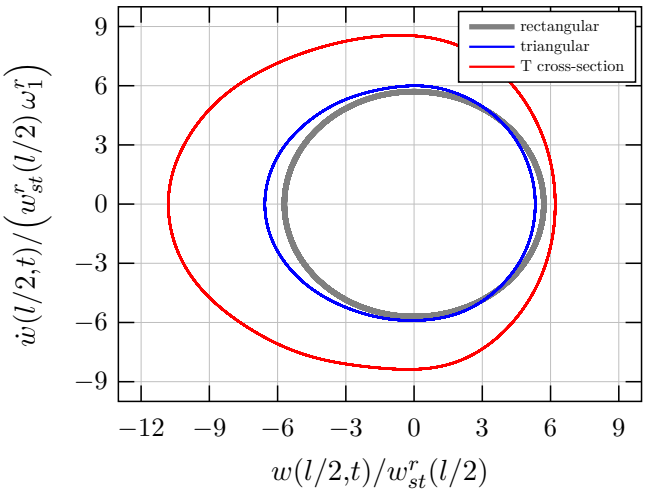

(a)

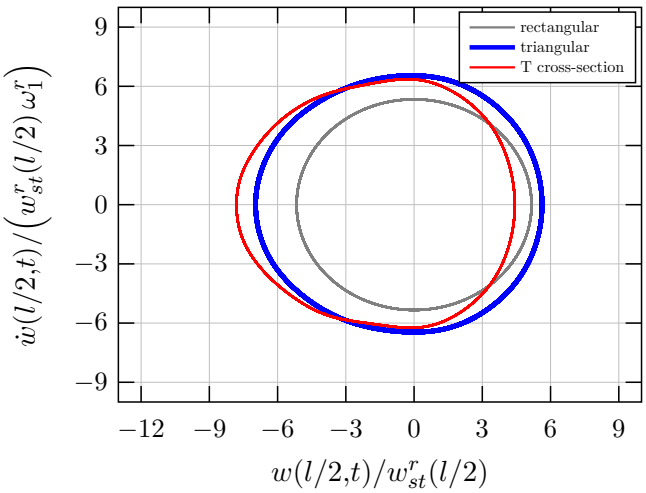

(b)

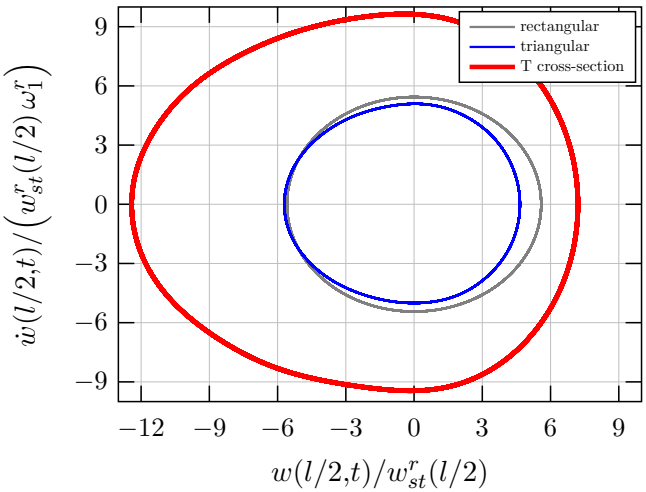

(c)

Fig. 5.18: Phase plane of harmonic vibration when (a) $\nu = \omega^r_{1,bi}$ (b) $\nu = \omega^t_{1,bi}$ (c) $\nu = \omega^T_{1,bi}$

The influence of different values of the modular ratios δ on the response of the bimodular beam with T cross-section for two bending states is graphically illustrated in Figs. 5.19 and 5.20. It is evident that increasing the modular ratio leads to a decrease in amplitude and a shift of the response peak towards higher frequencies. However, in this case, the nonlinear phenomena are much more significant due to additional internal forces caused by stiffness differences between two bending configurations.

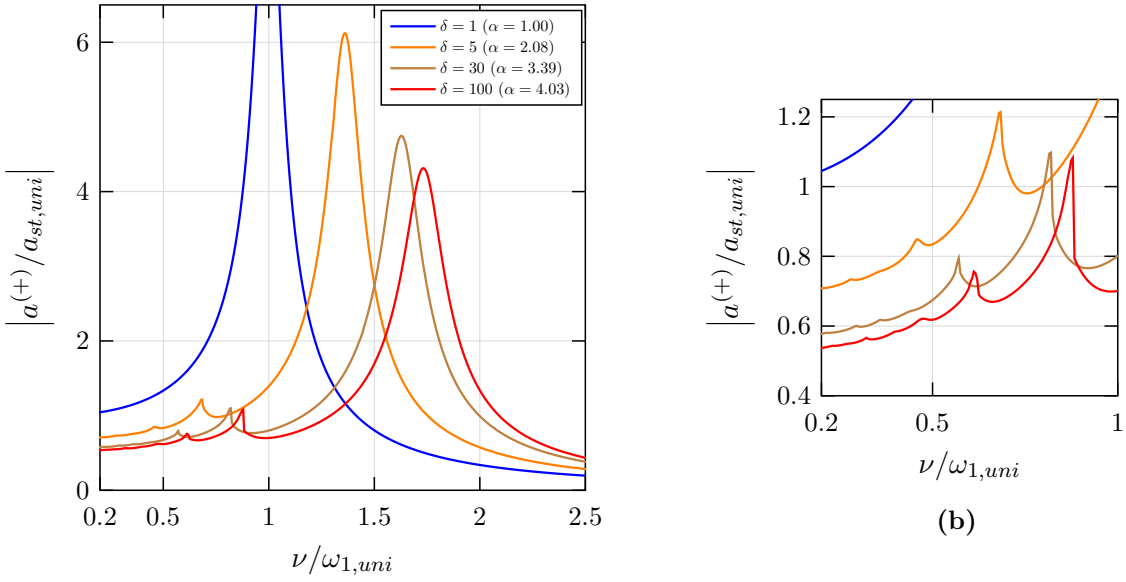

Fig. 5.19: (a) Frequency-response curve, $w(x,t) \geq 0$ (b) zoom into superharmonic peaks

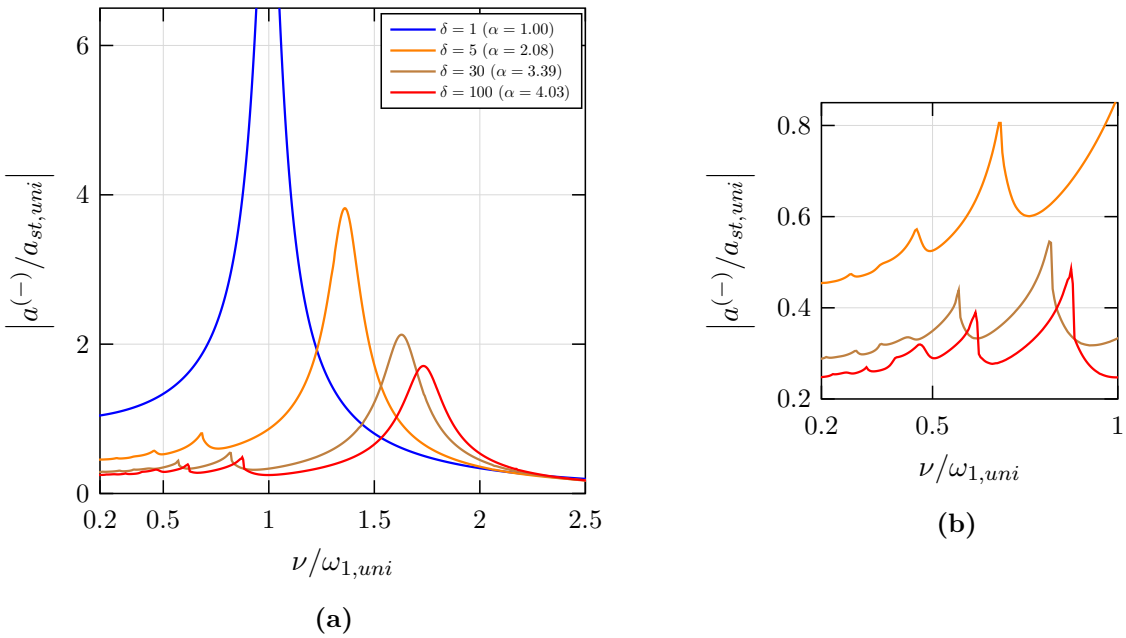

Fig. 5.20: (a) Frequency-response curve, $w(x,t) \leq 0$ (b) zoom into superharmonic peaks

Chapter 6

Conclusion

This thesis investigates the dynamic analysis of the structures characterized by varying behavior of elastic resisting forces during vibration. The study examined the systems with a single degree of freedom and systems with distributed mass and elasticity. When considering a bilinear spring-mass system with a single degree of freedom, it is not possible to find an analytical solution through a single equation that covers the entire motion domain. However, the dynamic responses of these systems can be determined piecewise. Similar to the piecewise linear analytical solution for free vibration of the bilinear elastic oscillator, an exact solution for harmonic excitation is presented. This solution can also be separately formulated for each considered displacement segment, ensuring continuity of displacement and velocity at transition times derived from the specified linear steady-state conditions. Although linear solutions exist within each positive or negative displacement domain, the resulting vibration exhibits nonlinear effects due to discontinuous elastic resisting force. The piecewise solutions are derived meaningfully and are well-suited for computational implementation.

Considering structures with distributed mass and load-dependent elastic properties, it is clear that they cannot be easily categorized as those with, for example, effective isotropic parameters. Consequently, bimodular composites can be effectively modeled as two-layer laminates. However, their neutral axis position depends on the curvature sign, namely the bending state, leading to discontinuous behavior during vibration. Therefore, it becomes essential to utilize an independent reference axis when formulating equations of motion for flexural oscillations. The position of the neutral axis within each bending configuration depends not only on the elastic material properties but also on the cross-sectional shape. According to this study, structures featuring symmetric cross-sections relative to the η-bending axis, such as rectangular cross-sections, demonstrate uniform stiffness during both downward and upward bending. Compared to unimodular structures characterized by a single Young's modulus in compression, bimodular composites exhibit a higher effective bending stiffness, increased by an amplification factor. In contrast, analyzing nonsymmetric cross-sections with respect to the η-bending axis, including the triangular, trapezoidal, or T cross-section presented here, indicates differences in effective bending stiffness between two bending states. These differences are particularly emphasized in T cross-sections due to the width discontinuity. A specified effective bending stiffness ratio characterizes the disparities in stiffness.

The dynamic response of a system may differ between linear and nonlinear, depending on the material and cross-section utilized. If an effective bending stiffness difference exists between upward and downward bending, deriving an exact closed-form solution for the entire motion domain expressed by a single equation is not possible, similar to the case with a bilinear elastic oscillator. For this reason, isogeometric analysis is applied to provide a solution approach, not just for linear but specifically for nonlinear vibrational responses of a bimodular beam. Although the strong form of the governing equation requires the fourth spatial derivative of the bending displacement function, the weak form involves the second derivative, allowing for efficient evaluation through this numerical method. Compared to classical beam finite elements

using the well-known cubic Hermite polynomials, isogeometric finite elements require only half the degree of freedom. This characteristic makes the isogeometric approach more advantageous from a numerical point of view, particularly for nonlinear vibration analysis. Furthermore, the isogeometric analysis provides the opportunity to use higher-order basis functions, leading to higher accuracy and faster convergence of natural frequencies.

This study indicates that bimodular beams, characterized by symmetric cross-sections concerning the η-bending axis, such as rectangular cross-sections utilized in this analysis, exhibit a linear dynamic response. More precisely, these systems experience no additional internal forces due to their consistent effective bending stiffness across both bending states. However, analyzing bimodular beams with nonsymmetric cross-sections relative to the η-bending axis, such as triangular, trapezoidal, or T cross-section, indicates nonlinear dynamic responses. This behavior can be explained by additional varying internal forces arising from differences in stiffness, as determined by the effective bending stiffness ratio. The isogeometric model provides approximate solutions for a wide range of cross-sections, showing nonlinear effects in dynamic responses, as evidenced by the triangular and T cross-sections studied in this context.

Within numerical investigations, the analysis focuses on the influence of cross-sections on dynamic response. For this purpose, three cross-sections, namely, rectangular, triangular, and T cross-sections, are analyzed, each with equal cross-sectional areas and approximately equal moments of inertia about the η-bending axis. Since the considered cross-sections have equal cross-sectional areas, the beams also possess the same mass per unit length. Although unimodular beams demonstrate coinciding dynamic responses due to equal mass per unit length and approximately equal bending stiffness, significant differences arise in the dynamic responses of bimodular beams despite using the same modular ratio. The reason behind this phenomenon is the influence of a cross-section on determining the position of the neutral axis and, consequently, on effective bending stiffnesses. The resulting variations in bending stiffness between two bending states lead to additional internal asymmetric forces, resulting in nonlinear vibrations. This effect is particularly evident in the case of a bimodular beam with a T cross-section.

When a bimodular beam is subjected to periodic excitation, the harmonic balance method can be efficiently applied for frequency-response analysis. This method involves approximating the solution with a truncated Fourier series in the time domain, which can subsequently be transformed into the frequency domain. Using this method, one can derive frequency-response functions that may vary between linear and nonlinear responses, depending on the material characteristics and shape of a cross-section. Bimodular beams with nonsymmetric cross-sections exhibit vibrations not only with the excitation frequency but also with higher frequencies, resulting in particularly emphasized small peaks in the frequency-response curve, known as superharmonic resonances. These resonances can be effectively treated by including a sufficient number of harmonics.

Based on the presented results of the numerical analysis, the significant conclusion is that symmetric cross-sections with respect to the η-bending axis behave much more favorably compared to nonsymmetric cross-sections when bimodular beams oscillate freely due to initial conditions or are subjected to a periodic excitation. However, when subjected to a short pulse, the response of bimodular beams with nonsymmetric cross-sections depends on the direction of an applied load in the forced vibration phase due to differing stiffness properties during upward and downward bending motion. In contrast, the behavior of bimodular beams with symmetric cross-sections remains unaffected by load direction. Increasing the modular ratio reduces the vibration amplitude but simultaneously increases the nonlinear effect when using nonsymmetrical cross-sections.

Future studies may analyze additional linear and nonlinear bimodular structures across the time and frequency domains, including straight and particulary curved beams, plates, and shells.

Bibliography

[1] C. Bert. "Models for Fibrous Composites With Different Properties in Tension and Compression". In: *Journal of Engineering Materials and Technology* 99 (1977), pp. 344–349. URL: https://doi.org/10.1115/1.3443550.

[2] C. Bert and F. Gordaninejad. *Analyses of beams constructed of nonlinear materials having different behavior in tension and compression*. Tech. rep. School of Aerospace, Mechanical and Nuclear Engineering, The University of Oklahoma, Norman Oklahoma 73019, 1982.

[3] C. Bert, J. Reddy, W. Chao, and V. S. Reddy. "Vibration of thick rectangular plates of bimodulus composite material". In: *Journal of Applied Mechanics* (1981). DOI: https://doi.org/10.1115/1.3157625.

[4] C. Bert and A. Tran. *Static and Dynamic Analyses of Thick Beams of Bimodular Materials*. Tech. rep. School of Aerospace, Mechanical and Nuclear Engineering, The University of Oklahoma, Norman Oklahoma 73019, 1981.

[5] C. Bert and A. Tran. "Transient response of a thick beam of bimodular material". In: *Earthquake Engineering & Structural Dynamics* 10 (1982), pp. 551–560.

[6] C. W. Bert and M. Kumar. "Vibration of cylindrical shells of bimodulus composite materials". In: *Journal of Sound and Vibration* 81 (1982), pp. 107–121. DOI: https://doi.org/10.1016/0022-460X(82)90180-8.

[7] C. W. Bert and C. J. Rebello. "Bending of laminated thick beams of bimodular material". In: *Engineering Structures* 5 (1983), pp. 227–231. DOI: https://doi.org/10.1016/0141-0296(83)90020-2.

[8] C. Bert and F. Gordaninejad. "Transverse shear effects in bimodular composite laminates". In: *Journal of composite materials* 17 (1983), pp. 282–298.

[9] C. Bert, J. Reddy, V. Reddy, and W. Chao. "Bending of thick rectangular plates laminated of bimodulus composite materials". In: *AIAA Journal* 19 (1981), pp. 1342–1349.

[10] C. Bucher. *Mechanik für Ingenieurinnen und Ingenieure: Einführung in die Technische Mechanik*. 2019. ISBN: 9781686710391.

[11] S. Chen, Y. Cheung, and H. Xing. "Nonlinear vibration of plane structures by finite element and incremental harmonic balance method". In: *Nonlinear Dynamics* 26 (2001), pp. 87–104. DOI: https://doi.org/10.1023/A:1012982009727.

[12] Y. Cheung, S. Chen, and S. Lau. "Application of the incremental harmonic balance method to cubic non-linearity systems". In: *Journal of Sound and Vibration* 140 (1990), pp. 273–286. DOI: https://doi.org/10.1016/0022-460X(90)90528-8.

[13] K. Cho, A. Striz, and C. Bert. "Bending analysis of thick bimodular laminates by higher-order individual-layer theory". In: *Composite structures* 15 (1990), pp. 1–24.

[14] A. K. Chopra. *Dynamics of Structures: Theory and Applications to Earthquake Engineering*. Fourth Edition. Pearson, 2012. ISBN: 978-0-13-285803-8.

[15] R. W. Clough and P. Joseph. *Dynamics of Structures*. Third Edition. Computers & Structures, Inc., 1995.

[16] J. A. Cottrell, T. J. Hughes, and Y. Bazilevs. *Isogeometric analysis: toward integration of CAD and FEA*. John Wiley & Sons, 2009.

[17] J. A. Cottrell, A. Reali, Y. Bazilevs, and T. J. Hughes. "Isogeometric analysis of structural vibrations". In: *Computer Methods in Applied Mechanics and Engineering* 195 (2006), pp. 5257–5296. DOI: https://doi.org/10.1016/j.cma.2005.09.027.

[18] J. Cottrell, T. Hughes, and A. Reali. "Studies of refinement and continuity in isogeometric structural analysis". In: *Computer Methods in Applied Mechanics and Engineering* 196 (2007), pp. 4160–4183. DOI: https://doi.org/10.1016/j.cma.2007.04.007.

[19] J.-L. Doong and C.-P. Fung. "Vibration and buckling of bimodulus laminated plates according to a higher-order plate theory". In: *Journal of Sound and Vibration* 125 (1988), pp. 325–339. DOI: https://doi.org/10.1016/0022-460X(88)90287-8.

[20] J.-L. Doong and L.-W. Chen. "Vibration of a Bimodulus Thick Plate". In: *Journal of Vibration, Acoustics, Stress, and Reliability in Design* 107 (1985), pp. 92–97. URL: https://doi.org/10.1115/1.3274722.

[21] S. Elgeti. *Study material for the lecture Isogeometric Analysis*. ILSB - Institute of Lightweight Design and Structural Biomechanics, 2023.

[22] A. Ghazavi and F. Gordaninejad. "Nonlinear bending of thick beams laminated from bimodular composite materials". In: *Composites science and technology* 36 (1989), pp. 289–298.

[23] F. Gordaninejad and C. Bert. *Forced Vibration of Timoshenko Beams Made of Multimodular Materials*. Tech. rep. School of Aerospace, Mechanical and Nuclear Engineering, The University of Oklahoma, Norman Oklahoma 73019, 1983.

[24] F. Gordaninejad. "Deflection and vibration in shear-deformable beams and laminated composites made of bimodular and multimodular materials". 1983.

[25] F. Gordaninejad. "Effect of shear deformation on bending of bimodular composite-material plates". In: *Composite Structures* 12 (1989), pp. 161–170. DOI: https://doi.org/10.1016/0263-8223(89)90019-6.

[26] F. Gordaninejad and C. W. Bert. "A new theory for bending of thick sandwich beams". In: *International Journal of Mechanical Sciences* 31 (1989), pp. 925–934. DOI: https://doi.org/10.1016/0020-7403(89)90033-7.

[27] X.-T. He, L. Cao, Y. Guo, J.-Y. Sun, and Z.-L. Zheng. "A perturbation solution of von-Kármán circular plates with different moduli in tension and compression under concentrated force". In: *Mechanics of Advanced Materials and Structures* 23 (2016), pp. 318–327. URL: https://doi.org/10.1080/15376494.2014.981615.

[28] X.-T. He, P. Xu, J.-Y. Sun, and Z.-L. Zheng. "Analytical Solutions for Bending Curved Beams with Different Moduli in Tension and Compression". In: *Mechanics of Advanced Materials and Structures* 22 (2015), pp. 325–337. URL: https://doi.org/10.1080/15376494.2012.736053.

[29] R. Heuer. "Studienblätter zur Vorlesung Baudynamik". Forschungsbereich Baumechanik und Baudynamik der Technischen Universität Wien, 2023.

[30] R. Heuer and G. El Chabaan. "Nonlinear Vibrations of Bimodular Continua by Means of Isogeometric Analysis". In: *Progress in Continuum Mechanics*. Springer, 2023, pp. 191–200. DOI: https://doi.org/10.1007/978-3-031-43736-6_12.

[31] R. Heuer and G. El Chabaan. "On nonlinear vibrations of bimodular beam structures". In: *Dynamics and Control of Advanced Structures and Machines: Contributions from the 4th International Workshop, Linz, Austria*. Springer, 2022, pp. 61–71. DOI: https://doi.org/10.1007/978-3-030-79325-8.

[32] T. J. Hughes, J. A. Cottrell, and Y. Bazilevs. "Isogeometric analysis: CAD, finite elements, NURBS, exact geometry and mesh refinement". In: *Computer Methods in Applied Mechanics and Engineering* 194 (2005), pp. 4135–4195. DOI: https://doi.org/10.1016/j.cma.2004.10.008.

[33] T. Iwase and K.-i. Hirashima. "High-Accuracy Analysis of Beams of Bimodulus Materials". In: *Journal of Engineering Mechanics* 126 (2000), pp. 149–156. DOI: 10.1061/(ASCE)0733-9399(2000)126:2(149).

[34] D. K. Jadan. "Analytical solution of tapered bimodular beams". In: *Anbar J. Eng. Sci* (2012), pp. 79–101.

[35] J. Kiendl, F. Auricchio, T. J. Hughes, and A. Reali. "Single-variable formulations and isogeometric discretizations for shear deformable beams". In: *Computer Methods in Applied Mechanics and Engineering* 284 (2015), pp. 988–1004. DOI: https://doi.org/10.1016/j.cma.2014.11.011.

[36] M. Krack and J. Gross. *Harmonic Balance for Nonlinear Vibration Problems*. Mathematical Engineering. Springer, 2019. ISBN: 978-3-030-14022-9. DOI: https://doi.org/10.1007/978-3-030-14023-6.

[37] A. H. Nayfeh and D. T. Mook. *Nonlinear Oscillations*. Wiley-VCH, 2008.

[38] W. Nowacki. *Baudynamik*. Springer-Verlag, Wien, NewYork, 1974.

[39] B. Patel, S. Gupta, and R. Sarda. "Free flexural vibration behavior of bimodular material angle-ply laminated composite plates". In: *Journal of Sound and Vibration* 286 (2005), pp. 167–186. DOI: https://doi.org/10.1016/j.jsv.2004.10.004.

[40] B. Patel, A. Lele, M. Ganapathi, S. Gupta, and C. Sambandam. "Thermo-flexural analysis of thick laminates of bimodulus composite materials". In: *Composite Structures* 63 (2004), pp. 11–20. DOI: https://doi.org/10.1016/S0263-8223(03)00120-X.

[41] L. Piegl and W. Tiller. *The NURBS book*. Springer, 1996.

[42] G. N. Prasanth and S. Poovalingam. "Analytical Solution to Bi-Linear Spring Mass Systems Free Vibration". In: *Journal of Aerospace Engineering & Technology* 8 (2018), pp. 21–36. DOI: 10.37591/.v9i3.761.

[43] C. Rebello, C. Bert, and F. Gordaninejad. "Vibration of bimodular sandwich beams with thick facings: a new theory and experimental results". In: *Journal of Sound and Vibration* 90 (1983), pp. 381–397.

[44] J. Reddy. "Transient response of laminated, bimodular-material, composite rectangular plates". In: *Journal of Composite Materials* 16.2 (1982), pp. 139–152. DOI: https://doi.org/10.1177/002199838201600205.

[45] J. Reddy and C. Bert. "On the Behavior of Plates Laminated of Bimodulus Composite Materials". In: *ZAMM - Journal of Applied Mathematics and Mechanics / Zeitschrift für Angewandte Mathematik und Mechanik* 62 (1982), pp. 213–219. DOI: https://doi.org/10.1002/zamm.19820620602.

[46] J. Reddy and W. Chao. "A comparison of closed-form and finite-element solutions of thick laminated anisotropic rectangular plates". In: *Nuclear Engineering and Design* 64 (1981), pp. 153–167.

[47] J. Reddy and W. Chao. “Finite-element analysis of laminated bimodulus composite-material plates”. In: *Computers & Structures* 12 (1980), pp. 245–251. DOI: https://doi.org/10.1016/0045-7949(80)90011-5.

[48] J. Reddy and W. Chao. “Nonlinear bending of bimodular-material plates”. In: *International Journal of Solids and Structures* 19 (1983), pp. 229–237.

[49] S. W. Shaw and P. J. Holmes. “A periodically forced piecewise linear oscillator”. In: *Journal of sound and vibration* 90 (1983), pp. 129–155.

[50] S. Timoshenko. “Strength of materials, part II”. In: *Advanced theory and problems* 245 (1941).

[51] A. Tran and C. Bert. “Bending of thick beams of bimodulus materials”. In: *Computers & Structures* 15 (1982), pp. 627–642. DOI: https://doi.org/10.1016/S0045-7949(82)80003-5.

[52] Y.-P. Tseng and C.-T. Lee. “Bending analysis of bimodular laminates using a higher-order finite strip method”. In: *Composite structures* 30 (1995), pp. 341–350.

[53] M. Urabe. “Galerkin’s procedure for nonlinear periodic systems”. In: *Archive for Rational Mechanics and Analysis* 20 (1965), pp. 120–152.

[54] O. Weeger. “Isogeometric Finite Element Analysis of Nonlinear Structural Vibrations”. PhD thesis. 2015.

[55] O. Weeger, U. Wever, and B. Simeon. “Isogeometric Analysis of nonlinear Euler-Bernoulli beam vibrations”. In: *Nonlinear Dynamics* 72 (2013). DOI: https://doi.org/10.1007/s11071-013-0755-5.

[56] L. Woiwode, N. N. Balaji, J. Kappauf, F. Tubita, L. Guillot, C. Vergez, B. Cochelin, A. Grolet, and M. Krack. “Comparison of two algorithms for Harmonic Balance and path continuation”. In: *Mechanical Systems and Signal Processing* 136 (2020), p. 106503. DOI: https://doi.org/10.1016/j.ymssp.2019.106503.

[57] H. Zhang, L. Zhang, and Q. Gao. “An efficient computational method for mechanical analysis of bimodular structures based on parametric variational principle”. In: *Computers & Structures* 89 (2011), pp. 2352–2360. DOI: https://doi.org/10.1016/j.compstruc.2011.07.008.

[58] L. Zhang, Q. Gao, and H. Zhang. “An efficient algorithm for mechanical analysis of bimodular truss and tensegrity structures”. In: *International Journal of Mechanical Sciences* 70 (2013), pp. 57–68. DOI: https://doi.org/10.1016/j.ijmecsci.2013.02.002.

[59] F. Ziegler. *Mechanics of solids and fluids*. Springer-Verlag New York, Inc., 1998.

[60] L. Zuo and A. Curnier. “Non-linear real and complex modes of conewise linear systems”. In: *Journal of Sound and Vibration* 174 (1994), pp. 289–313.

Appendix A

Appendix

A.1 Dynamic analysis of bilinear elastic oscillator

Tab. A.1: Free-vibration response

$\alpha = 1$				$\alpha = 4$			
i	$t_{0,i}/T_D$	a_i/x_0	ε_i [rad]	i	$t_{0,i}/T_{D,bi}$	a_i/x_0	ε_i [rad]
1	0	5.2223	1.3781	1	0.00	2.7420	1.1975
2	0.47	5.2223	1.3781	2	0.29	5.5048	-0.1919
3	0.97	5.2223	1.3781	3	0.96	2.7420	4.3628
4	1.47	5.2223	1.3781	4	1.29	5.5048	-1.7686
5	1.97	5.2223	1.3781	5	1.96	2.7420	7.5282
6	2.47	5.2223	1.3781	6	2.29	5.5048	-3.3453
7	2.97	5.2223	1.3781	7	2.96	2.7420	10.6935

Tab. A.2: Response to harmonic force; $\nu/\omega_{0,bi} = 0.1875$

$\alpha = 1$					
i	$t_{0,i}/T_D$	$A_i/x_{st}^{(-)}$	$B_i/x_{st}^{(-)}$	$C_i/x_{st}^{(-)}$	$D_i/x_{st}^{(-)}$
1	0	-0,8636	0.9040	1.0636	0.0567
2	0.73	-0.4879	-0.6211	0.4879	-0.9468
3	1.20	0.2921	0.5060	-0.2921	-1.0243
4	1.36	0.5285	0.0458	-0.5285	-0.9248
5	3.06	-0.0686	0.1676	0.0686	1.0629
6	4.98	-0.0407	0.0350	0.0407	-1.0644
7	7.00	-0.0100	0.0111	0.0100	1.0651
8	8.99	-0.0032	0.0028	0.0032	-1.0651
9	10.98	-0.0009	0.0008	0.0009	1.0652
10	12.97	-0.0003	0.0002	0.0003	-1.0652
11	14.96	-0.0001	0.0001	0.0001	1.0652
12	16.95	-0.0000	0.0000	0.0000	-1.0652
13	18.94	-0.0000	0.0000	0.0000	1.0652
14	20.93	-0.0000	0.0000	0.0000	-1.0652
15	22.92	-0.0000	0.0000	0.0000	1.0652

Tab. A.3: Response to harmonic force; $\nu/\omega_{0,bi} = 0.1875$

$\alpha = 4$					
i	$t_{0,i}/T_D$	$A_i/x_{st}^{(-)}$	$B_i/x_{st}^{(-)}$	$C_i/x_{st}^{(-)}$	$D_i/x_{st}^{(-)}$
1	0	-0.0539	0.4975	0.2539	0.0032
2	0.40	-0.9699	-0.6860	0.9699	-0.4403
3	0.69	-0.1757	0.3074	0.1757	-0.1833
4	1.11	-0.3315	-0.4014	0.3315	-1.0122
5	4.11	-0.0335	0.1440	0.0335	0.2517
6	6.54	-0.1810	0.1191	0.1810	-1.0497
7	9.36	-0.0144	0.1289	0.0144	0.2535
8	11.84	-0.2056	0.1625	0.2056	-1.0451
9	14.66	-0.0128	0.1353	0.0128	0.2536
10	17.14	-0.2137	0.1611	0.2137	-1.0435
11	19.98	-0.0127	0.1359	0.0127	0.2536
12	22.45	-0.2144	0.1608	0.2144	-1.0433
13	25.29	-0.0127	0.1360	0.0127	0.2536
14	27.77	-0.2145	0.1607	0.2145	-1.0433
15	30.60	-0.0127	0.1360	0.0127	0.2536

Tab. A.4: Response to harmonic force; $\nu = \omega_{0,bi}$

$\alpha = 1$					
i	$t_{0,i}/T_D$	$A_i/x_{st}^{(-)}$	$B_i/x_{st}^{(-)}$	$C_i/x_{st}^{(-)}$	$D_i/x_{st}^{(-)}$
1	0	0.2000	-4.0001	0	5.0000
2	0.48	-0.4666	2.9157	0.4666	-4.9782
3	0.98	0.3043	-2.1280	-0.3043	4.9907
4	1.48	-0.2204	1.5519	0.2204	-4.9951
5	1.98	0.1665	-1.1315	-0.1665	4.9972
6	2.48	-0.1282	0.8248	0.1282	-4.9984
7	2.98	0.0996	-0.6011	-0.0996	4.9990
8	3.48	-0.0777	0.4380	0.0777	-4.9994
9	3.98	0.0607	-0.3191	-0.0607	4.9996
10	4.48	-0.0474	0.2324	0.0474	-4.9998
11	4.97	0.0369	-0.1692	-0.0369	4.9999
12	5.47	-0.0287	0.1232	0.0287	-4.9999
13	5.97	0.0223	-0.0897	-0.0223	5.0000
14	6.47	-0.0172	0.0652	0.0172	-5.0000
15	6.96	0.0133	-0.0474	-0.0133	5.0000

Tab. A.5: Response to harmonic force; $\nu = \omega_{0,bi}$

$\alpha = 4$					
i	$t_{0,i}/T_D$	$A_i/x_{st}^{(-)}$	$B_i/x_{st}^{(-)}$	$C_i/x_{st}^{(-)}$	$D_i/x_{st}^{(-)}$
1	0	-0.2436	0.4529	0.4436	0.0532
2	0.34	-0.9433	-2.4786	0.9433	0.7677
3	1.04	-0.4397	1.2675	0.4397	-0.0792
4	1.38	-1.1324	-3.3892	1.1324	0.4436
5	2.06	-0.4285	1.7774	0.4285	-0.1267
6	2.39	-1.1649	-4.0849	1.1649	0.3496
7	3.06	-0.4223	2.0869	0.4223	-0.1460
8	3.39	-1.1771	-4.5361	1.1771	0.3061
9	4.06	-0.4186	2.2783	0.4186	-0.1562
10	4.39	-1.1831	-4.8207	1.1831	0.2819
11	5.06	-0.4163	2.3971	0.4163	-0.1622
12	5.39	-1.1865	-4.9984	1.1865	0.2672
13	6.06	-0.4149	2.4711	0.4149	-0.1659
14	6.39	-1.1885	-5.1088	1.1885	0.2580
15	7.06	-0.4139	2.5172	0.4139	-0.1682

A.2 Bimodular structure

Figs. A.1 and A.2 present the amplification factors for both bending cases across the modular ratio δ and ratio γ for six different values of β-ratio, ranging from 0 to 1 with a step of 0.2, while the right side illustrates the dependency along β for six distinct values of γ-ratio. The left side of these figures presents the amplification factors for both bending cases across the modular ratio δ and ratio γ for six different values of β-ratio, ranging from 0 to 1 with a step of 0.2, while the right side illustrates the dependency along β for six distinct values of γ-ratio. It becomes apparent that when the T cross-section transforms into a rectangular cross-section with one of the β and γ ratios equal to 0 or 1, the amplification factors change exclusively along the modular ratio axis and are completely identical to the graphical representation of these factors in Subsection 3.5.1 illustrated by Fig. 3.5, showing no difference between the two bending cases. In contrast, T cross-sections manifest such distinctions, particularly evident at lower values of the geometry ratios β and γ, where amplification factors for upward bending exceed those for downward bending.

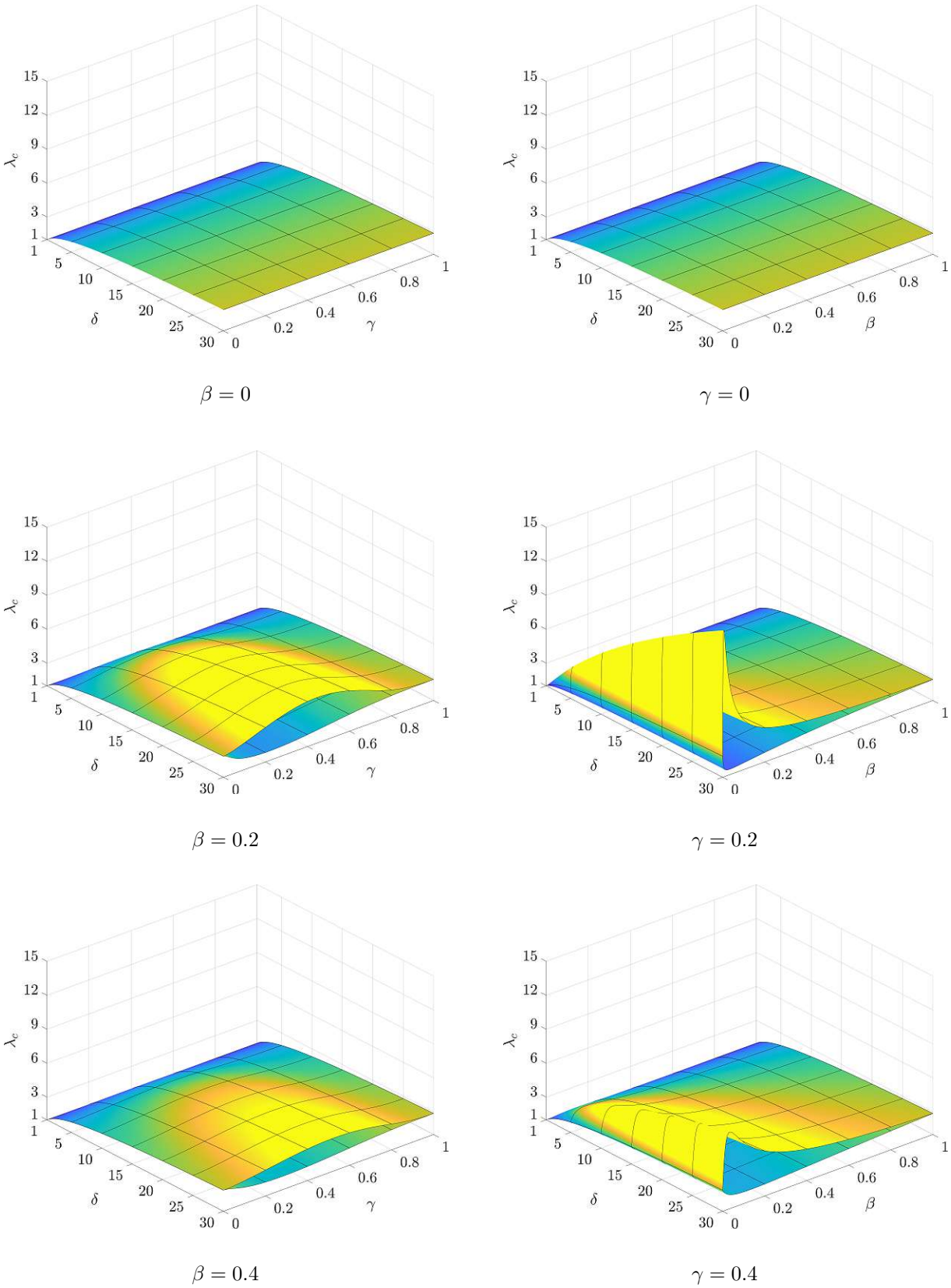

Fig. A.1: Variation of amplification factors with δ, β, and γ

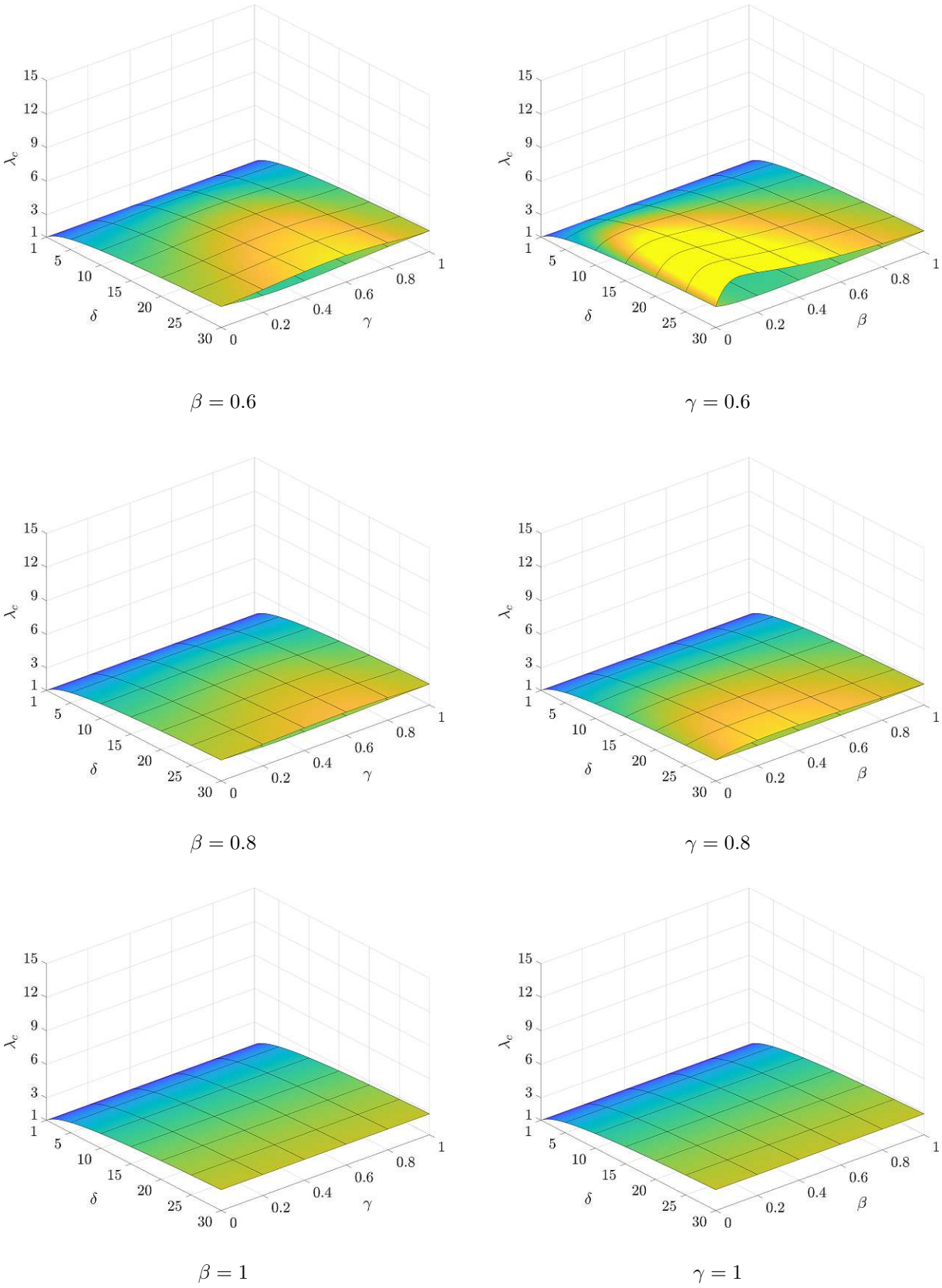

Fig. A.2: Variation of amplification factors with δ, β, and γ